Arnold Schwarzenegger
Governor

NUMERICAL INVESTIGATION OF FAN PERFORMANCE IN A FORCED DRAFT AIR-COOLED STEAM CONDENSER

PIER FINAL PROJECT REPORT

Prepared For:
California Energy Commission
Public Interest Energy Research Program

Prepared By:
J. R. Bredell and D. G. Kröger
University of Stellenbosch

December 2006
CEC-500-2006-113

Prepared By:
J. R. Bredell and D. G. Kröger
Department of Mechanical Engineering
University of Stellenbosch
South Africa
Contract No. 500-02-014
Work Authorization No. 104

Prepared For:
California Energy Commission
Public Interest Energy Research (PIER) Program

Joe O'Hagan,
Contract Manager

Kelly Birkinshaw,
Program Area Manager

Martha Krebs, Ph.D.
Deputy Director
ENERGY RESEARCH AND DEVELOPMENT DIVISION

B. B. Blevins
Executive Director

DISCLAIMER

This report was prepared as the result of work sponsored by the California Energy Commission. It does not necessarily represent the views of the Energy Commission, its employees or the State of California. The Energy Commission, the State of California, its employees, contractors and subcontractors make no warrant, express or implied, and assume no legal liability for the information in this report; nor does any party represent that the uses of this information will not infringe upon privately owned rights. This report has not been approved or disapproved by the California Energy Commission nor has the California Energy Commission passed upon the accuracy or adequacy of the information in this report.

Acknowledgments

Financial support for this project was provided by the Public Interest Energy Research (PIER) Program of the California Energy Commission. The authors would like to thank Joseph O'Hagan of the Energy Commission staff and Kent Zammit and Chuck McGowan of EPRI for their support.

Please cite this report as follows:

Bredell, J. R. and D. G. Kröger. 2006. *Numerical Investigation of Fan Performance in a Forced Draft Air-Cooled Steam Condenser.* California Energy Commission, PIER Energy-Related Environmental Research. CEC-500-2006-113.

Preface

The Public Interest Energy Research (PIER) Program supports public interest energy research and development that will help improve the quality of life in California by bringing environmentally safe, affordable, and reliable energy services and products to the marketplace.

The PIER Program, managed by the California Energy Commission (Energy Commission), conducts public interest research, development, and demonstration (RD&D) projects to benefit California electricity and natural gas ratepayers.

The PIER program strives to conduct the most promising public interest energy research by partnering with RD&D entities, including individuals, businesses, utilities, and public or private research institutions.

PIER funding efforts are focused on the following RD&D program areas:

- Buildings End-Use Energy Efficiency
- Energy-Related Environmental Research
- Energy Systems Integration
- Environmentally Preferred Advanced Generation
- Industrial/Agricultural/Water End-Use Energy Efficiency
- Renewable Energy Technologies
- Transportation

Numerical Investigation of Fan Performance in a Forced Draft Air-Cooled Steam Condenser is the final report for the Alternative Cooling Technologies and Strategies Program project (contract number 500-02-014, work authorization number 104) conducted by the University of Stellenbosch, South Africa. The information from this project contributes to PIER's Energy-Related Environmental Research program.

For more information about the PIER Program, please visit the Energy Commission's website at www.energy.ca.gov/pier/ or contact the Energy Commission at 916-654-5164.

Table of Contents

Preface ii

Abstract viii

Executive Summary 1

1. Introduction 3

1.1. Background and Motivation 3
1.2. Literature Study 7
1.3. Problem Statement 9
1.4. Outline 11

2. System Description 13

2.1. System Components 13
2.1.1. Finned tubes 14
2.1.2. Axial flow fans 15
2.2. Thermal-flow Analysis 18
2.2.1. Energy equation 19
2.2.2. Draft equation 19

3. Numerical Modelling 21

3.1. An Overview of the CFD Code 21
3.1.1. Governing equations 21
3.1.2. Turbulence model 22
3.1.3. Boundary conditions 22
3.1.4. Discritization schemes 23
3.2. Numerical Models 24
3.2.1. Heat exchanger model 25
3.2.2. Numerical fan model 26

4. Evaluation of Numerical Models 32

4.1. Evaluation of the Numerical Fan Model 32
4.1.1. Computational aspects 32
4.1.2. Numerically predicted fan characteristics: A-fan 36
4.1.3. Numerically predicted fan characteristics: B-fan 37
4.2. Evaluation of a Freestanding Fan Unit 38
4.2.1. Computational aspects 39
4.2.2. Numerical results 42
4.3. Discussion of Results 42

5. Fan Performance in a Section of the ACSC 43

5.1. Windless Conditions at Various Platform Heights 43
5.1.1. Computational aspects 44
5.1.2. Effect of platform height 46
5.1.3. Comparison of A-fan and B-fan (Effect of hub-tip ratio) 53
5.1.4. Effect of walkways and windscreens 55
5.2. Crosswind Conditions 59
5.2.1. Computational aspects 59
5.2.2. Discussion 62

6. Conclusions and Recommendations 65

6.1. Importance of this Study 65

6.2. Research Findings 65
6.2.1. Numerical prediction of fan characteristics 65
6.2.2. Effect of platform height on fan performance 65
6.2.3. Comparison of the A-fan and B-fan 66
6.2.4. Effect of a walkway on fan performance 68
6.2.5. Modelling of crosswind using an essentially two-dimensional approach 69
6.3. Future Research 69

7. References 71

8. Nomenclature 76

9. Glossary 78

Appendix A. System Specifications

Appendix B. Fan Installation Specifications

Appendix C. Calculation of Source Terms in the Numerical Heat Exchanger Model

Appendix D. Fan Blade Profile Lift and Drag Characteristics

Appendix E. Numerical Fan Performance Results for a Section of the ACSC under Windless Conditions

List of Figures

Figure 1.1. Forced and induced draft ACHEs 3
Figure 1.2. Air-cooled steam condenser (ACSC) 4
Figure 1.3. Schematic representation of a direct air-cooled power plant 4
Figure 1.4. The Matimba direct air-cooled power plant 5
Figure 1.5. Side elevation of the Matimba power plant 5
Figure 1.6. Side elevation of the El Dorado power plant 6
Figure 1.7. Factors that result in distorted inlet conditions 7
Figure 1.8. Computational grids used by Coetzee and du Toit (2004) in plan view 9
Figure 1.9. A long ACSC bank 10
Figure 1.10. Two rotor-only axial flow fans in plan view 10
Figure 2.1. A fan unit in an ACSC array 13
Figure 2.2. Finned tubes used in industrial air-cooling applications 14
Figure 2.3. Finned tube configuration 15
Figure 2.4. Industrial cooling fans 15
Figure 2.5. BS848 (British Standards Institution 1997) Type A fan test facility 16
Figure 2.6. Blade angle definition 18
Figure 3.1. Simplified numerical model of a ACSC fan unit 24
Figure 3.2. Heat exchanger model 25
Figure 3.3. Vector plot for a three-dimensional rotating mesh fan model 27
Figure 3.4. Fan blade element 28
Figure 3.5. Schematic of the computational grid for actuator disc model 29
Figure 3.6. Velocity diagram of fan blade element 30
Figure 3.7. Computational grid for actuator disc model 31
Figure 4.1. Geometrical layout of fan test model computational grid 32
Figure 4.2. Section view of the computational grid for fan test model 33
Figure 4.3. Isometric view of the computational grid for fan test model 33
Figure 4.4. Detail view of the computational grid at the fan inlet 33
Figure 4.5. Static pressure (Pa) plot for A-fan numerical model (d_F=9.145 m, γ_{pt}=16º) 34
Figure 4.6. Static pressure (Pa) plot for B-fan numerical model (d_F=1.542 m, γ_{cr}=31º) 34
Figure 4.7. Vector plot for A-fan numerical model (d_F=9.145 m, γ_{pt}=16º) 35
Figure 4.8. Vector plot for B-fan numerical model (d_F=1.542 m, γ_{cr}=31º) 35
Figure 4.9. Fan static pressure for A-fan (d_F=9.145 m, γ_{pt}=16º) 36
Figure 4.10. Fan shaft power for A-fan (d_F=9.145 m, γ_{pt}=16º) 36
Figure 4.11. Fan static efficiency for A-fan (d_F=9.145 m, γ_{pt}=16º) 37
Figure 4.12. Fan static pressure for B-fan (d_F=1.542 m, γ_{cr}=31º) 37

Figure 4.13. Fan shaft power for B-fan (d_F=1.542 m, γ_{cr}=31º) 38
Figure 4.14. Fan static efficiency for B-fan (dF=1.542 m, γ_{cr}=31º) 38
Figure 4.15. Operating point for the numerical ACSC fan unit model 39
Figure 4.16. Geometrical layout of the computational grid used to evaluate the ACSC fan unit model 39
Figure 4.17. Dimensions of numerical the ACSC fan unit model 40
Figure 4.18. Section view of the computational grid for fan unit model 40
Figure 4.19. Isometric view of the computational grid for fan unit model 40
Figure 4.20. Detail view of the computational grid for fan unit model 41
Figure 4.21. Static pressure (Pa) plot in the ACSC fan unit model with A-fan 41
Figure 4.22. Static pressure (Pa) plot in the ACSC fan unit model with B-fan 42
Figure 5.1. A section of a long ACSC bank located near its centre 43
Figure 5.2. Layout of computational grid for modelling a section of the ACSC under windless conditions at various platform heights 44
Figure 5.3. Computational grid for modelling a section of the ACSC under windless conditions 45
Figure 5.4. Enlarged sectional view of the computational grid near the fan units 45
Figure 5.5. Streamline plot for H_i=26 m 47
Figure 5.6. Streamline plot for H_i=14 m 47
Figure 5.7. Static pressure (Pa) plot for H_i=26 m (plane Y-Y) 48
Figure 5.8. Static pressure (Pa) plot for H_i=14 m (plane Y-Y) 48
Figure 5.9. Vector plot for H_i=26 m (plane Y-Y) 49
Figure 5.10. Vector plot for H_i=14 m (plane Y-Y) 49
Figure 5.11. Static pressure (Pa) plot for H_i=26 m (plane Z-Z) 50
Figure 5.12. Static pressure (Pa) plot for H_i=14 m (plane Z-Z) 50
Figure 5.13. Vector plot for Hi=26 m (plane Z-Z) 51
Figure 5.14. Vector plot for H_i=14 m (plane Z-Z) 51
Figure 5.15. Volumetric effectiveness of the fans in a section of an ACSC at various platform heights 52
Figure 5.16. System volumetric effectiveness of an ACSC at various platform heights 53
Figure 5.17. Static pressure (Pa) plot of edge fan employing the B-fan with H_i=14 m 53
Figure 5.18. Vector plot of edge fan employing the B-fan with H_i=14 m 54
Figure 5.19. Volumetric effectiveness of the edge fan (for the A-fan and B-fan) in the section of the ACSC at various platform heights 54
Figure 5.20. System volumetric effectiveness for the A-fan and B-fan 55
Figure 5.21. Four different walkway and windscreen configurations investigated 55
Figure 5.22. Static pressure (Pa) plot for case 1 employing the A-fan with H_i=14 m 56
Figure 5.23. Vector plot for case 1 employing the A-fan with H_i=14 m 56

Figure 5.24. Volumetric effectiveness of the edge fan (A-fan) for cases 0 to 3 57
Figure 5.25. Volumetric effectiveness of the edge fan (B-fan) for cases 0 to 3 57
Figure 5.26. System volumetric effectiveness for cases 0 to 3 employing the A-fan 58
Figure 5.27. System volumetric effectiveness for cases 0 to 3 employing the B-fan 58
Figure 5.28. Layout of computational grid for modelling the section of an ACSC under crosswind conditions (essentially two-dimensional modelling approach) 59
Figure 5.29. Computational grid for modelling the section of an ACSC under crosswind conditions. 61
Figure 5.30. Enlarged section view of computational grid near the fan units..... 61
Figure 5.31. Streamline plot for a crosswind of 3 meters per second (m/s) after 70 iterations 62
Figure 5.32. Temperature (K) plot for a crosswind of 3 m/s after 70 iterations 62
Figure 5.33. Static pressure (Pa) plot for a crosswind of 3 m/s after 70 iterations 63
Figure 5.34. Velocity magnitude (m/s) plot for a crosswind of 3 m/s after 70 iterations 63
Figure 5.35. Temperature (K) plot for a crosswind of 3 m/s after 300 iterations 64
Figure 6.1. Numerically determined performance characteristics for A-fan on B-fan 66
Figure 6.2. Axial velocity profiles in actuator disc model for A-fan and B-fan 67
Figure 6.3. Effect of inlet flow distortion on volume flow rate 68

List of Tables

Table 3.1. Conservation equations 21
Table 3.2. Transport equations for k-ε turbulence model 22
Table 3.3. Constants for k-ε turbulence model 22
Table 3.4. Momentum sink terms for heat exchanger model 25
Table 5.1. Constants in equations 5.3 to 5.6 60

Abstract

Inlet air flow distortions in a large air-cooled steam condenser (ACSC), caused by structures, wind, and other fans may result in a significant reduction in fan performance, or volumetric effectiveness, as well as fan blade vibration. This phenomenon has an adverse effect on the heat rejection capacity of an ACSC due to a decrease in air mass flow rate. In this study, the effect of inlet flow distortions on the flow rate through the fans in an ACSC is numerically investigated by modelling the flow field in a section of such a system using the computational fluid dynamics code, FLUENT. The effect of platform height on the volumetric effectiveness of two different types of axial flow fans is considered. The two fans have the same diameter, number of blades, and rotational speed, but feature different blade designs, and hub-tip-ratios of respectively 0.153 and 0.4. Numerical simulations show all-round superior performance in terms of volume flow rate for the fan with a hub-tip-ratio of 0.4. It is furthermore confirmed that the addition of a walkway can significantly increase the flow rate through the fans located near the edge of the fan platform.

Keywords: air-cooled, steam condenser, axial flow fan, fan performance, inlet flow distortions, Computational Fluid Dynamics (CFD)

Executive Summary

Introduction

Forced draft air-cooled steam condensers (ACSCs) consisting of an array of fan units are used in direct air-cooled power plants to condense steam in a closed steam cycle. Axial flow fans located below an A-frame configuration of finned tube heat exchanger bundles, force a stream of ambient cooling air through the system. In so doing, heat from the condensing steam is rejected to the environment via the finned tubes. Owing to the dynamic interaction between the steam turbines and the ACSC, a change in the heat rejection rate of the ACSC will directly influence the efficiency of the steam turbines.

Purpose

Understanding and predicting the factors or mechanisms that can reduce the heat rejection rate of an ACSC is essential. This study involves the numerical modeling of the flow about and through a section of a long ACSC bank consisting of six fan rows, to determine the effect of inlet flow distortions on fan flow rate.

Project Objectives

The main objectives of the investigation are:

- Investigating the effect of platform height on ACSC performance. Because of the obvious cost implications, platform height is a critical design parameter in large industrial air-cooled systems.
- Comparing different axial flow fan designs operating under off-design conditions. Such off-design conditions may potentially be caused by wind, but could also be inherent in the design of an air-cooled system.
- Investigating and evaluating cost-effective external modifications to an ACSC platform which improve its heat rejection capacity.

Project Outcomes

The most important outcomes of the study are:

- Modern flow simulation software was successfully employed as an engineering tool to predict the performance of an ACSC for different design parameters.
- Due to the proximity of the ground, an unfavorable cross-flow velocity component is induced underneath the fan platform of an ACSC. Depending on the height of the fan platform, the induced cross-draft may result in flow separation and distortion at the fan inlets. The reduction in air flow rate with a decrease in platform height was modeled and results were found to be consistent with previous experimental and numerical results.
- It was shown that fans of different designs, which have the same operating point under design conditions, do not have the same operating point under off-design conditions. The importance of taking the fan design and fan performance characteristic into account when designing an ACSC, is emphasized.

- Furthermore, it was shown that relatively economical modifications to the fan platform can significantly improve the performance of fans which are most affected by flow distortions. This would necessarily increase the heat rejection capacity of an ACSC.

Conclusions

Inlet air flow distortions in a large air-cooled steam condenser (ACSC), caused by structures, wind, and other fans, result in a significant reduction in fan flow rate due to the following factors or mechanisms:

- Increased inlet flow losses (i.e., flow separation at the edge of the fan inlet) resulting in a decrease in flow rate.
- Maldistribution of air into the fan (i.e., non-uniform inlet conditions) resulting in fan blade stall and reduction in aerodynamic efficiency.
- Off-axis inflow conditions, which decreases the static pressure rise generated by the fan.

It was shown that different fans are not equally sensitive to these distortions, and that modifications to the fan platform can reduce the flow rate reducing effect of inflow distortions.

Benefits to California

Growing demand, stringent environmental legislation and restrictions on water resources has resulted in increased use of air-cooled systems in the power generating industry in California. It was shown in this investigation that significant economical and performance benefits can be obtained from the aerodynamic optimization of an ACSC, and industrial air-cooled systems in general.

1. Introduction

1.1. Background and Motivation

Mechanical draft air-cooled heat exchangers (ACHEs) and air-cooled condensers (ACCs) use air as medium to cool and condense process fluids. Based on economical and environmental considerations, these systems are often employed instead of water-cooled systems in the petrochemical, air-conditioning, and power-generating industries. In an ACHE, heat from the circulating process fluid is transferred to the air via finned tubes. For construction and handling purposes, these finned tubes are grouped together in units called *heat exchanger bundles.* As illustrated in Figure 1.1, a fan situated upstream or downstream of the heat exchanger forces air through the system to reject the heat to the environment. If the fan is located upstream of the heat exchanger, the ACHE is a forced draft type, as opposed to an induced draft type ACHE, in which the fan is located downstream of the heat exchanger. Kröger 2004 elaborates on different types and configurations of ACHEs and ACCs, and on the advantages and disadvantages of each.

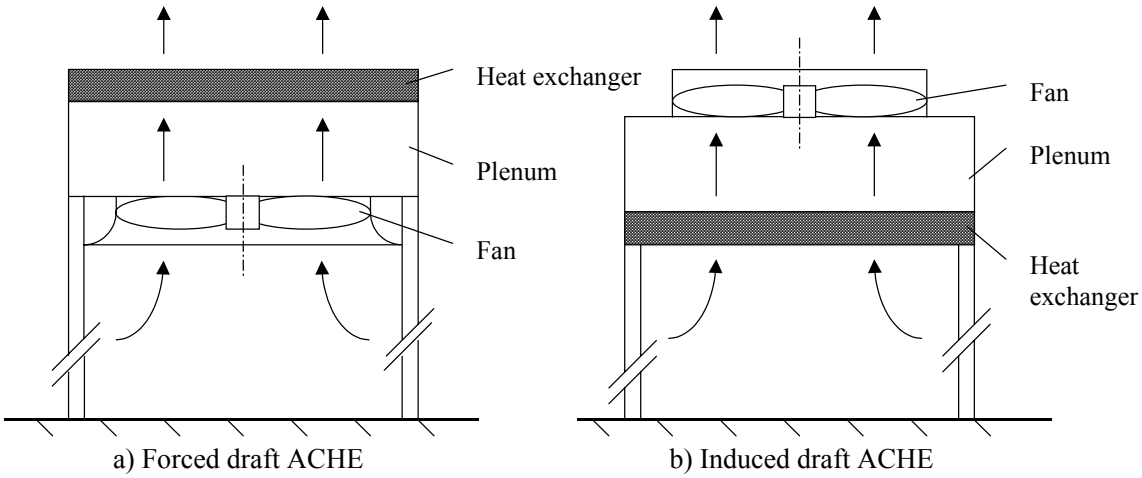

Figure 1.1. Forced and induced draft ACHEs

In an ACC, the process fluid, initially in vapour form, is condensed inside the finned tubes. To remove the condensate effectively, and to reduce the plant footprint, the heat exchanger bundles are installed in a vertical or inclined configuration. Although there are various types of ACC configurations, only the A-frame type, frequently used in direct-cooled power plants, shall be discussed in more detail. An A-frame air-cooled steam condenser (ACSC) unit, shown in Figure 1.2, consists of a series of heat exchanger bundles arranged in an A-frame structure above an axial flow fan. Steam, supplied by a steam header, flows down through the finned tubes. As heat is rejected to the ambient air, the saturated or supersaturated steam condenses and collects in the condensate duct.

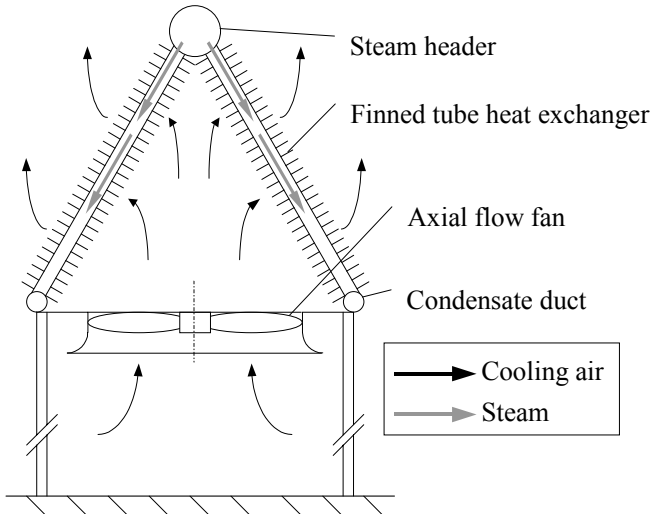

Figure 1.2. Air-cooled steam condenser (ACSC)

In a direct air-cooled power plant, the low-pressure steam from the turbine exhaust enters into the ACSC, as shown in Figure 1.3. The condensate is then pumped back to the boiler via the condensate duct to form a closed steam cycle.

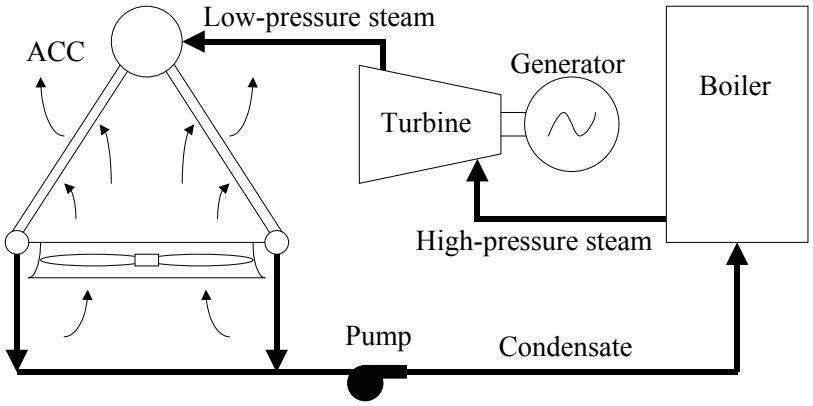

Figure 1.3. Schematic representation of a direct air-cooled power plant

Direct-cooled power plants may differ considerably in layout, construction, and capacity. Two examples of direct-cooled power plants are discussed in more detail.

The world's largest forced draft direct air-cooled power plant, Matimba, shown schematically in Figure 1.4, was commissioned in 1987 and is situated in the Limpopo province of the Republic of South Africa. It has a capacity of 3990 megawatts of electricity, or MW(e), and employs an ACSC consisting of 288 axial flow fans 9.145 meters (m) in diameter, each driven by a 270 kilowatt (kW) electrical motor. The 5760 MW ACSC platform is located 45 m above ground level and covers a plot area of 74.5 m × 510 m. The main dimensions of this plant are shown in Figure 1.5

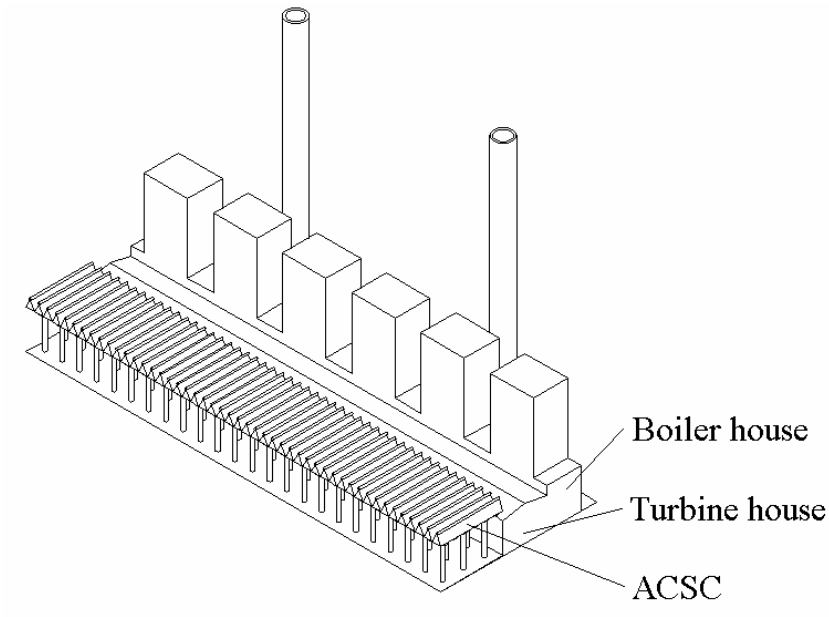

Figure 1.4. The Matimba direct air-cooled power plant

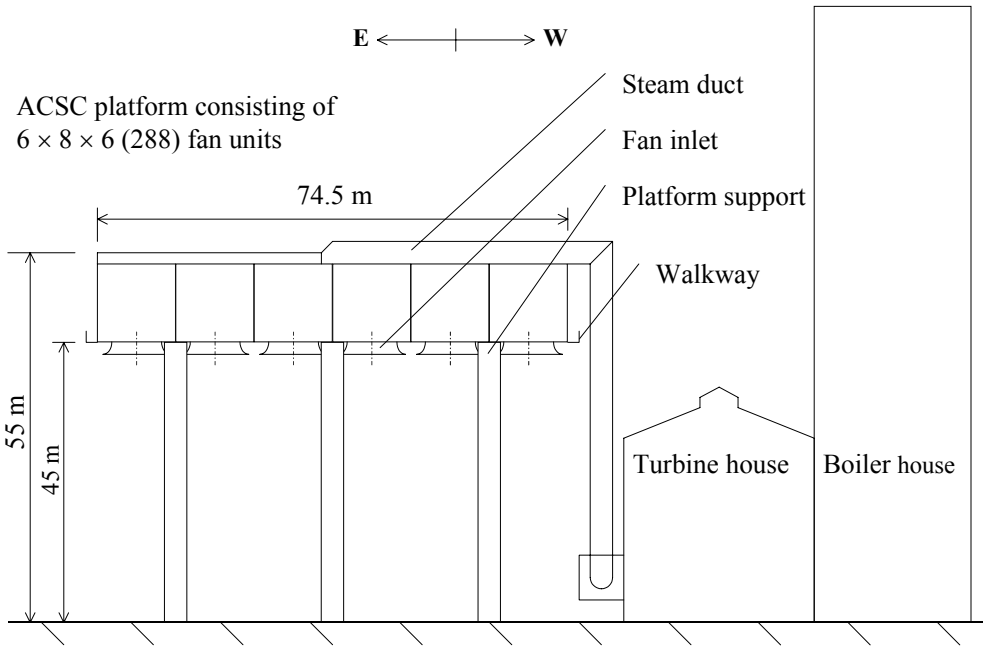

Figure 1.5. Side elevation of the Matimba power plant

Another example of a direct air-cooled power plant is the 480 MW(e) El Dorado plant, southeast of Las Vegas in the Nevada desert, in the United States. This modern, high-efficiency, combined-cycle plant has an ACSC employing 30 axial flow fans with a diameter of 10.363 m. As shown in Figure 1.6, the ACSC platform is located 19.2 m above ground level and covers an area of 83.2 m × 70.5 m.

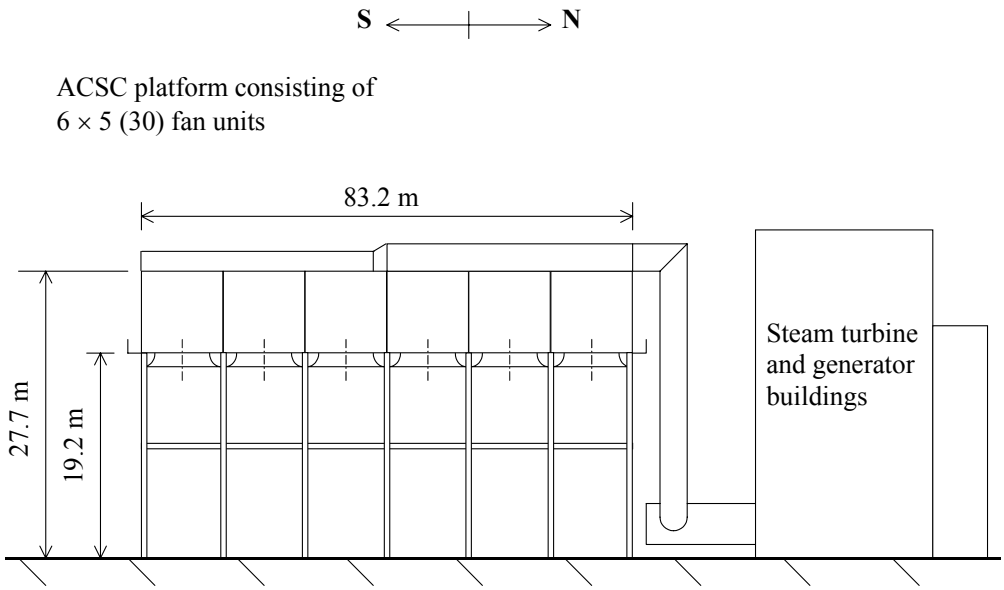

Figure 1.6. Side elevation of the El Dorado power plant

Because air is used as cooling medium, the heat rejection capacity is strongly influenced by ambient conditions such as dry bulb temperature, wind, atmospheric stability, and other meteorological phenomena. It is often found that under off-design conditions (e.g., on hot and windy days) the reduced heat rejection capacity of the ACSC measurably reduces the output of power plants. Goldschagg 1993 reports on the reduction of turbine performance under windy conditions at the Matimba power plant. Due to the strong dynamic interaction between the steam turbine and the ACSC, turbine trips may occur under severe wind conditions.

Consideration of ambient conditions, particularly the prevailing winds, is therefore imperative in the design, location, and orientation of large air-cooled systems. An example of such a case is the Matimba facility (refer to Figure 1.4 and Figure 1.5). The plant is orientated so that the ACSC is upwind of the turbine and boiler buildings under prevailing easterly wind conditions. This limits the distortion of the inlet air flow by the buildings and reduces hot plume recirculation.

An understanding of the global flow field, as well as the detail flow field near the fan inlets, can be applied to optimise the cooling capacity of a forced draft air–cooled system. The objective of this study is to investigate the effect of inlet air flow distortions on the performance of fans in an ACSC by using computational fluid dynamics (CFD) to model the flow field in a section (or sector) of such a system.

1.2. Literature Study

According to Thiart and von Backström 1993, inlet air flow distortions in a forced-draft ACHE (or ACC) can be caused by wind, nearby buildings, and cross-drafts induced by other fans, as shown in Figure 1.7.

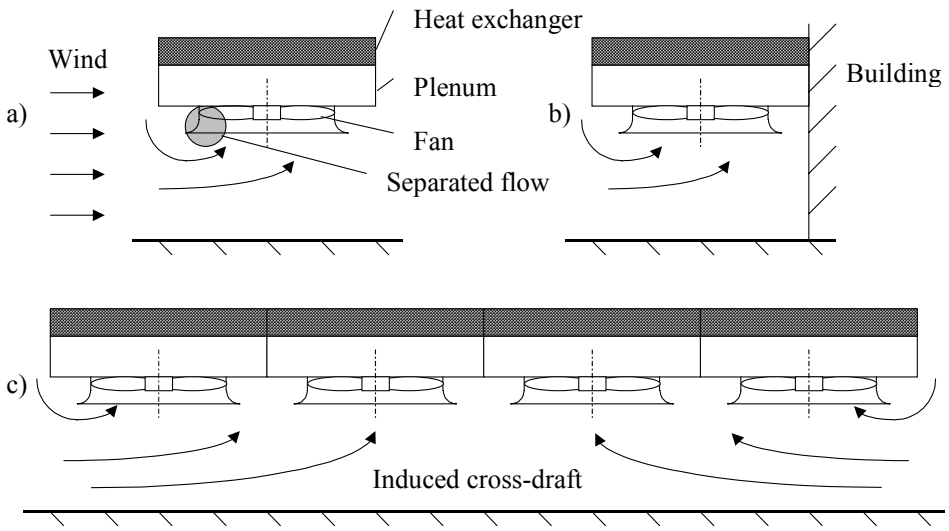

Figure 1.7. Factors that result in distorted inlet conditions

In an experimental study on a scale model of an ACHE, Salta and Kröger 1995 investigated the effect of inlet flow distortions on fan performance. With an experimental set-up similar to Figure 1.7(c), it was found that a reduction in the distance between the fan platform and the ground results in a significant decrease in flow rate, mainly as a result of poor fan performance. They also observed that the fans along the edge or periphery of an ACHE are most affected by flow distortions caused by the induced cross-draft.

Bruneau 1994, who designed an axial flow fan for application in a cooling tower, explains this reduction in fan performance in more detail, and states that, "depending on the severity of the distortions (i.e., non-uniform inlet profiles) the fan blade can stall, accompanied by losses in aerodynamic efficiency and peak pressure rise, as well as blade vibrations."

Duvenhage et al. (1996) numerically and experimentally investigated flow distortions at the inlet of forced-draft ACHEs under induced cross-draft conditions. The platform height, as well as three different inlet shrouds—namely cylindrical, conical and bell-mouth—were considered. Recommendations towards the optimal design of these inlet shrouds were made.

Although the main focus of the study is on flow distortions resulting from induced cross-drafts, a discussion of wind-effects is warranted, seeing that the majority of the relevant literature on numerical modelling of forced draft ACHEs, involves the latter.

According to Duvenhage and Kröger (1996) the negative impact of wind on an ACHE (or ACC) can be divided into two categories. The first category, *recirculation,* results when a fraction of the buoyant plume is drawn back into the ACHE (or ACC) inlet, which increases

the temperature of the cooling medium and decreases the heat rejection rate. The analytical, experimental, and numerical investigation of the reduction in performance of mechanical draft ACHEs due to recirculation are presented in numerous studies (Gunter and Shipes 1971; Kröger 1989; du Toit and Kröger 1993; Duvenhage and Kröger 1995; Rogers et al. 1999).

The second category is the reduction in fan performance due to distorted inlet flow conditions, as shown in Figure 1.7(a). In this case, the reduction in effectiveness of the ACHE is brought about by a decrease in air mass flow rate through the system. Although these two categories of wind-effects are often coupled, usually the one or the other is dominant, depending on the ACHE (or ACC) geometry, wind speed, and direction.

During tests done on a full-scale ACHE under crosswind conditions, Turner (1975) found that flow separation at the fan inlet caused maldistribution of air flow into the fan, which resulted in a reduction in fan performance. Van Aarde (1990) conducted experiments on a full-scale ACSC, and observed similar trends. A significant reduction in fan performance under windy conditions was reported.

The influence of wind speed and direction on a long ACHE bank was numerically investigated by Duvenhage and Kröger (1996). The reduction in fan performance, as well as the plume recirculation, was successfully modelled. They report that crosswinds resulted in a significant reduction in fan performance of the upwind fans, while winds along the longitudinal axis lead to an increase in hot plume recirculation along the sides of the ACHE.

Coetzee (2000) conducted a numerical study on the influence of various atmospheric conditions on different ACHE configurations. He concludes that despite many simplifications and assumptions, CFD models can effectively be used to investigate ACHE operation in different conditions and environments. In a more recent study, Coetzee and du Toit 2004 compared two modelling approaches in order to determine the importance of end-effects in the numerical modelling of ACHEs subjected to wind. In the first approach, the *full three-dimensional* model allows air to pass around the ACHE, thereby including end-effects, as shown in Figure 1.8 a. In the second approach, illustrated in Figure 1.8(b), air is confined to a channel preventing any flow around the ACHE, and therefore excluding end-effects. These researchers point out that this *essentially two-dimensional* modelling approach can be used to represent a heat exchanger bay located near the centre of a large bank of ACHEs.

Van Staden and Pretorius (1996) present an integrated numerical model to predict the global performance of a direct air-cooled power plant. The model employs CFD to simulate the effect of ambient conditions on the ACSC and takes into account the interaction between the steam turbine and ACSC. A case study was performed on the Matimba power plant. More recently this model was validated, to some extent, by comparing steady-state numerical results to measured onsite data. Van Staden (2000) reports a good comparison of temperature profiles, velocity distributions, and air flow paths.

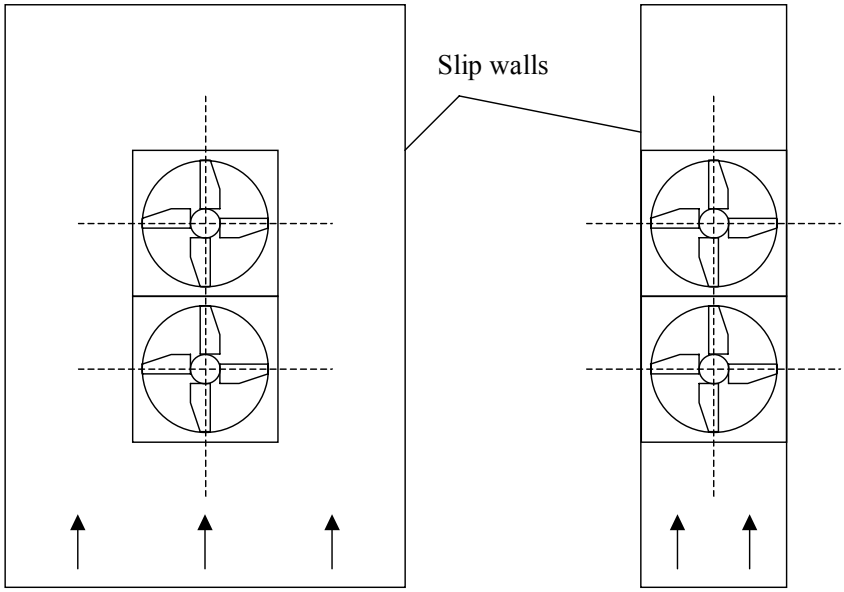

a) Full three-dimensional model b) Essentially two-dimensional model

Figure 1.8. Computational grids used by Coetzee and du Toit (2004) in plan view

From the literature survey it can be concluded that modern numerical modelling techniques can effectively be used to analyse the flow field associated with an ACHE (or ACC) to predict its performance under various operating conditions. Although numerical methods such as CFD may provide valuable insight into such thermal flow problems, the importance of analytical and experimental investigations must not be overlooked.

1.3. Problem Statement

This study involves the numerical modelling of the flow about and through a section (or sector) of an ACSC, as shown in Figure 1.9.

The section located near the centre of a long ACSC bank consists of six fan units, the specifications of which are given in Appendix A. Under windless conditions the realistic assumption can be made that there is no flow across the sectional planes. The focus of this numerical investigation is on the reduction of fan performance due to inlet flow distortion resulting from an induced cross-draft. The degree of distortion is varied by changing the height of the fan platform above the ground.

The numerical investigation of the effect of inlet flow distortions and air maldistribution on the performance of multiple fans require a realistic, computationally inexpensive numerical fan model. Therefore, an important part of this study is the implementation and evaluation of a numerical fan model.

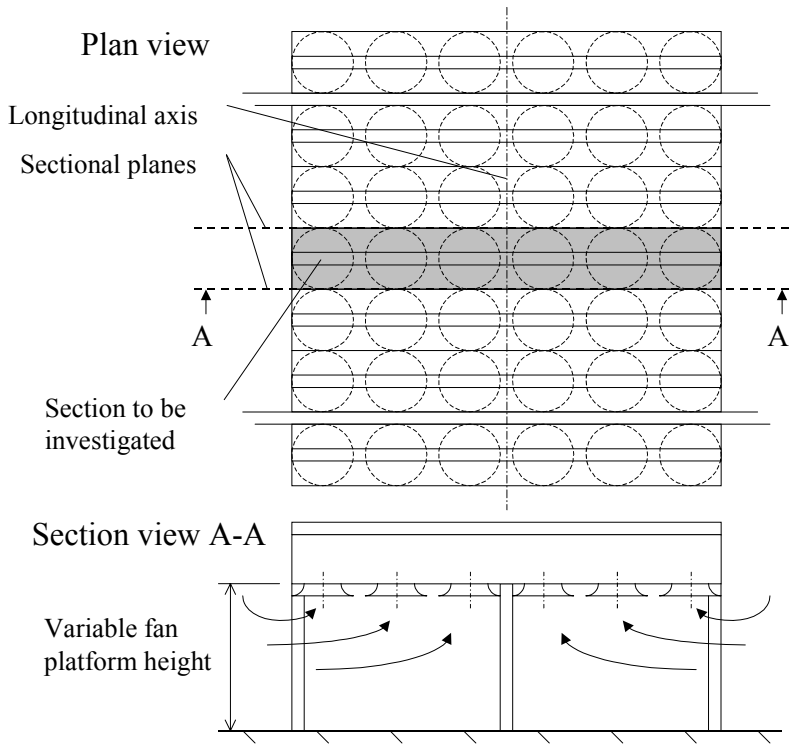

Figure 1.9. A long ACSC bank

Two different rotor-only axial flow fans, schematically shown in Figure 1.10, were investigated. The first fan, hereafter referred to as the *A-fan,* has the following main features: diameter d_F=9.145 m, number of fan blades n_F=8, hub-tip ratio d_h/d_F=0.153, rotational speed N=125 rpm. Such fans are commonly used in general industrial cooling application.

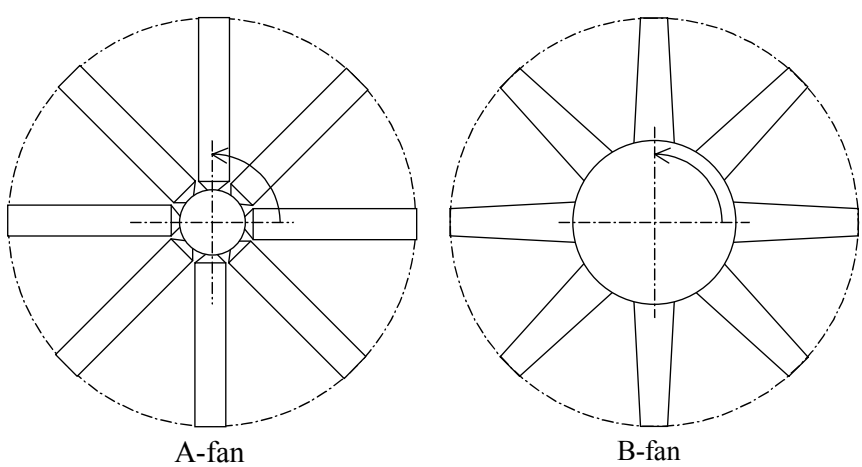

Figure 1.10. Two rotor-only axial flow fans in plan view

The second fan, referred to as the *B-fan,* has the same diameter, number of blades, and rotational speed as the A-fan, but features an enlarged hub with a hub-tip ratio of d_h/d_F=0.4. Bruneau 1994 designed the B-fan with the purpose of application in an existing ACSC. The original fan installation was of the low hub-tip ratio type, similar to the A-fan. A characteristic of these low hub-tip ratio type fans is the recirculation or reverse flow that occurs near the hub, as reported by van Aarde (1990) and Venter (1990).

In the design of the B-fan, the fan efficiency at the required volume flow rate and pressure rise was improved by eliminating the reverse flow effect at the hub region by increasing the hub-tip ratio. The consequences of different blade profiles were also considered. Note that the B-fan in this study refers only to the B2-fan with the NASA GA(W)-2 blade profile in Bruneau (1994).

Salta and Kröger 1995 report a measurable increase in fan performance, specifically the edge or peripheral fan, with the addition of a walkway along the periphery of the ACHE bank. Similar modifications towards improving the fan inlet conditions are considered and evaluated.

In this study a simplified numerical model was used to qualitatively evaluate the fan performance in a section of an ACSC subjected to various levels of inlet flow distortions. The main objectives of this study are summarised as follows:

1. Numerically determining the performance characteristics of two different axial flow fans using a fan model.

2. Evaluation of the effect of cross-draft inlet flow distortions on the performance of fans in a section (or sector) of an ACSC.

3. Comparison of two different types of axial flow fans under distorted inlet flow conditions.

4. Evaluation of performance enhancing walkways and windscreens.

5. Determining whether or not an *essentially two-dimensional* modelling approach can be employed to realistically model a section (or sector) of an ACSC under crosswind conditions.

1.4. Outline

Chapter 2 details a typical fan unit in the ACSC being investigated. Emphasis is on the finned tube heat exchanger bundles and axial flow fan. Reference is also made to the thermal-flow analysis (i.e., energy and draft equation) applicable to the system.

Chapter 3 provides an in-depth discussion of the numerical techniques employed. An overview of the finite volume CFD code is given, with reference to turbulence modelling and discritization schemes. The mathematical formulation of the numerical fan and heat exchanger models is provided.

Chapter 4 focuses on validation of the numerical models developed in the previous chapter. Results obtained from the numerical fan model in a free inlet, free outlet type configuration are compared to experimental data. The combination of the fan and heat exchanger models are also tested in a single isolated fan unit model.

Chapter 5 presents the numerical modelling of a section of the ACSC consisting of six fan units at different platform heights under windless conditions. Various walkway and windscreen configurations, with the purpose of improving the performance of the fans (particularly the peripheral fan) are evaluated. Furthermore, a discussion regarding the validity of the *essentially two-dimensional* modelling approach to the system under consideration is given.

Chapter 6 summarises this study's results. Conclusions are drawn and recommendations are made for future research.

2. System Description

2.1. System Components

The ACSC under consideration consists of an array of fan units as shown in Figure 1.9. A schematic of a typical fan unit found along the edge of the ACSC platform is shown in Figure 2.1.

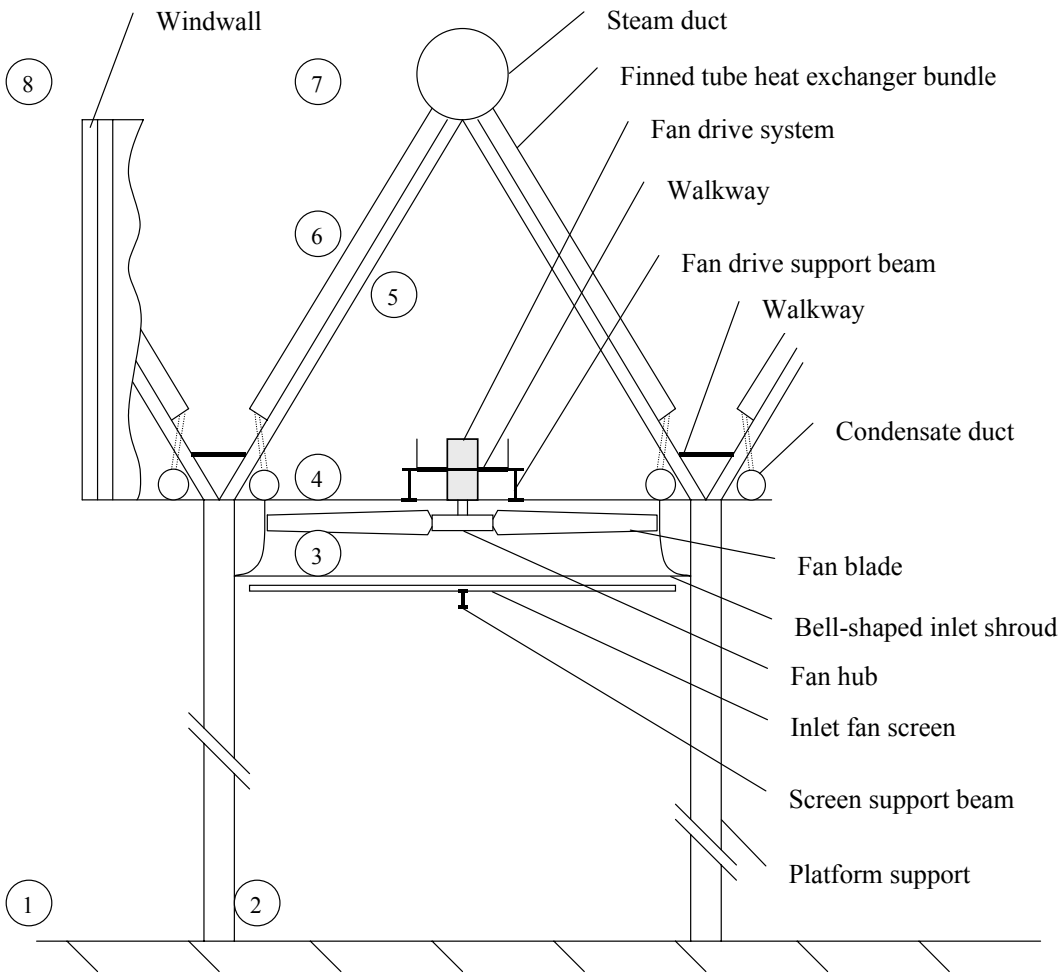

Figure 2.1. A fan unit in an ACSC array

Stagnant ambient air at (1) is accelerated towards the platform supports at (2). Air then flows up into the bell-shaped fan inlet at (3), through the fan, and enters the A-frame plenum at (4). The air then gets heated as it flows through the finned tube heat exchanger bundles between (5) and (6). The hot air then exits the system at (7). Windwalls along the edge or periphery of the ACSC reduce the amount of recirculation, thereby improving the performance of the system. Specifications of the system are given in Appendix A.

2.1.1. Finned tubes

Examples of finned heat exchanger tubes typically used in industrial air-cooling applications are shown in Figure 2.2. These tubes are usually of aluminium or galvanized steel construction in order to prevent corrosion.

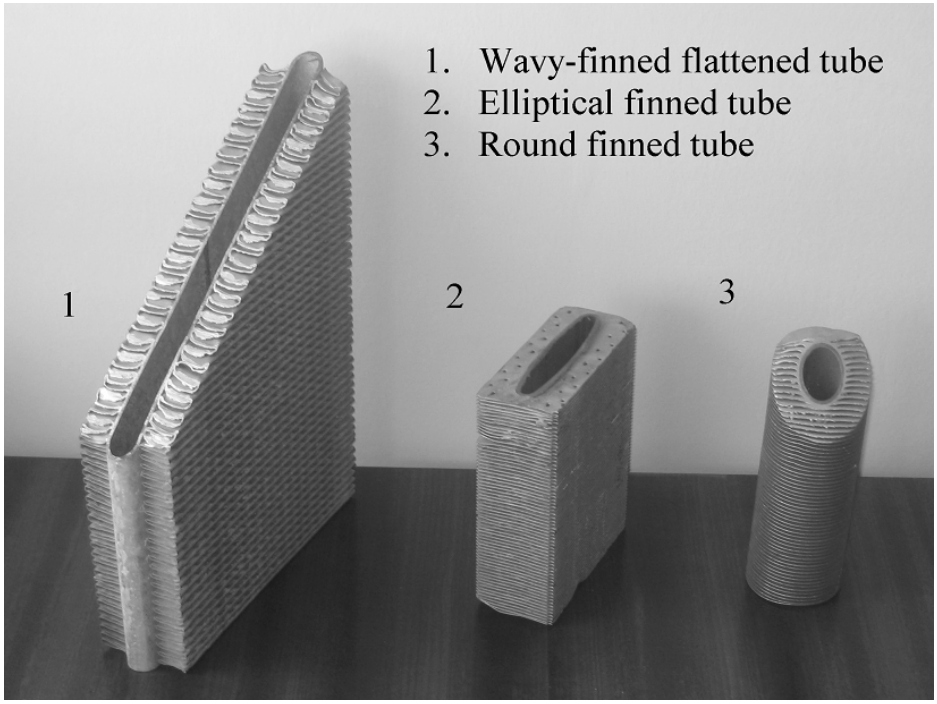

Figure 2.2. Finned tubes used in industrial air-cooling applications

The system under consideration employs two rows of elliptical finned tubes in a staggered arrangement, as shown in Figure 2.3. This tube features an elliptically shaped tube to reduce flow resistance and extended rectangular plate fins to increase the airside heat transfer area. The pressure drop and heat transfer characteristics of the finned tubes, obtained through experimental testing, are given in Appendix A. Each fan unit has 8 heat exchanger bundles consisting of 57 and 58 finned tubes in respectively the first and second tube rows.

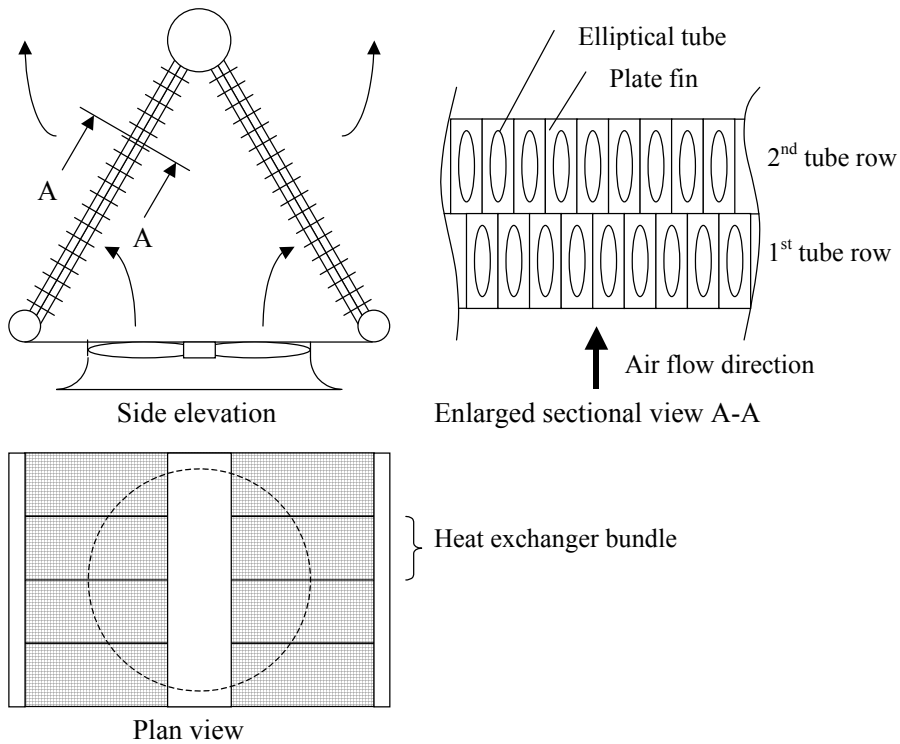

Figure 2.3. Finned tube configuration

2.1.2. Axial flow fans

Axial flow fans are ideally suited for application in ACHEs and ACCs, where high volume flow rates at relatively low pressure rise are required. Figure 2.4 shows some of the fans used in industrial cooling applications.

Figure 2.4. Industrial cooling fans

It can be seen that these fans differ significantly in size and construction. Cost, structural strength, material properties, and noise generation are some of the major considerations in fan selection.

Fan characteristics (i.e., pressure rise, fan shaft power and efficiency) are determined by one of many fan test codes or standards. Whether or not the fan test characteristics are an accurate representation of the fan performance in an actual installation will depend on the ACC or ACHE geometry and operating conditions. Figure 2.5 shows a BS848 (British Standards Institution 1997) Type A fan test facility. Fans investigated in this study were tested according to this code. The test facility and calculation of the fan characteristics are therefore discussed in more detail.

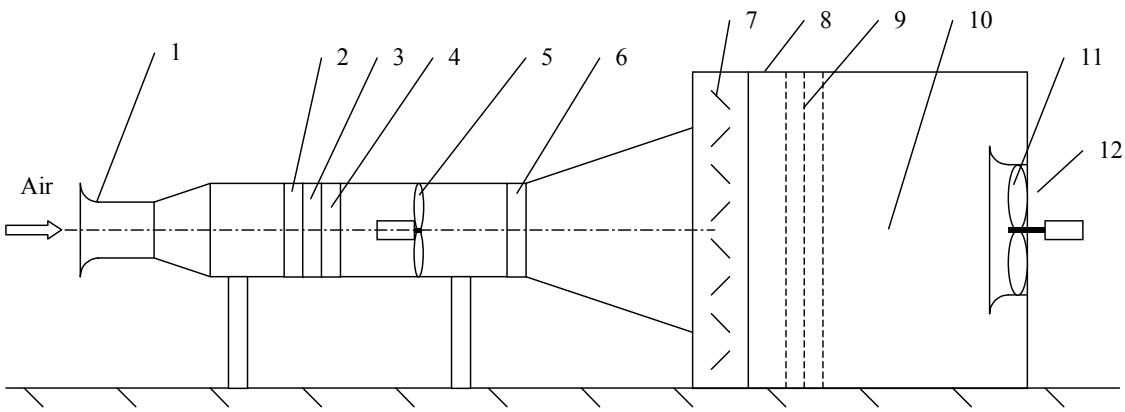

1.	Calibrated bell mouth	7.	Guide vanes
2.	Flow staightener	8.	Rectangular settling chamber
3.	Throttling device	9.	Wire mesh screens
4.	Flow staightener	10.	Measurement of fan inlet conditions
5.	Auxiliary fan	11.	Test fan
6.	Flow staightener	12.	Free atmospheric outlet

Figure 2.5. BS848 (British Standards Institution 1997) Type A fan test facility

The mass flow rate, m_T, through the fan test facility is determined by measuring the relative static pressure just after the calibrated bell mouth inlet (1). The static pressure difference generated by the test fan, Δp_{sc}, is measured at the settling chamber inside wall (10), relative to atmospheric pressure. The air temperature, T_a, is also measured inside the settling chamber. According to the ideal gas equation, the fan test air density is

$$\rho_T = \frac{(p_a + \Delta p_{sc})}{RT_a} \tag{2.1}$$

The volume flow is therefore

$$V_T = \frac{m_T}{\rho_T} \tag{2.2}$$

The dynamic pressure inside the settling chamber (8), is given by

$$p_{dT} = \frac{1}{2\rho_T}\left(\frac{m_T}{A_{sc}}\right)^2 \tag{2.3}$$

Under these test conditions, the fan static pressure is defined as

$$\Delta p_{FsT} = -\Delta p_{sc} - \Delta p_{dT} \tag{2.4}$$

Furthermore the test fan rotational speed and shaft torque, denoted N_T and M_T respectively, are also measured. The fan shaft power is then given by

$$P_{FT} = \frac{2\pi N_T M_T}{60} \tag{2.5}$$

where N_T is in rpm. The fan static efficiency is then defined as

$$\eta_{FsT} = \frac{V_T \Delta p_{FsT}}{P_{FT}} \tag{2.6}$$

It can be seen that the fan characteristics determined according to the aforementioned code are determined for an isolated fan with ideal inlet conditions. Thus, it is important to take note of the following system effects in actual fan installations that may result in measurable deviation from the predicted fan performance:

(a) In an actual fan installation, buildings, wind, and other fans may result in distorted inlet flow conditions, as shown in Figure 1.7. As mentioned, these factors will usually cause a reduction in fan performance due to a combination of increased inlet flow losses and off-axis inlet flow conditions. Stinnes (1998) performed an experimental investigation on the performance of an axial fan subjected to a forced cross-flow component at the inlet. For a cross-flow ratio of 0.5 and 1, he reports reductions in the pressure rise of 4% and 8%, respectively.

(b) As seen in Figure 2.5, air in the settling chamber moves through the test fan and exits to the free atmosphere. In a forced draft ACHE or ACC, air is blown into a confined plenum chamber. In an experimental investigation on an ACHE, Meyer and Kröger (1998) found that a fraction of the kinetic energy at fan outlet is recovered inside the plenum chamber. Neglecting this recovery effect will result in a conservative prediction of the operating point. According to Kröger (2004) however, there is essentially no recovery in an A-frame plenum configuration.

(c) Large fans ranging between 8 meters (m) and 11 m in diameter are often found in ACSC. For obvious reasons, it is impractical to test these fans in a standard test facility. The fan laws are therefore applied to data obtained from a geometrically similar model fan in order to predict the performance of the large fan. In a typical 1:6 scale model operating at the same tip speed as the full-scale fan, the Reynolds number based on the fan blade chord length may range between 6.8×10^4 and 4.5×10^5. In the full-scale model the corresponding Reynolds number will be six times higher, and range between 4.08×10^5 and 2.7×10^6. The lift and drag characteristics of the fan blade profiles are Reynolds number dependent. An increase in Reynolds number is

generally associated with an increase in lift coefficient and a decrease in drag coefficient. The fan laws do not take into account the effect of Reynolds number variation. It can therefore be expected that the performance of a full-scale fan will differ from that predicted by the fan laws. In a numerical investigation Meyer and Kröger (2004) predict that the static pressure rise and fan power are respectively 3% and 4% higher than predicted by the fan laws.

Appendix B provides the fan installation specifications, as well as the fan blade geometry and fan characteristics of the A-fan and B-fan. For the effective interpretation of the fan characteristics and for further reference, a definition of the blade angle is required.

To provide a more uniform outlet velocity, the fan blades are designed with blade twist (i.e., the blade angle, γ, is a function of radius). In this study, if blade angle is measured between the plane of rotation and the chord line, it is denoted by γ_c. In practice however, the blade angle is sometimes referenced to the bottom surface of the fan blade profile in order to facilitate easier adjustment of the blade angle setting. In such a case the blade angle is denoted by γ_p. These two angles are compared in Figure 2.6. When γ_c or γ_p refers to a blade angle setting, a second subscript is added to indicate where the angle is measured, i.e., at the root or at the tip, respectively denoted by r or t. For example, γ_{cr} refers to a blade angle setting referenced to the chord line of a fan blade profile at the blade root.

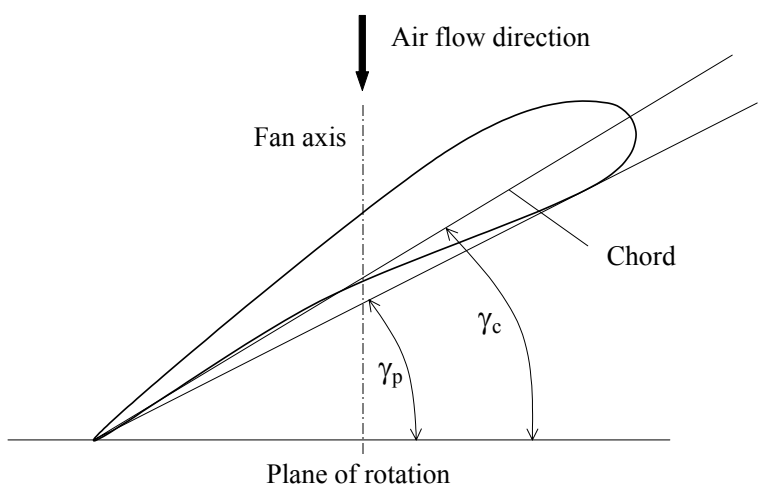

Figure 2.6. Blade angle definition

2.2. Thermal-flow Analysis

An ACSC is designed to condense a required amount of steam under prescribed design conditions. The first consideration in the thermal-flow design of such a system is the design of the heat exchangers so that it is capable of rejecting the required amount of heat to the environment. The second design consideration is the selection of an axial flow fan that will generate the required amount of air mass flow rate at, or near, maximum fan static efficiency. The rate of heat transfer to air is given by the energy equation, whereas the draft equation describes the pressure changes through the ACSC, i.e., equates the pressure rise induced by the fan to the flow losses through the system. In the thermal-flow design or analysis of an ACSC these equations are inherently coupled and must be solved simultaneously.

2.2.1. Energy equation

The heat transfer rate between the condensing steam and the cooling air flowing through a heat exchanger having n_r finned tube rows, for a typical fan unit in a ACSC, is given by the following equation:

$$Q = \sum_{i=1}^{n_r} m_a c_{pa(i)} \left(T_{ao(i)} - T_{ai(i)}\right) = \sum_{i=1}^{n_r} e_{(i)} m_a c_{pa(i)} \left(T_s - T_{ai(i)}\right) \tag{2.7}$$

where $T_{ao(i)}$, $T_{ai(i)}$, and T_s are the air outlet, air inlet, and steam temperatures, respectively. The effectiveness, $e_{(i)}$ of each row is given by:

$$e_{(i)} = 1 - \exp\left(\frac{-UA_{(i)}}{m_a c_{pa(i)}}\right) \tag{2.8}$$

where $UA_{(i)}$ is the overall heat transfer coefficient between the steam and the air. Due to the relatively low thermal resistance of the condensate film, $UA_{(i)}$ is mainly dependent on the air side heat transfer characteristics of the finned tubes.

2.2.2. Draft equation

The air experiences mechanical energy losses as it moves through, or past, upstream and downstream obstacles and heat exchanger bundles. The pressure drop across these components are defined by means of a dimensionless loss coefficient, given by equation 2.9

$$K = \frac{\Delta p}{\frac{1}{2}\rho v^2} \tag{2.9}$$

where Δp, ρ, and v are the pressure drop, air density, and characteristic velocity based on a prescribed cross-sectional area, respectively.

If the vertical temperature and pressure gradients in the stagnant ambient air are neglected, the draft equation according to Kröger (2004) for an ACSC fan unit shown in Figure 2.1, is given by

$$p_{a1} - p_{a7} \approx 0 = K_{ts} \frac{1}{2\rho_{a1}} \left(\frac{m_a}{n_b A_{fr}}\right)^2 + K_{up} \frac{1}{2\rho_{a3}} \left(\frac{m_a}{A_e}\right)^2 - \Delta p_{Fs} + K_{do} \frac{1}{2\rho_{a3}} \left(\frac{m_a}{A_e}\right)^2 + K_{\theta t} \frac{1}{2\rho_{a56}} \left(\frac{m_a}{n_b A_{fr}}\right)^2 \tag{2.10}$$

where K_{ts}, K_{up}, and K_{do} are the loss coefficients for the platform supports, upstream obstacles and downstream obstacles, respectively. $K_{\theta t}$ is the total loss coefficient across the heat exchanger bundles and includes the kinetic energy losses at the outlet of the A-frame array. The total frontal area of the heat exchanger bundles is given by $n_b A_{fr}$, where n_b and A_{fr} are the

number of bundles and frontal area of a single bundle, respectively. A_e is the effective flow area through the fan—i.e., $\pi/4(d_c^2-d_h^2)$—where d_c and d_h are the fan casing and fan hub diameters, respectively. The Δp_{Fs} term in equation 2.10 is the fan static pressure as determined by one of many fan test codes or standards. Fan characteristics determined for a free-inlet, free-outlet type of configuration (e.g., BS848 [British Standards Institution 1997] Type A) are used in the design of forced draft ACHEs and ACCs.

3. Numerical Modelling

3.1. An Overview of the CFD Code

In this study the commercially available CFD code, FLUENT, is used to investigate the flow field in a simplified model of an ACSC.

3.1.1. Governing equations

FLUENT numerically solves the finite volume based, steady-state differential equations for conservation of mass, momentum, and energy, relevant to incompressible viscous fluids, as given in Versteeg and Malalasekera (1995). The general transport equation for a field variable ϕ in a three-dimensional Cartesian coordinate system, is given by

$$\frac{\partial}{\partial x}(\rho u\phi)+\frac{\partial}{\partial y}(\rho v\phi)+\frac{\partial}{\partial z}(\rho w\phi)=\frac{\partial}{\partial x}\left(\Gamma_\phi\frac{\partial\phi}{\partial x}\right)+\frac{\partial}{\partial y}\left(\Gamma_\phi\frac{\partial\phi}{\partial y}\right)+\frac{\partial}{\partial z}\left(\Gamma_\phi\frac{\partial\phi}{\partial z}\right)+S_\phi \qquad (3.1)$$

where u, v, and w are the velocities in the x, y, and z directions, respectively. Furthermore, the terms on the left side are the convection terms, and the first three terms on the right side, the diffusive terms.

The differential equations for continuity, x-momentum, y-momentum, z-momentum, and energy can be obtained by substituting ϕ with 1, u ,v, w and T respectively, and assigning appropriate values to the diffusion coefficient, Γ_ϕ, and source term S_ϕ, as shown in Table 3.1.

Table 3.1. Conservation equations

Equation	ϕ	Γ_ϕ	S_ϕ
Continuity	1	0	0
x-momentum	u	μ_e	$-\frac{\partial p}{\partial x}+\frac{\partial}{\partial x}\left(\mu_e\frac{\partial u}{\partial x}\right)+\frac{\partial}{\partial y}\left(\mu_e\frac{\partial v}{\partial x}\right)+\frac{\partial}{\partial z}\left(\mu_e\frac{\partial w}{\partial x}\right)+F_x$
y-momentum	v	μ_e	$-\frac{\partial p}{\partial y}+\frac{\partial}{\partial x}\left(\mu_e\frac{\partial u}{\partial y}\right)+\frac{\partial}{\partial y}\left(\mu_e\frac{\partial v}{\partial y}\right)+\frac{\partial}{\partial z}\left(\mu_e\frac{\partial w}{\partial y}\right)+F_y$
z-momentum	w	μ_e	$-\frac{\partial p}{\partial z}+\frac{\partial}{\partial x}\left(\mu_e\frac{\partial u}{\partial z}\right)+\frac{\partial}{\partial y}\left(\mu_e\frac{\partial v}{\partial z}\right)+\frac{\partial}{\partial z}\left(\mu_e\frac{\partial w}{\partial z}\right)+F_z$
Energy	T	μ_e/Pr	$\frac{1}{c_p}\left(u\frac{\partial p}{\partial x}+v\frac{\partial p}{\partial y}w\frac{\partial p}{\partial z}+G\right)+F_E$

In Table 3.1 p, T, μ_e, and Pr are the static pressure, temperature, effective viscosity, and Prandtl number, respectively. F_x, F_y, and F_z are external momentum source terms or body forces, such as gravity (e.g., for gravity in the z direction F_x=0, F_y=0, and $F_z=\rho g$). These terms may also contain momentum sink or source terms, with the purpose of modelling devices such as flow resistances and fans. The production term G in the equation for energy is defined as follows:

$$G = \mu_e \left\{ 2\left[\left(\frac{\partial u}{\partial x}\right)^2 + \left(\frac{\partial v}{\partial y}\right)^2 + \left(\frac{\partial w}{\partial z}\right)^2 \right] + \left(\frac{\partial v}{\partial x} + \frac{\partial u}{\partial y}\right)^2 + \left(\frac{\partial v}{\partial z} + \frac{\partial w}{\partial y}\right)^2 + \left(\frac{\partial u}{\partial z} + \frac{\partial w}{\partial x}\right)^2 \right\} \quad (3.2)$$

These equations are integrated over each control volume or cell of a defined computational grid, and then discritized. The result is a set of implicit algebraic equations that can be solved numerically.

The SIMPLE algorithm discussed in Patankar (1980), for pressure correction and pressure-velocity coupling, augments the discritized governing equations.

3.1.2. Turbulence model

Turbulence is modelled using the k-ε model of Launder and Spalding (1974). The semi-empirical transport equations for the turbulent kinetic energy, k, and its dissipation rate, ε, is obtained by adapting equation 3.1, as shown in Table 3.2.

Table 3.2. Transport equations for k-ε turbulence model

Equation	ϕ	Γ_ϕ	S_ϕ
Turbulent kinetic energy	k	μ_e/σ_k	$G - \rho\varepsilon$
Turbulent kinetic energy dissipation rate	ε	μ_e/σ_ε	$\frac{\varepsilon}{k}\left(C_1 G + C_2 \rho\varepsilon\right)$

The effective viscosity, μ_e, is given by

$$\mu_e = \mu + \mu_t \quad (3.3)$$

where μ and μ_t is the molecular viscosity and turbulent eddy viscosity, respectively. The turbulent eddy viscosity is defined as

$$\mu_t = C_\mu \rho \frac{k^2}{\varepsilon} \quad (3.4)$$

The constants used in Table 3.2 and equation 3.4 are given in Table 3.3

Table 3.3. Constants for k-ε turbulence model

C_μ	C_1	C_2	σ_k	σ_ε
0.09	1.44	1.92	1	1.3

3.1.3. Boundary conditions

The governing equations discussed in the previous two sections require boundary conditions in order to be solved numerically. Assigning appropriate boundary conditions and positioning domain boundaries are imperative in any CFD simulation. A discussion of the boundary conditions provided by FLUENT and used in this study are given below.

(a) ***Velocity inlet boundary:*** This condition is used to specify the inlet velocity vector, as well as the temperature and turbulence parameters. The static pressure is not fixed, and is allowed to change to the appropriate value that will satisfy the specified inlet condition.

(b) ***Pressure boundaries:*** This type of boundary condition allows for inflow and outflow across the boundary. For this boundary condition the static pressure, p, at the boundary plane, is specified. When outflow across the boundary occurs, field variables (i.e., velocities, temperature and turbulence parameters) are extrapolated from interior cells. If however inflow occurs, the flow is assumed to be normal to the boundary. In this case the temperature and turbulence parameters need to be specified. This is referred to as a *static pressure boundary*.

FLUENT also allows the user to specify the relative (or gauge) total pressure at the boundary plane in cases where inflow occurs. This is referred to as a *total pressure boundary*. The relative static pressure, p, in this case is then the difference between the specified total pressure, p_{tot}, and dynamic pressure, as given in equation 3.5

$$p = p_{tot} - p_d = p_{tot} - \frac{1}{2}\rho v_{in}^2 \tag{3.5}$$

where v_{in} is the inlet velocity at the boundary face.

(c) ***Outlet boundary:*** Use of this boundary condition specifies a zero diffusion flux for all variables in a direction normal to the boundary face. This boundary condition is typically applied to developed flow where the cross-stream velocity profile is unchanging in the flow direction. Furthermore, an overall mass balance correction is applied.

(d) ***Symmetry boundary:*** This boundary condition is used to model mirror planes, and assumes zero normal velocity and zero normal gradients for all other field variables. Flow across this boundary is therefore not allowed.

(e) ***Wall boundaries:*** Solid surfaces are modelled using this boundary condition. The viscous shear stresses for turbulent flows in the near wall region are calculated by means of the law-of-the-wall, as proposed by Launder and Spalding (1974). This is known as a *zero-slip* condition.

A *slip-wall boundary condition* can be obtained by specifying the surface shear stresses to be zero. Such a boundary is similar to a symmetry condition in the sense that is does not allow flow across the boundary (i.e., the normal velocity is zero). Zero gradients for other field variables will however not be enforced in the case of the *slip-wall* condition.

3.1.4. Discritization schemes

The convective terms in the governing equations are discritized using either the first-order upwind differencing scheme, or the second-order upwind differencing scheme. The first of these schemes is unconditionally bounded and will, according to Patankar (1980), always result in a physically realistic solution. Numerical diffusion is however a disadvantage which

may affect the accuracy of the solution. Higher order accuracy can be obtained by using the second-order upwind differencing scheme. This scheme is however more unstable compared to the first-order scheme, and requires a sufficiently fine computational grid for proper convergence.

3.2. Numerical Models

In the numerical model of the ACSC fan unit, shown in Figure 3.1, objects such as supports, inlet screens, beams, electrical fan drives, and ducting were not modelled.

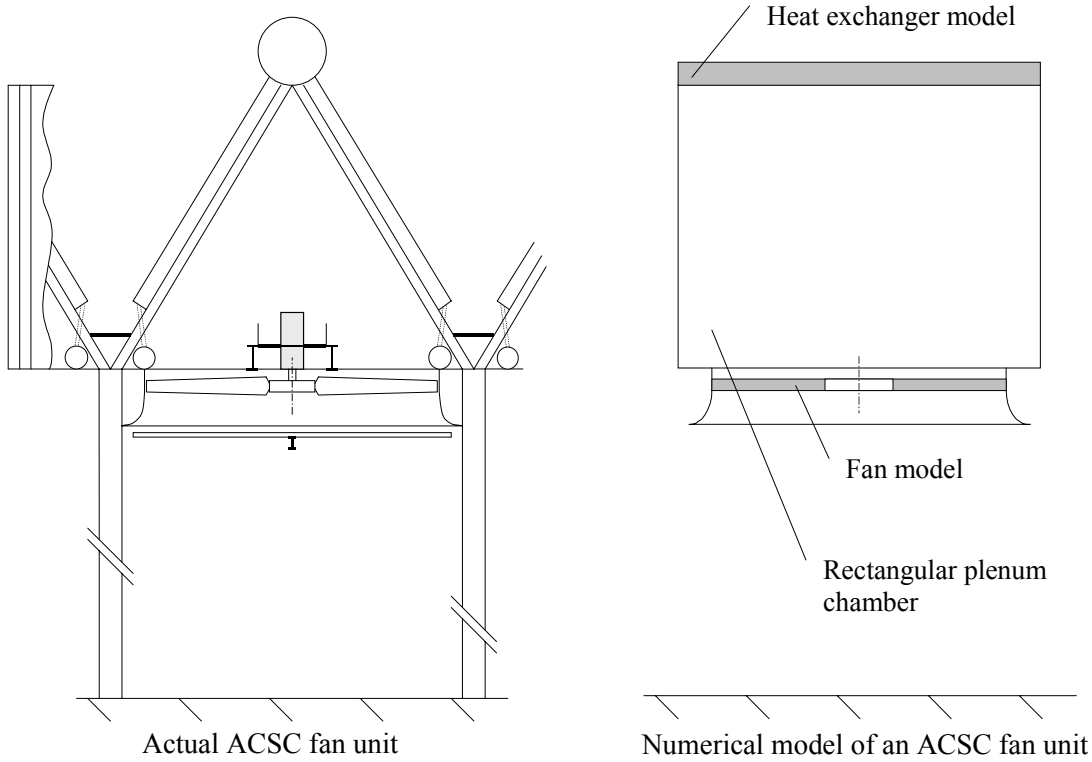

Figure 3.1. Simplified numerical model of a ACSC fan unit

The mechanical energy losses (or pressure drop) resulting from these obstacles were however taken into account in the heat exchanger model, which also includes heat exchanger and outlet losses. This simplification is justified, seeing that the purpose of this study is the investigation of fan performance, and not the detailed modelling of plenum chamber behaviour or outlet flow. Furthermore, the axial fan is simulated using a numerical fan model, which is discussed in more detail in Section 3.2.2.

FLUENT allows the user to specify source terms, material properties and boundary conditions through what is known as user-defined-functions (UDFs). A UDF is computer code written in the C programming language that is capable of accessing data such as field variables, material properties, and system coordinates from the solver. This information is then used to calculate function values (e.g., momentum source terms in a fan model, and return these values to the solver). UDFs were written for the two main components of the ACSC model, namely the heat exchanger and fan model. The mathematical modelling of these two models is discussed in more detail in subsequent sections.

3.2.1. Heat exchanger model

In the numerical heat exchanger model, losses in mechanical energy of the air due to the effective system resistance, as well as heat transfer to the air, are modelled. Based on the draft equation given in equation 2.10, the effective system resistance or pressure drop, Δp_e, for a single fan unit, is given by

$$\Delta p_e = -\left[K_{ts} \frac{1}{2\rho_{a1}} \left(\frac{m_a}{n_b A_{fr}} \right)^2 + K_{up} \frac{1}{2\rho_{a3}} \left(\frac{m_a}{A_e} \right)^2 + K_{do} \frac{1}{2\rho_{a3}} \left(\frac{m_a}{A_e} \right)^2 + K_{\theta t} \frac{1}{2\rho_{a56}} \left(\frac{m_a}{n_b A_{fr}} \right)^2 \right] \tag{3.6}$$

The loss coefficients in equation 3.6 are evaluated in Appendix A. Numerically, this pressure drop is modelled as momentum sink terms in the momentum conservation equations corresponding to the flow direction. FLUENT provides a *porous media condition* where these momentum sink terms are a function of velocity. For the numerical model shown in Figure 3.2, these terms are given in Table 3.4.

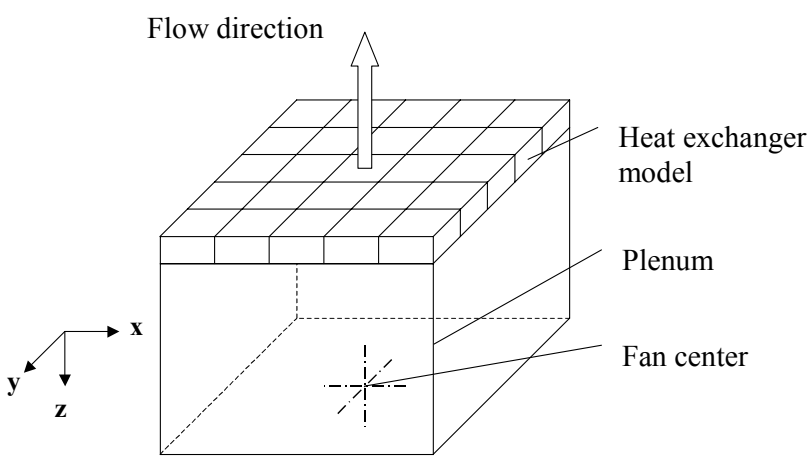

Figure 3.2. Heat exchanger model

Table 3.4. Momentum sink terms for heat exchanger model

Direction	Body force	Momentum sink in N/m^3
x	F_x	$-\left(C_x \frac{1}{2}\rho\lvert\mathbf{v}\rvert u + \frac{\mu}{\alpha_x} u \right)$
y	F_y	$-\left(C_y \frac{1}{2}\rho\lvert\mathbf{v}\rvert v + \frac{\mu}{\alpha_y} v \right)$
z	F_z	$\left(C_z \frac{1}{2}\rho\lvert\mathbf{v}\rvert w + \frac{\mu}{\alpha_z} w \right)$

The momentum sink terms consist of two parts: the viscous resistance term and the inertial resistance term. Therefore, $1/\alpha_i$ and C_i, are respectively the viscous and inertial loss coefficients. For the system under consideration, $1/\alpha_z$ and C_z were determined (see Appendix C) and found to be 1.897×10^6 and 59.1364, respectively. In order to restrict the discharge flow to the primary flow direction, the inertial loss coefficients in the x and y directions are specified to be a thousand times higher than C_z.

Heat transfer to the air is modelled by calculating an energy source term, F_E in W/m^3, based on equation 2.7. Details regarding the calculation of F_E are given in Appendix C.

3.2.2. Numerical fan model

The modelling of ACHEs and ACCs require a fan model in order to generate flow through the system. Various methods for the numerical modelling of axial fans are available. A discussion of these models with reference to the advantages and disadvantages of each model, as well as their practical implementation in a commercial CFD code, is given below:

(a) ***Constant velocity fan model:*** Bender et al. (1996) conducted a numerical investigation on the wind-effects on the intake flow rate of an induced draft counter flow air-cooled heat exchanger. In the two-dimensional numerical model the axial fan was modelled by employing the active structure interior boundary method developed by Schreüder and du Plessis (1990). In this model the fan is modelled by specifying the fan exit velocity corresponding to the desired volume flow rate through the fan. By decoupling the velocity pressure relationship, the velocity remains constant as the pressure correction is implemented. The model does not take into account any three-dimensional flow, or turbulence effects.

(b) ***Constant static pressure fan model:*** In this model a constant static pressure rise is induced by adding source terms to the axial direction momentum equation in the cells defining the axial flow fan. Under ideal inlet conditions this model will result in a constant outlet velocity profile. Furthermore, only an axial velocity component is induced by the pressure jump, therefore no swirl will be generated.

(c) ***Varying static pressure fan model:*** Van Staden (2000) developed an axial fan model intended for the use in modelling the global flow field around a large ACSC. In this model the momentum source terms are calculated from the applicable fan static pressure characteristic curve. This results in an abrupt static pressure rise across the fan corresponding to the volumetric flow rate through the fan. The model is suitable for relatively coarse meshes and is therefore ideal for modelling a large number of axial fans. Once more, only an axial velocity component is produced by this model.

(d) ***Actuator disc model:*** Thiart (1990) developed a numerical fan model for predicting the effect of distorted fan inlet conditions. This model solves the incompressible Navier-Stokes equations, together with the k-ε model for turbulence, and is based on the modelling approach followed by Pericleous and Patel (1986), who modelled the flow field inside a stirred reactor. In this model the effect of the axial flow fan is modelled by momentum source terms, which are calculated using blade element theory. This results in a realistic three-dimensional simulation of the air flow generated by an axial flow fan. Comparison of numerical and experimental results

revealed that numerical predictions of distorted inflow effects on the performance of axial flow fans were good, considering the problem's complexity. This model was also successfully used in numerous other numerical investigations: (Thiart and von Backström 1993; Duvenhage and Kröger 1996; Duvenhage et al. 1996; Coetzee 2000; Meyer 2000; Coetzee and du Toit 2004; Hotchkiss 2004; Meyer and Kröger 2004).

(e) ***Full three-dimensional rotating mesh model:*** Modern CFD codes are capable of directly modelling axial fans and impellers. In this approach, the fan or impeller blades are modelled as solid rotating surfaces in the flow domain. A vector plot of such a model is shown in Figure 3.3. It can be appreciated that a very fine mesh would be required to accurately capture flow effects around the blades. In some CFD codes blade deformation is also taken into account. Because this model is computationally extremely expensive, this approach is only suggested if detail of the flow between the blades is required.

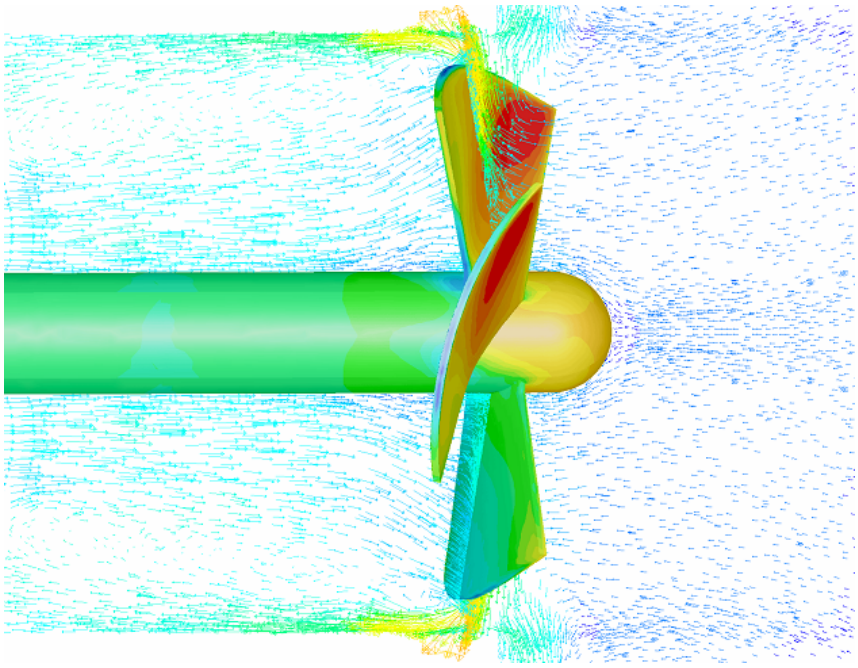

Figure 3.3. Vector plot for a three-dimensional rotating mesh fan model

Due to its relative computationally inexpensive nature and proven use, the actuator disc model was employed in the current investigation.

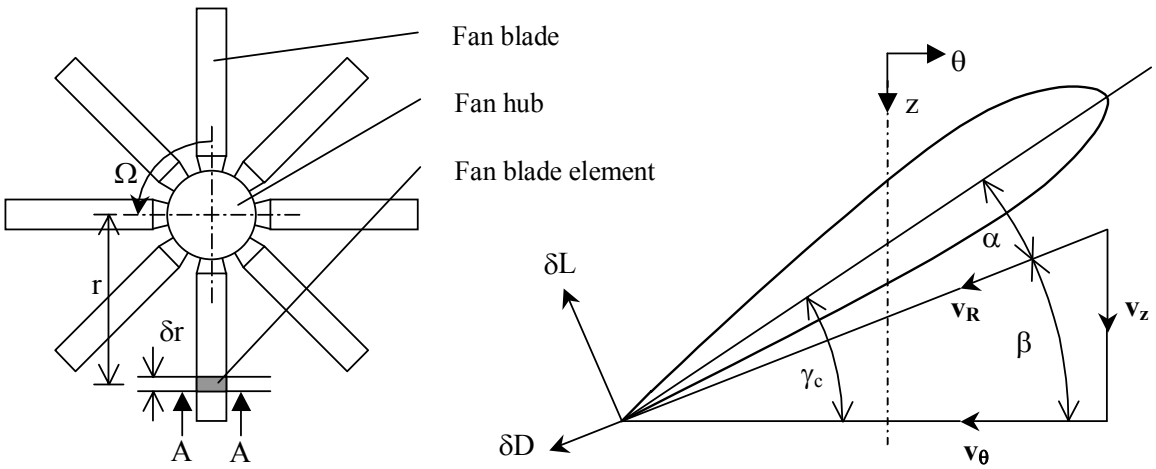

Plan view of axial fan

Enlarged sectional view A-A of fan blade element

Figure 3.4. Fan blade element

According to Wallis (1980) a radial fan blade element, as shown in Figure 3.4, can be considered to be a two-dimensional airfoil section. Therefore, the lift and drag forces imparted on the fluid by the fan blade over a small span, δr, are given by equation 3.7 and equation 3.8, respectively

$$\delta L = \frac{1}{2}\rho\left|\mathbf{v_R^2}\right|C_L c\delta r \tag{3.7}$$

and

$$\delta D = \frac{1}{2}\rho\left|\mathbf{v_R^2}\right|C_D c\delta r \tag{3.8}$$

where $\mathbf{v_R}$, C_L, C_D, and c are the resultant relative air velocity, lift coefficient, drag coefficient, and chord length, respectively (C_L, C_D, and c are defined in Appendix C).

The fan blade element exerts an equal but opposite force on the air. The axial and tangential components of this force can be written in terms of δL and δD

$$\delta f_z = \delta L\cos\beta - \delta D\sin\beta \tag{3.9}$$

and

$$\delta f_\theta = \delta L\sin\beta + \delta D\cos\beta \tag{3.10}$$

The numerical implementation of this model requires a computational grid in the form of a disc with radial and tangential increments, as shown in Figure 3.5.

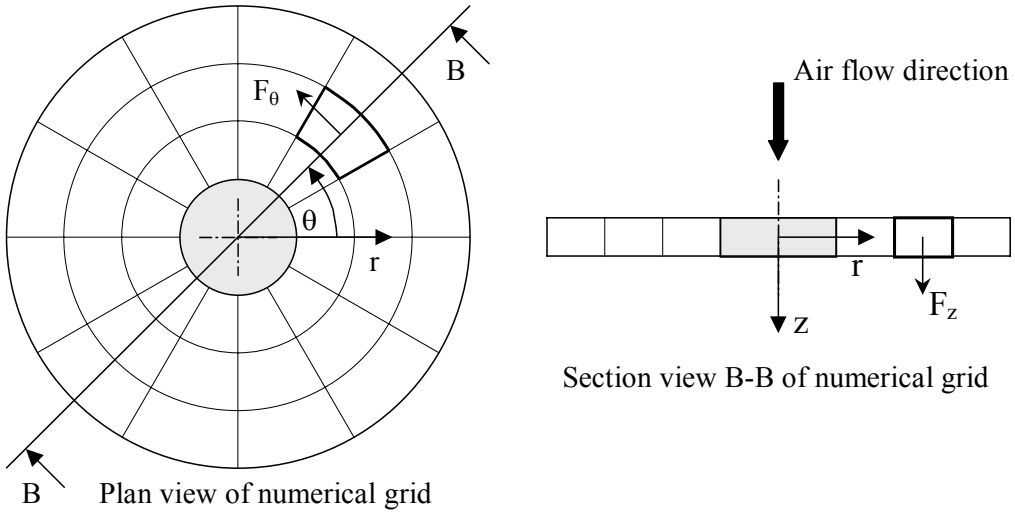

Figure 3.5. Schematic of the computational grid for actuator disc model

The time averaged momentum source terms in the axial and tangential directions are given by

$$F_z = \frac{\delta S_z}{\delta V} = \frac{\sigma \delta S_z}{c \delta r t} \tag{3.11}$$

and

$$F_\theta = \frac{\delta S_\theta}{\delta V} = \frac{\sigma \delta S_\theta}{c \delta r t} \tag{3.12}$$

where σ and t denote the blade solidity and axial thickness of the fan rotor model, respectively. The blade solidity serves as a time averaging factor, and is given by

$$\sigma = \frac{n_b c}{2\pi r} \tag{3.13}$$

where n_b is the number of blades.

By substituting equations 3.7 to 3.10 into equations 3.11 and 3.12, the final expressions for the momentum source terms are obtained

$$F_z = \frac{1}{2}\rho \left|\mathbf{v}_\mathbf{R}^2\right| \frac{\sigma}{t}\left(C_L \cos\beta - C_D \sin\beta\right) \tag{3.14}$$

and

$$F_\theta = \frac{1}{2}\rho \left|\mathbf{v}_\mathbf{R}^2\right| \frac{\sigma}{t}\left(C_L \cos\beta + C_D \sin\beta\right) \tag{3.15}$$

The fan shaft torque and power are respectively given by equation 3.16 and equation 3.17,

$$M = \int_V F_\theta r dV = \sum_{i=1}^{n} F_{\theta(i)} r_{(i)} dV_{(i)} \tag{3.16}$$

and

$$P_F = M\Omega \tag{3.17}$$

In turbo machinery the convention is that the drag force on a blade element acts in a direction parallel to the mean relative velocity vector, as shown in the velocity diagram in Figure 3.6.

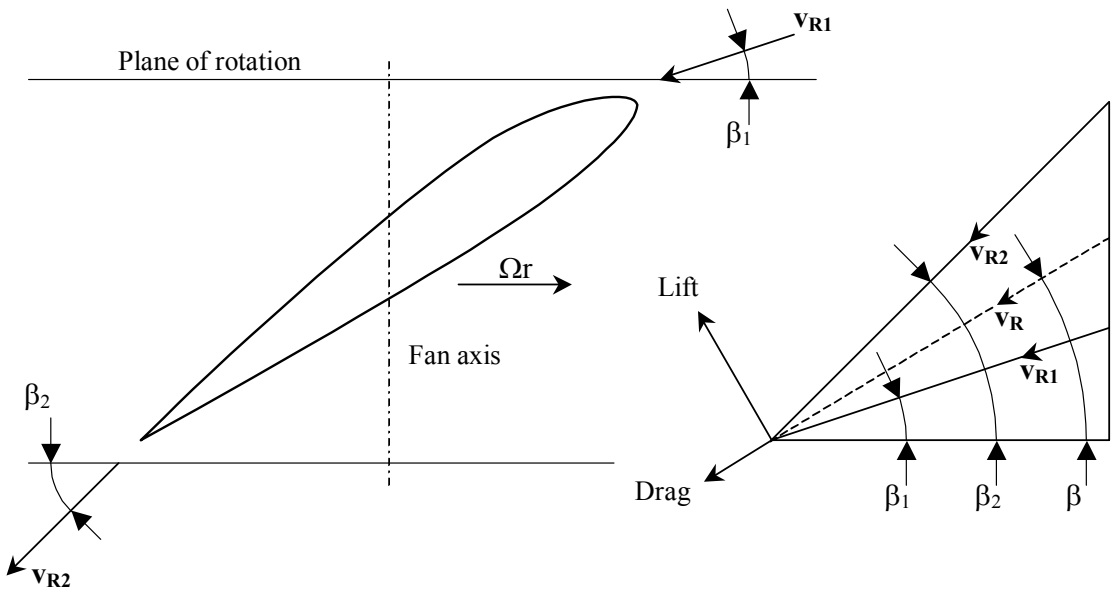

Figure 3.6. Velocity diagram of fan blade element

The relative velocity vector, $\mathbf{v_R}$, in equations 3.14 and 3.15, is therefore the average between the upstream and downstream relative velocity vectors. In the actuator disc model, $\mathbf{v_R}$ in each cell is calculated by taking the average of the velocities in the corresponding upstream and downstream cells, as shown in Figure 3.6.

With the method for the calculation of $\mathbf{v_R}$ determined**,** it only remains to specify the lift and drag coefficients. According to Wallis (1980), in an impeller with low blade number and therefore low solidity, the interference between blades can be neglected so that the blade can be assumed to act alone in a free stream. Therefore, for the modelling of the low solidity fans investigated in this study, isolated blade profile or airfoil data is used.

With regards to the placement of the upstream and downstream discs in the flow domain, it was found that a distance of approximately half a chord length, respectively upstream and downstream of the actuator disc model, yielded best results with the use of isolated airfoil data.

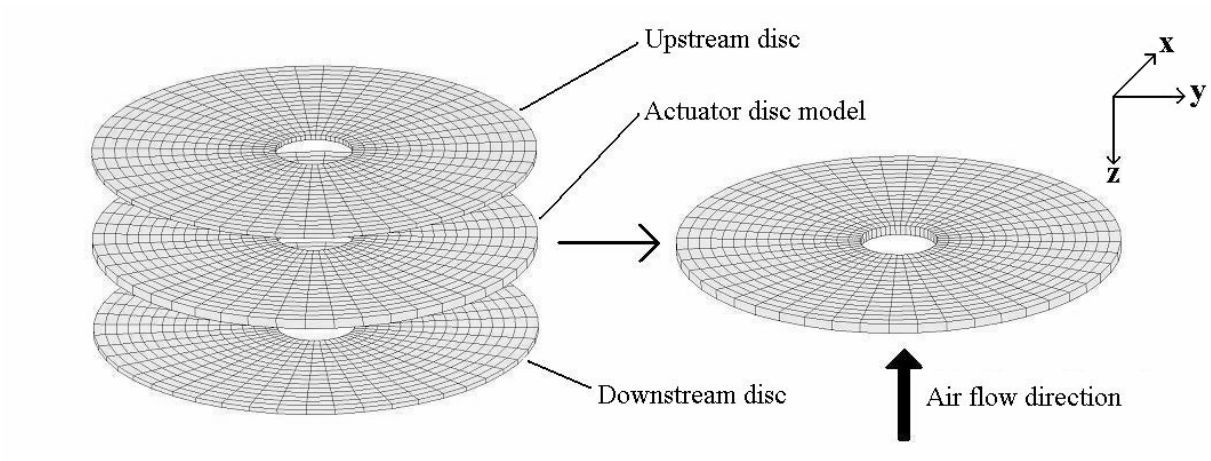

Figure 3.7. Computational grid for actuator disc model

In this study, both the A-fan and the B-fan was modelled using the actuator disc theory discussed above. The corresponding fan blade geometry (i.e., chord length and blade angle variation) and the fan blade profile characteristics (i.e., lift and drag coefficient data), required in the modelling, are respectively given in Appendix B and Appendix D.

4. Evaluation of Numerical Models

4.1. Evaluation of the Numerical Fan Model

This section is concerned with the numerical testing and validation of the actuator disc model that was used to simulate the effect of an axial flow fan. The actuator disc model was implemented in a free inlet/free outlet type configuration in order to numerically predict fan performance—i.e., fan static pressure (Δp_{Fs}), fan shaft power (P_F), and fan static efficiency (η_{Fs})—for a range of flow rates. The numerically predicted fan characteristics are compared to data provided by the manufacturer in the case of the A-fan, and to experimental data measured by Stinnes (1998) in the case of the B-fan.

4.1.1. Computational aspects

The layout and dimensions of the computational grid used in determining the free inlet/free outlet fan characteristics are shown in Figure 4.1.

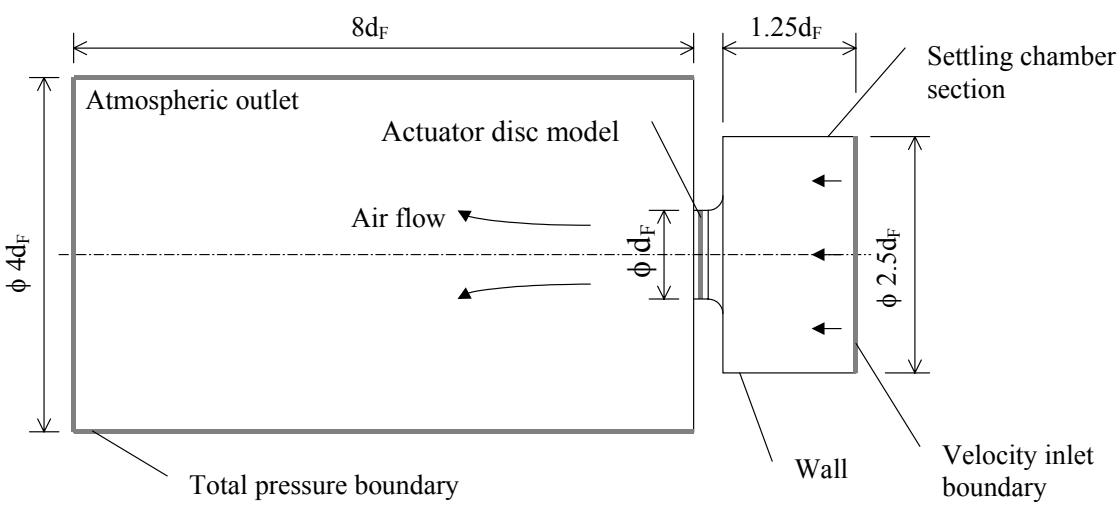

Figure 4.1. Geometrical layout of fan test model computational grid

The dimensions of the settling chamber section correspond to dimensions set out in BS848 (British Standards Institution 1997). The computational grid consisting of 134,000 cells is shown in figures 4.2 to 4.4.

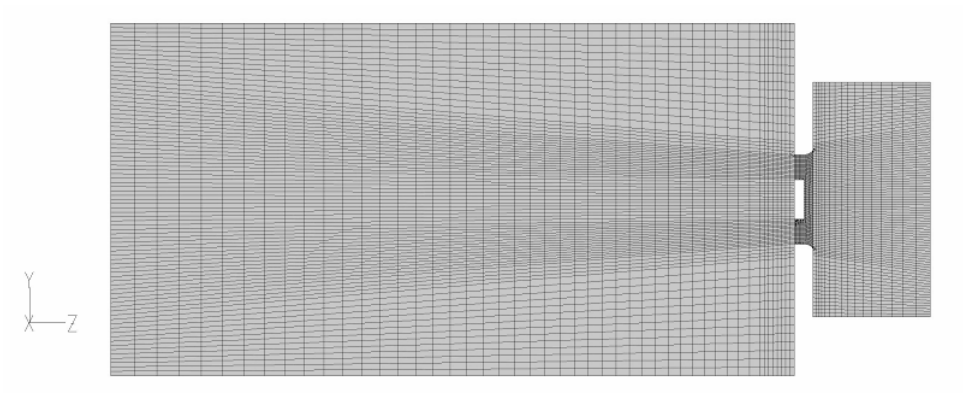

Figure 4.2. Section view of the computational grid for fan test model

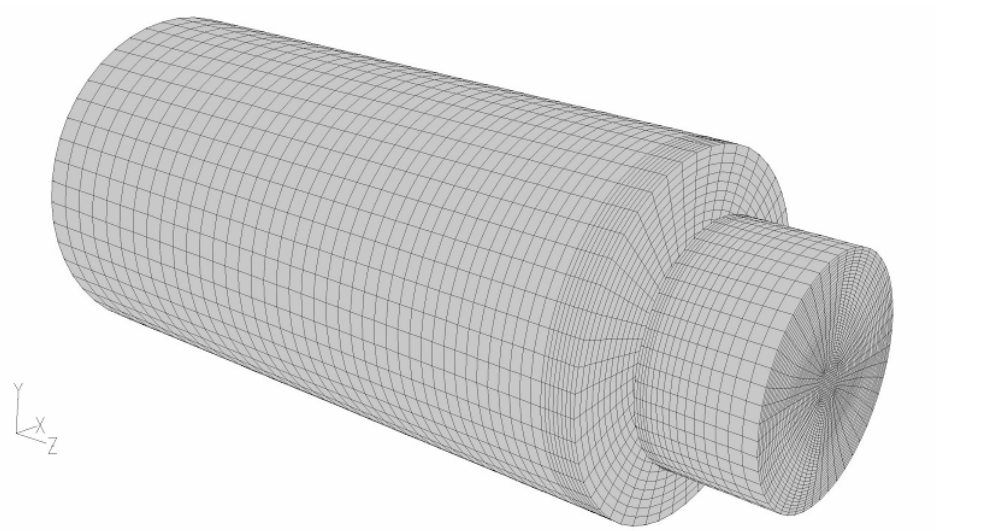

Figure 4.3. Isometric view of the computational grid for fan test model

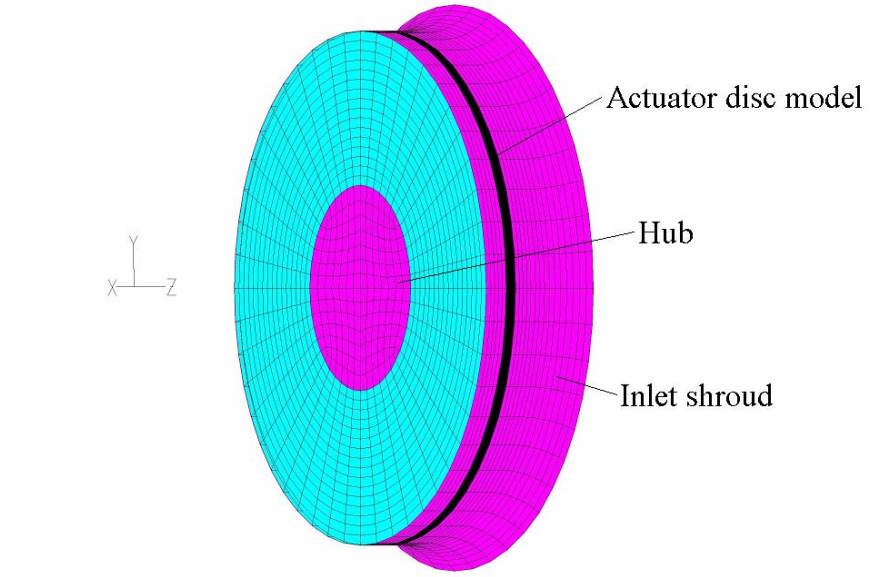

Figure 4.4. Detail view of the computational grid at the fan inlet

The atmospheric outlet boundary, shown in Figure 4.1, was modelled by specifying a total pressure boundary condition (p_{tot}=0). The flow rate through the system was determined by specifying a uniform inlet velocity boundary condition at the inlet of the settling chamber section. By varying the inlet velocity, the numerically predicted fan characteristics could be determined for a range of flow rates. The fan inlet shroud and hub was modelled as a zero-slip wall condition. In the numerical modelling of an ACHE, Coetzee (2001) used the unconditionally bounded first-order upwind differencing scheme in order to maintain numerical stability. For the same reason, this scheme was also employed in the modelling of the ACSC and its components in the current investigation. Furthermore, the flow was assumed to be isothermal, incompressible, and time independent. Convergence of the mass flow rate to the sixth significant digit was established after approximately 1000 iterations.

Typical static pressure contour plots for the A-fan and B-fan models, operating at near maximum fan static efficiency, are shown in Figure 4.5 and Figure 4.6, respectively.

Figure 4.5. Static pressure (Pa) plot for A-fan numerical model (d_F=9.145 m, γ_{pt}=16°)

Figure 4.6. Static pressure (Pa) plot for B-fan numerical model (d_F=1.542 m, γ_{cr}=31°)

The corresponding vector plots of the flow field through the fan models are shown in Figure 4.7 and Figure 4.8.

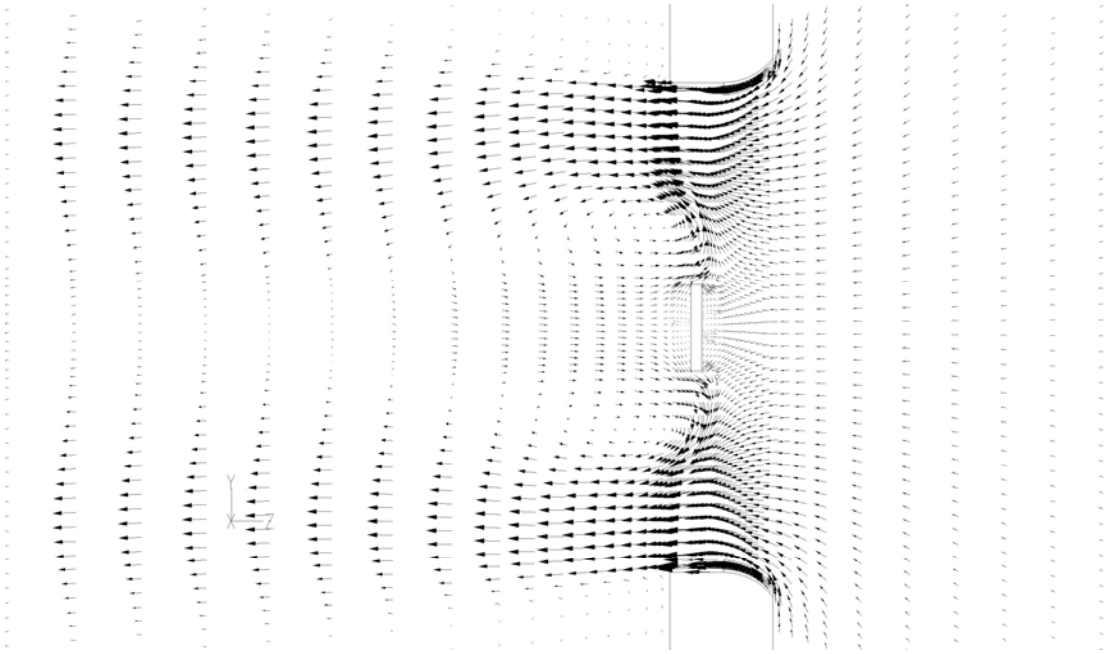

Figure 4.7. Vector plot for A-fan numerical model (d_F=9.145 m, γ_{pt}=16°)

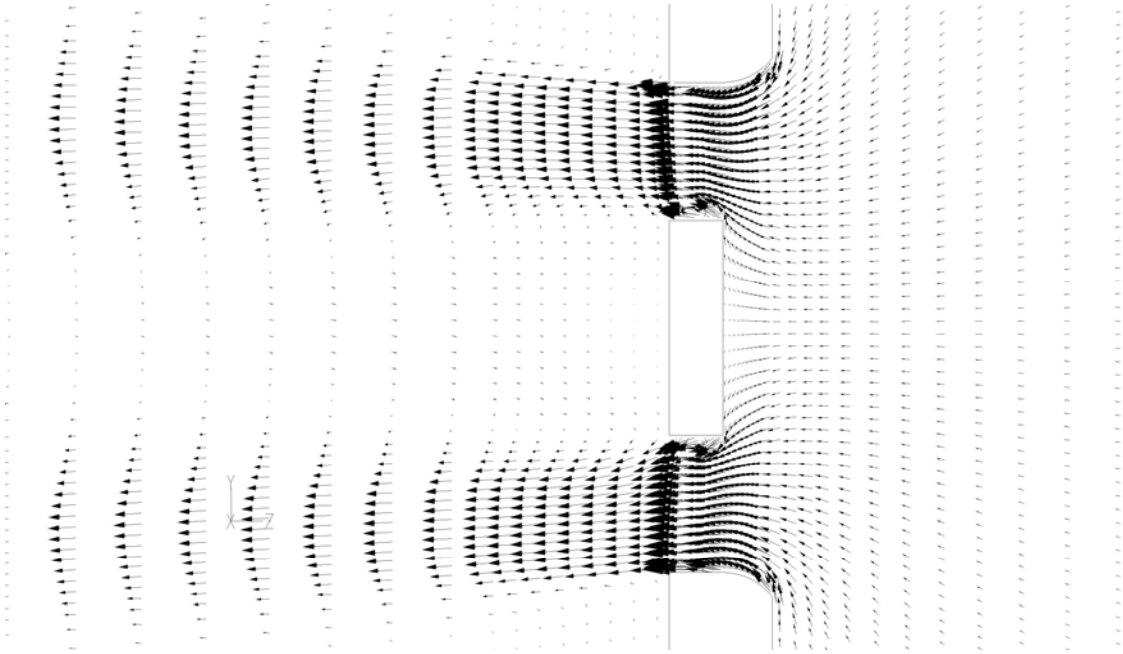

Figure 4.8. Vector plot for B-fan numerical model (d_F=1.542 m, γ_{cr}=31°)

4.1.2. Numerically predicted fan characteristics: A-fan

Numerically determined fan static pressure, fan shaft power, and fan static efficiency for the A-fan are compared to data provided by the manufacturer (given in Appendix B), in figures 4.9 to 4.11, respectively.

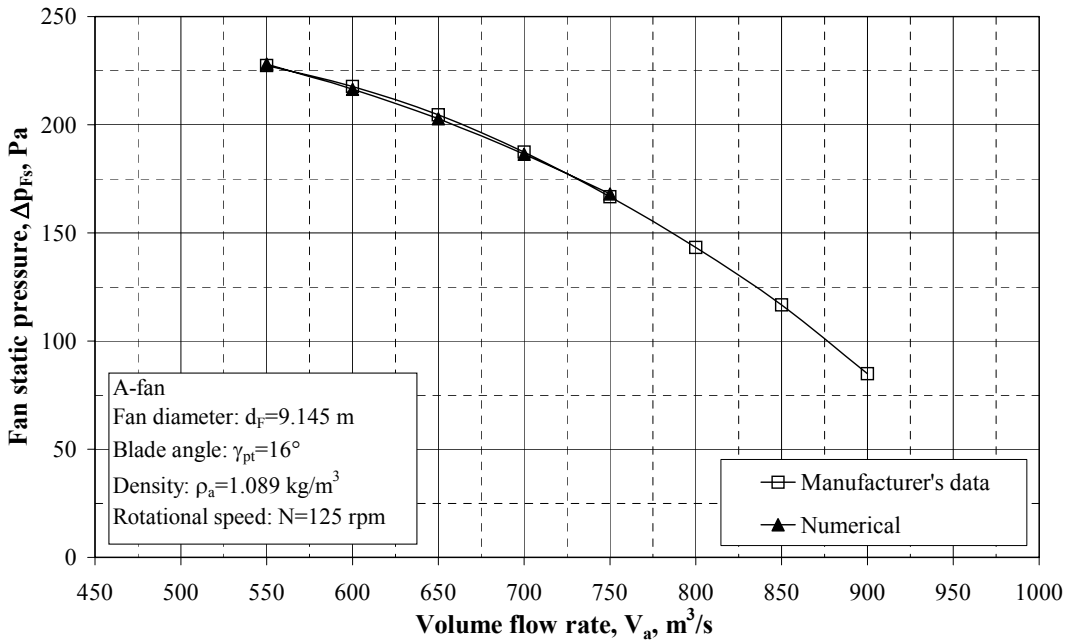

Figure 4.9. Fan static pressure for A-fan (d_F=9.145 m, γ_{pt}=16º)

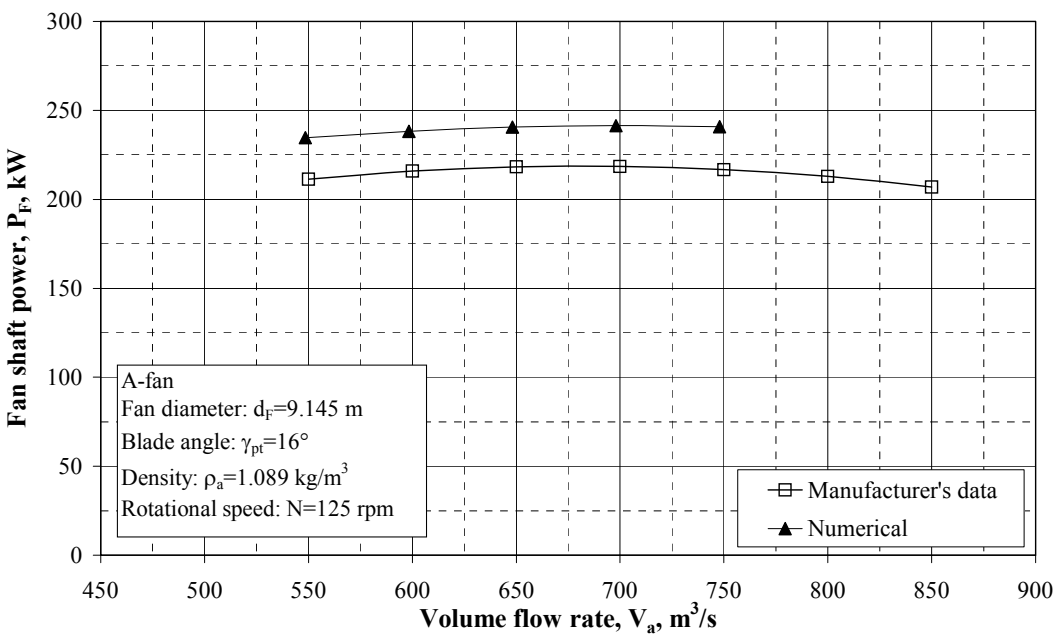

Figure 4.10. Fan shaft power for A-fan (d_F=9.145 m, γ_{pt}=16º)

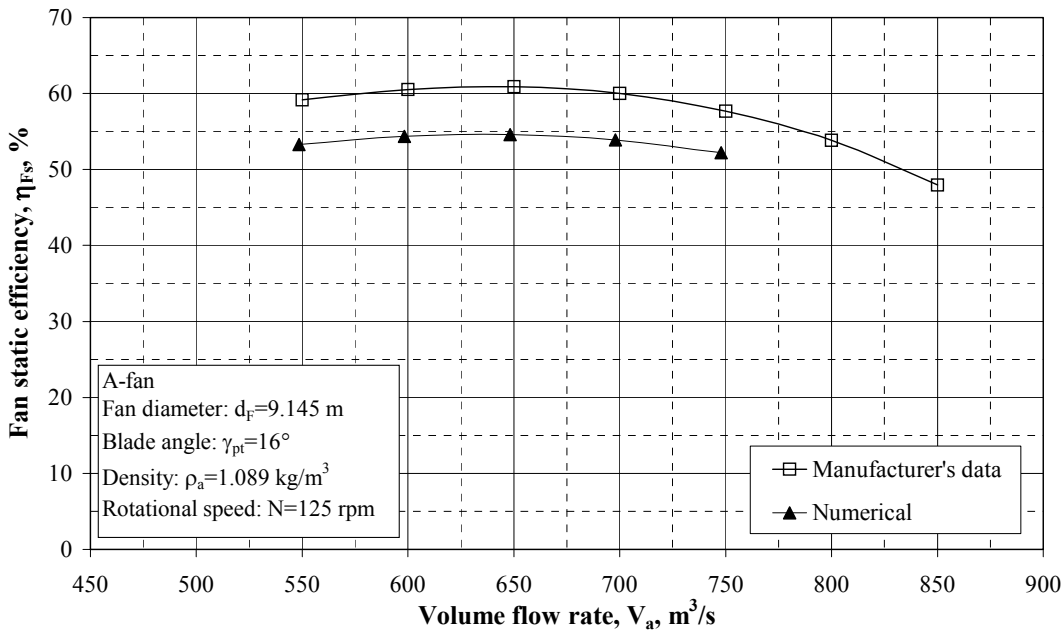

Figure 4.11. Fan static efficiency for A-fan (d_F=9.145 m, γ_{pt}=16°)

4.1.3. Numerically predicted fan characteristics: B-fan

Numerically determined fan static pressure, fan shaft power and fan static efficiency for the B-fan are compared to the experimental data measured by Stinnes (1998) (given in Appendix B), in figures 4.12 to 4.14.

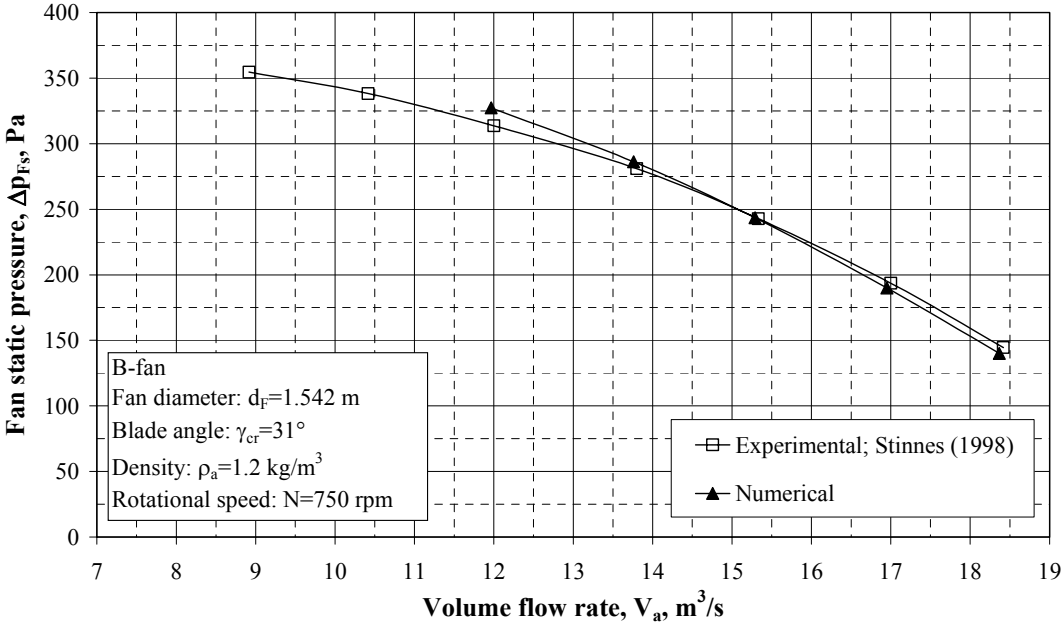

Figure 4.12. Fan static pressure for B-fan (d_F=1.542 m, γ_{cr}=31°)

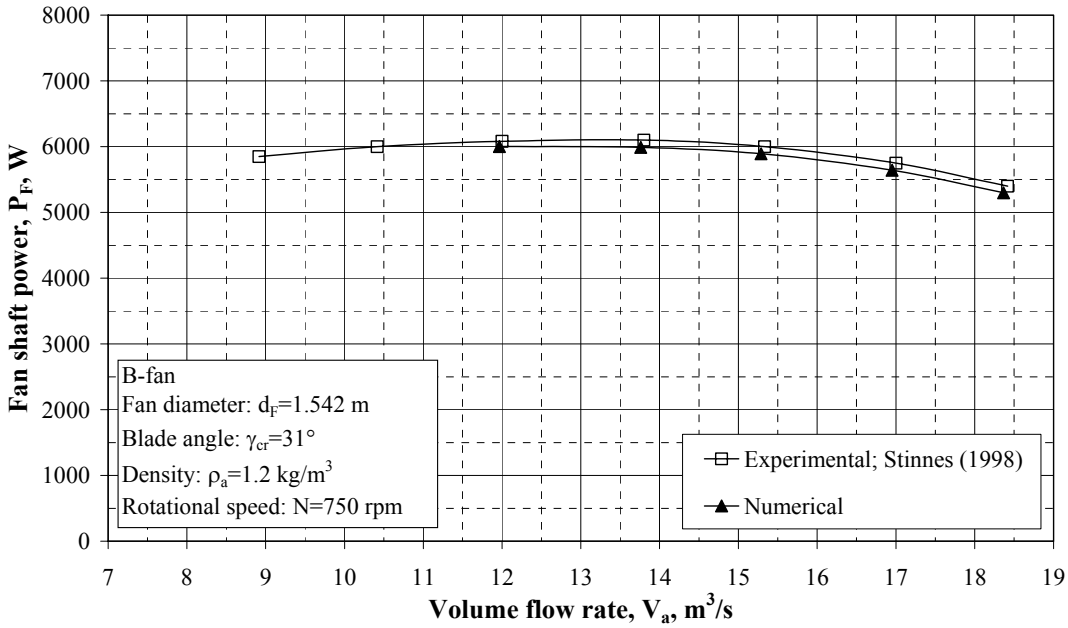

Figure 4.13. Fan shaft power for B-fan (d_F=1.542 m, γ_{cr}=31º)

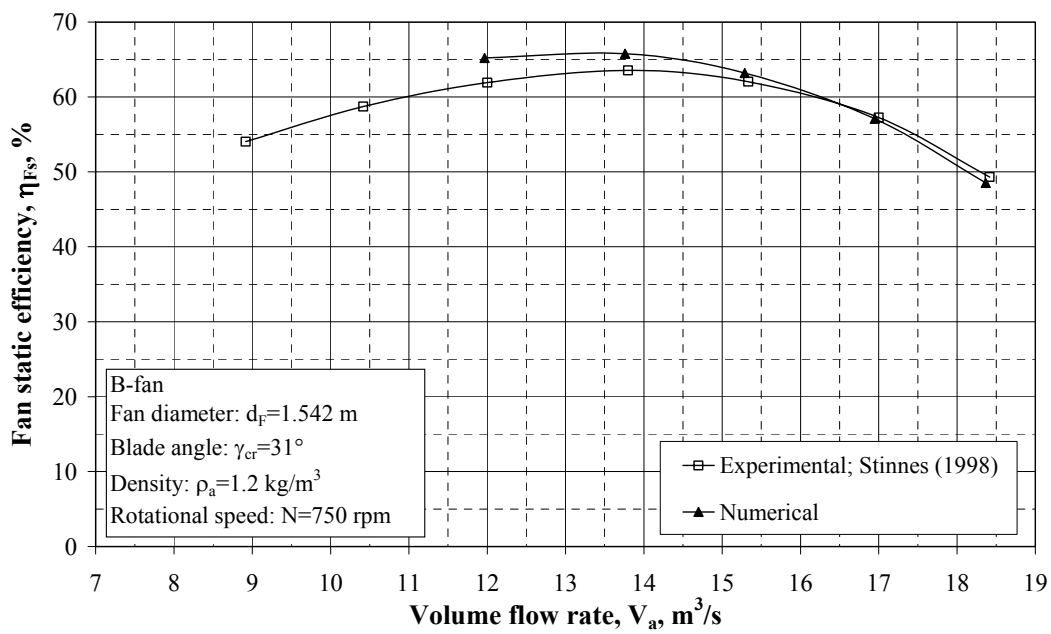

Figure 4.14. Fan static efficiency for B-fan (dF=1.542 m, γ_{cr}=31º)

4.2. Evaluation of a Freestanding Fan Unit

In this section the combination of the numerical fan and heat exchanger models is evaluated for a single freestanding fan unit model. For the ACSC under consideration, a typical blade angle setting for the commercially available A-fan, is γ_{pt}=16º. In further numerical modelling of the A-fan, this particular blade angle setting is used. The expected operating point of the

fan unit model can be found where the effective system resistance curve, defined by equation 3.6, intersects the appropriate fan static pressure curve, as shown in Figure 4.15. In order to compare the performance of the prototype B-fan to the A-fan, both fans are required to have the same diameter and operating point. By numerically modelling the B-fan with a diameter of d_F=9.145 m, it was found that a blade angle setting of γ_{cr}=34.5º resulted in approximately the same operating point being obtained as in the case of the A-fan with γ_{pt}=16º, as shown in Figure 4.15.

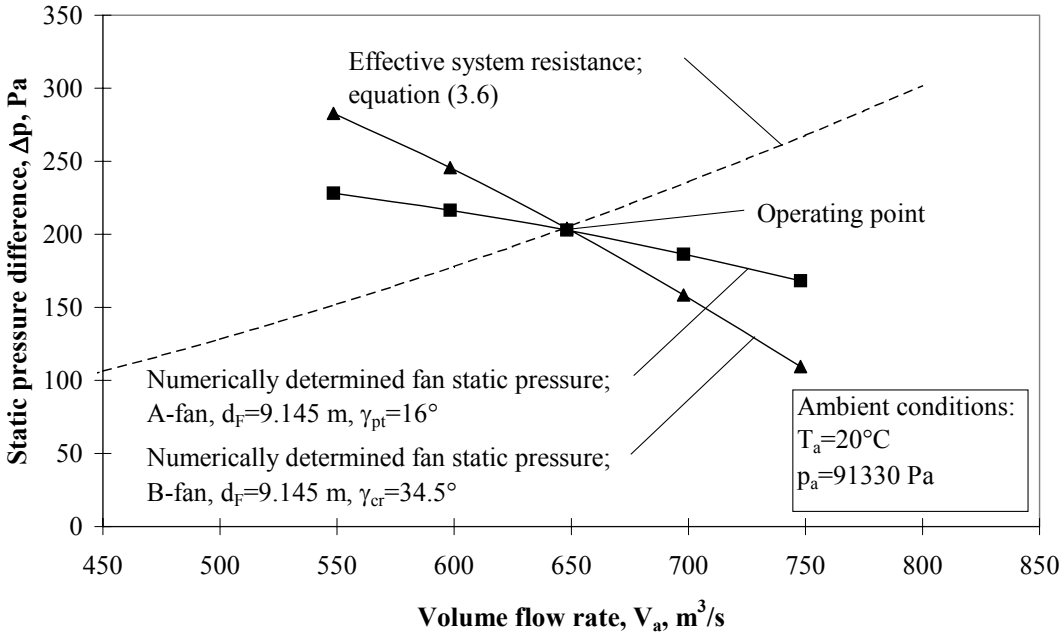

Figure 4.15. Operating point for the numerical ACSC fan unit model

4.2.1. Computational aspects

The geometric layout of the computational grid used to model a freestanding fan unit is shown in Figure 4.16.

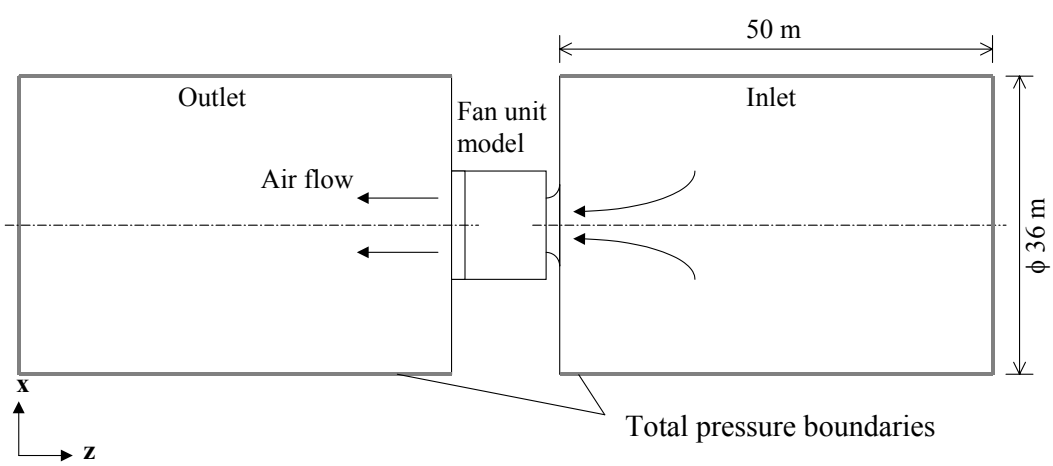

Figure 4.16. Geometrical layout of the computational grid used to evaluate the ACSC fan unit model

The geometry of the fan unit model shown in Figure 4.17 is based on the dimensions of the actual ACSC given in Appendix A. Dimensions of the inlet shroud are given in Appendix B.

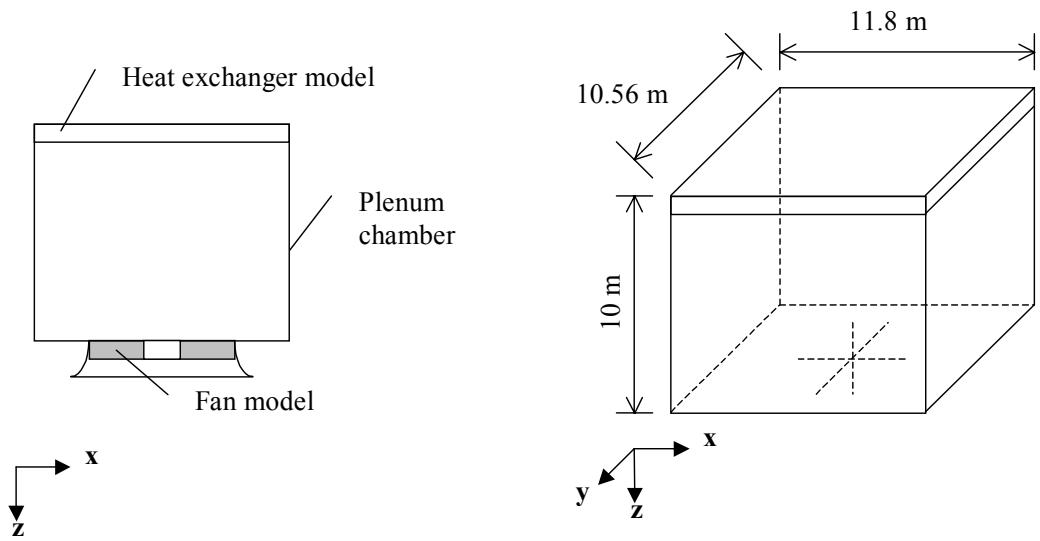

Figure 4.17. Dimensions of numerical the ACSC fan unit model

Detail of the computational grid consisting of 152,000 cells is shown in figures 4.18 to 4.20.

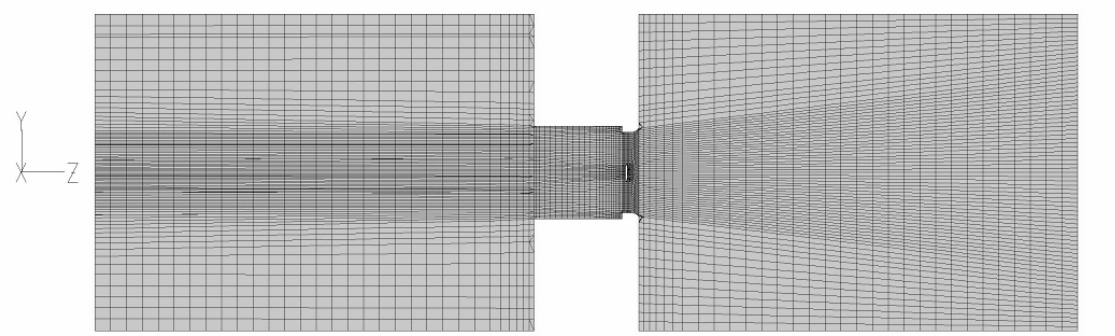

Figure 4.18. Section view of the computational grid for fan unit model

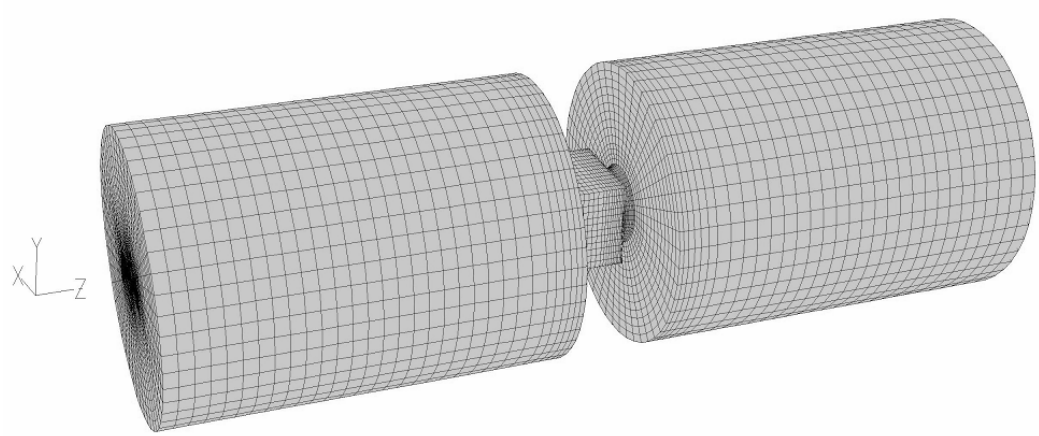

Figure 4.19. Isometric view of the computational grid for fan unit model

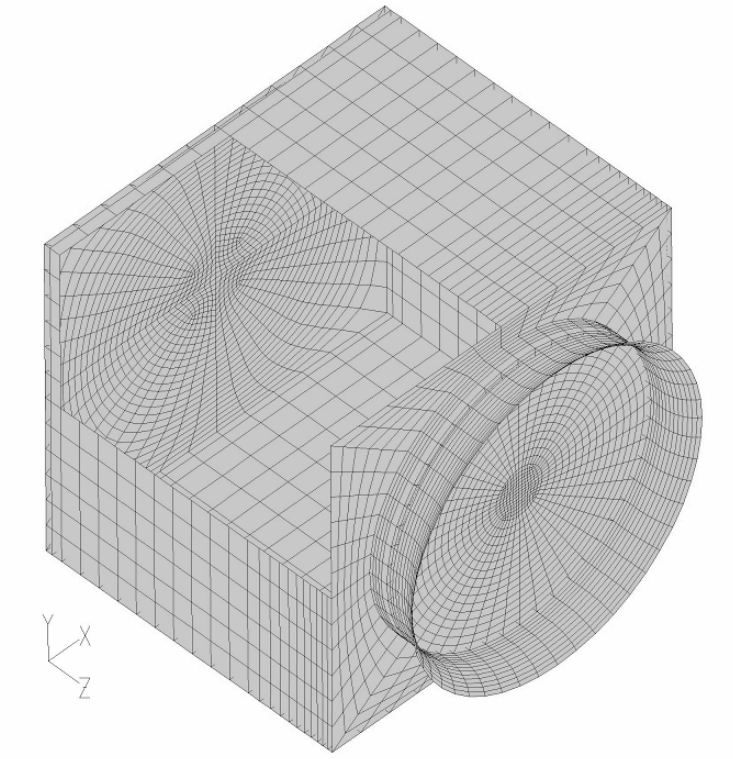

Figure 4.20. Detail view of the computational grid for fan unit model

The inlet and outlet boundaries, shown in Figure 4.16, were modelled by specifying a total pressure boundary condition, with p_{tot}=0. The flow of air through the fan unit model was therefore generated by the actuator disc model, and not the specified boundary conditions. The fan inlet and plenum chamber walls were specified as zero-slip walls. Convergence of the mass flow rate to the sixth significant digit was established after approximately 700 iterations. The resulting static pressure contour plots inside the plenum, for the A-fan and the B-fan, are shown in Figure 4.21 and Figure 4.22, respectively.

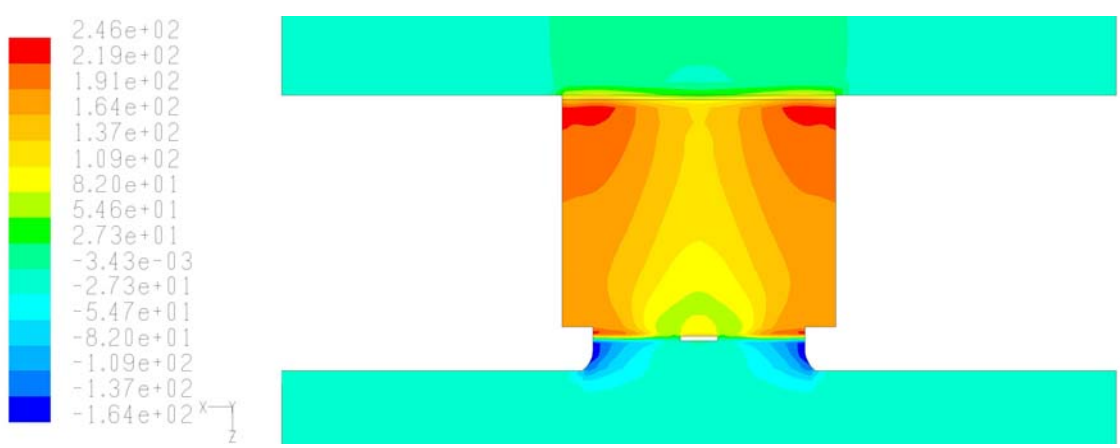

Figure 4.21. Static pressure (Pa) plot in the ACSC fan unit model with A-fan

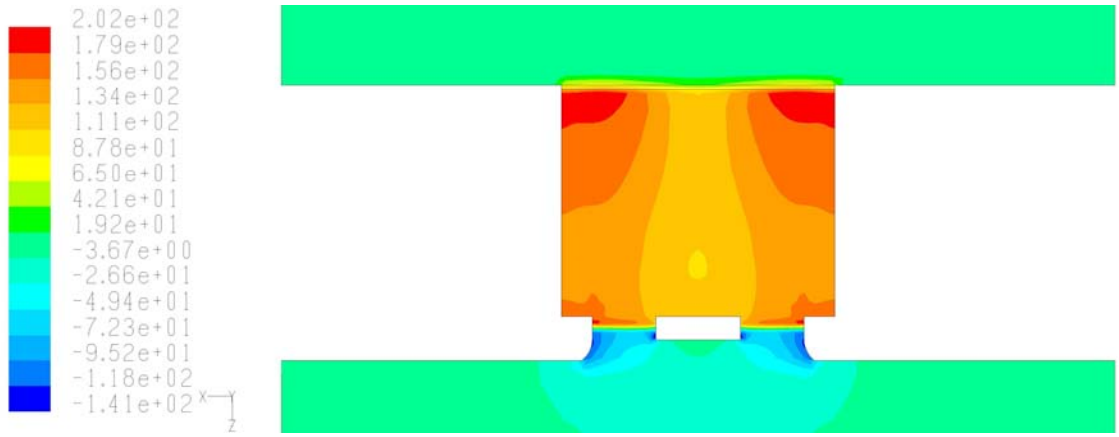

Figure 4.22. Static pressure (Pa) plot in the ACSC fan unit model with B-fan

4.2.2. Numerical results

A fan unit of the ACSC under consideration, employing both the A-fan and the B-fan, were modelled. For the given ambient conditions, and with the effective system resistance defined by equation 3.6, the volume flow rates for the A-fan and B-fan were 653.88 cubic meters per second (m^3/s) and 659.49 m^3/s, respectively. If heat transfer to the air is modelled, the corresponding heat rejection rates are, 22.32 MW and 22.52 MW. This simplified model of a fan unit can now be used to simulate the flow field in a section of ACSC array, consisting of multiple fan units.

4.3. Discussion of Results

The numerically predicted fan static pressure (Δp_{Fs}) and fan shaft power (P_F) for the A-fan differed by 0.7% and 10.6%, respectively, from the data provided by the manufacturer. For the B-fan, the numerically predicted Δp_{Fs} and P_F deviated by 2.5% and 1.8%, respectively, from the experimental data of Stinnes (1998). The fan static efficiency (η_{Fs}) of both fan models showed trends similar to the corresponding experimentally determined efficiency.

Except for P_F of the A-fan model, the numerically predicted fan characteristics compare exceptionally well to experimental data. In part, the aforementioned discrepancy in fan power may be attributed to the fact that, to date, fan manufacturers have used fan similarity laws to scale up the performance characteristics obtained from a scale model fan. This scaling effect was discussed in more detail in Section 2.1.2.

The recirculation or reverse flow that occurs near the hub of the commercially available A-fan, as reported by van Aarde (1990) and Venter (1990), can clearly be seen in Figure 4.7. This phenomenon is however absent in the B-fan, as expected.

The flow rates predicted for the freestanding fan units are used as reference values when evaluating fan performance under distorted inlet conditions in a section of the ACSC array.

5. Fan Performance in a Section of the ACSC

5.1. Windless Conditions at Various Platform Heights

In this part of the study, the numerical modelling of the flow about and through a section of an ACSC under windless conditions, is considered. The ACSC consists of six long adjacent fan rows. The section under investigation, shown in Figure 5.1, is representative of the fan units located near the centre of the ACSC.

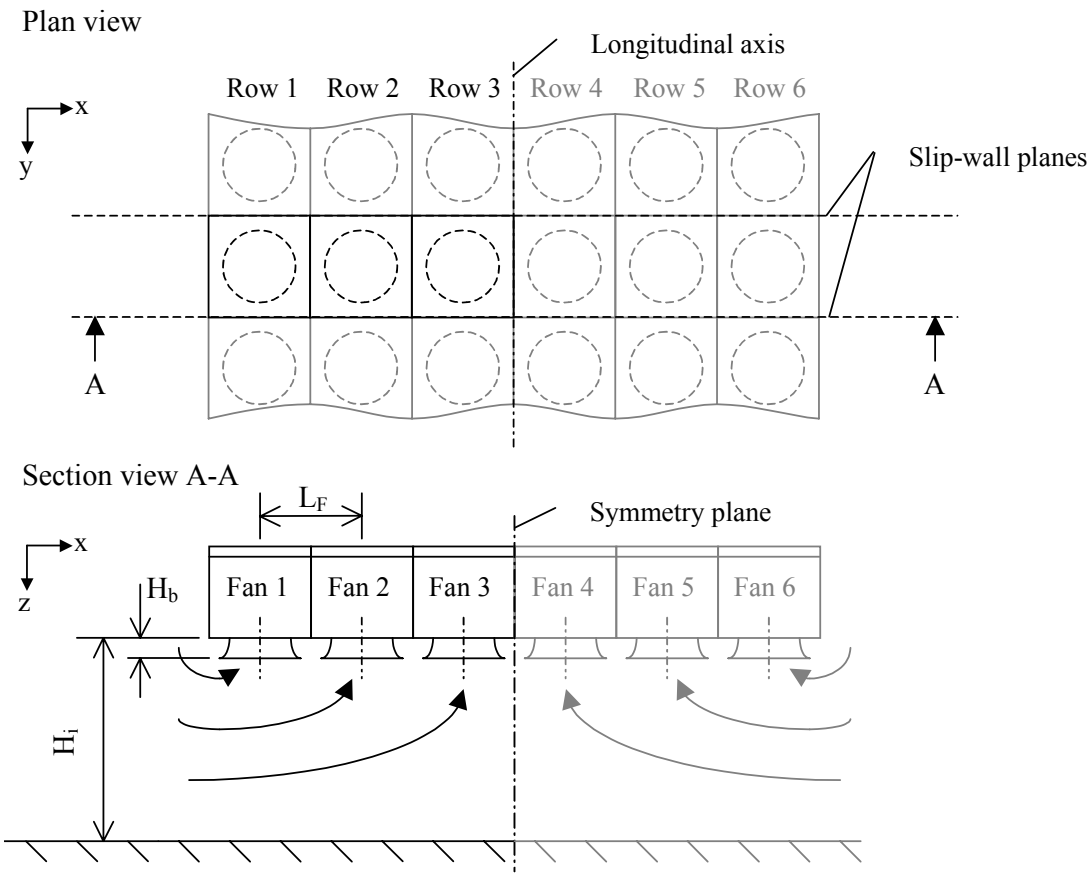

Figure 5.1. A section of a long ACSC bank located near its centre

Due to the proximity of the ground, an unfavourable cross-flow velocity component is induced underneath the fan platform. Depending on the height of the fan platform, H_i, the induced cross-draft may result in flow separation and distortion at the fan inlets.

In this section, these system effects are investigated by modelling the section of the ACSC at various platform heights.

5.1.1. Computational aspects

Assuming the flow to be *essentially two-dimensional* (i.e., no flow occurring across the sectional planes) these planes were accordingly modelled as slip-walls. Owing to the symmetry plane through the longitudinal axis, it was only required to model one half of the section under consideration, as shown in Figure 5.1.

According to Kröger (2004) the reduction of effectiveness due to recirculation under windless conditions for this type of ACSC, is less that 1%. For the purpose of this investigation, the modelling of heat transfer to the air and the buoyant plume were therefore not essential. By not modelling the discharge flow, the computational grid could consequently be simplified and reduced in size, resulting in shorter computing times.

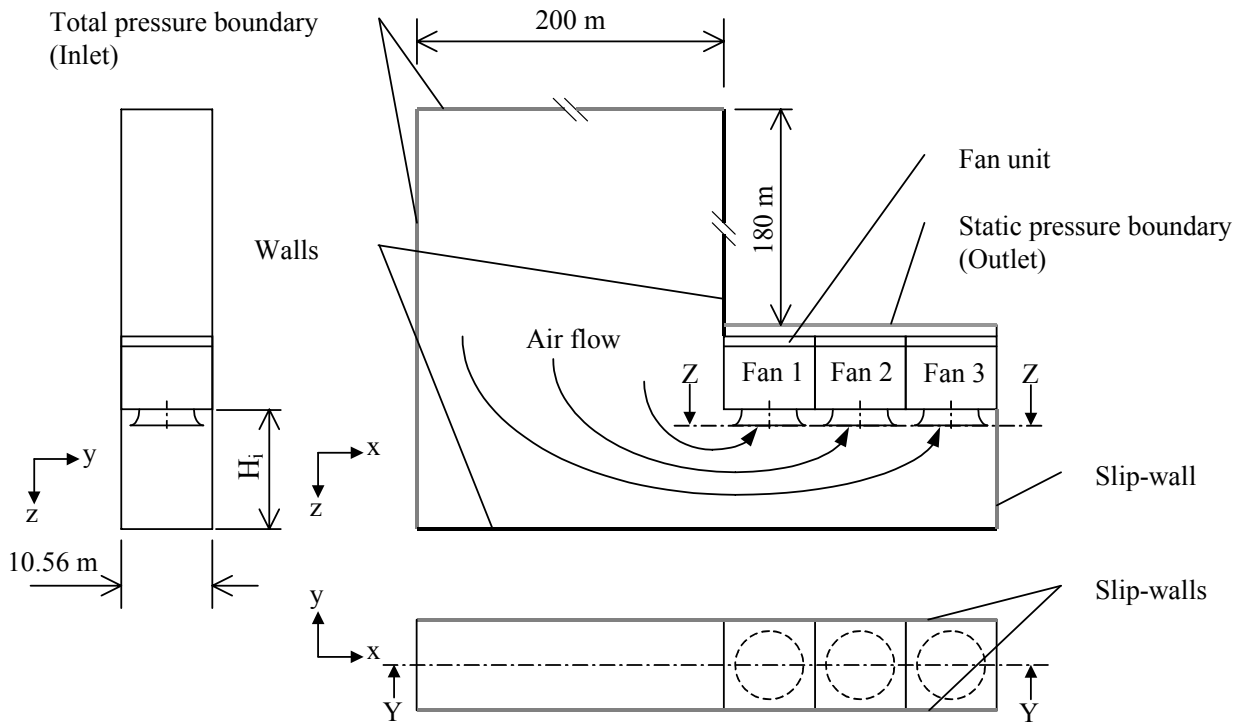

Figure 5.2. Layout of computational grid for modelling a section of the ACSC under windless conditions at various platform heights

The computational grid (consisting of between 45,000 and 500,000 cells depending on the platform height) is shown in Figure 5.3 and Figure 5.4.

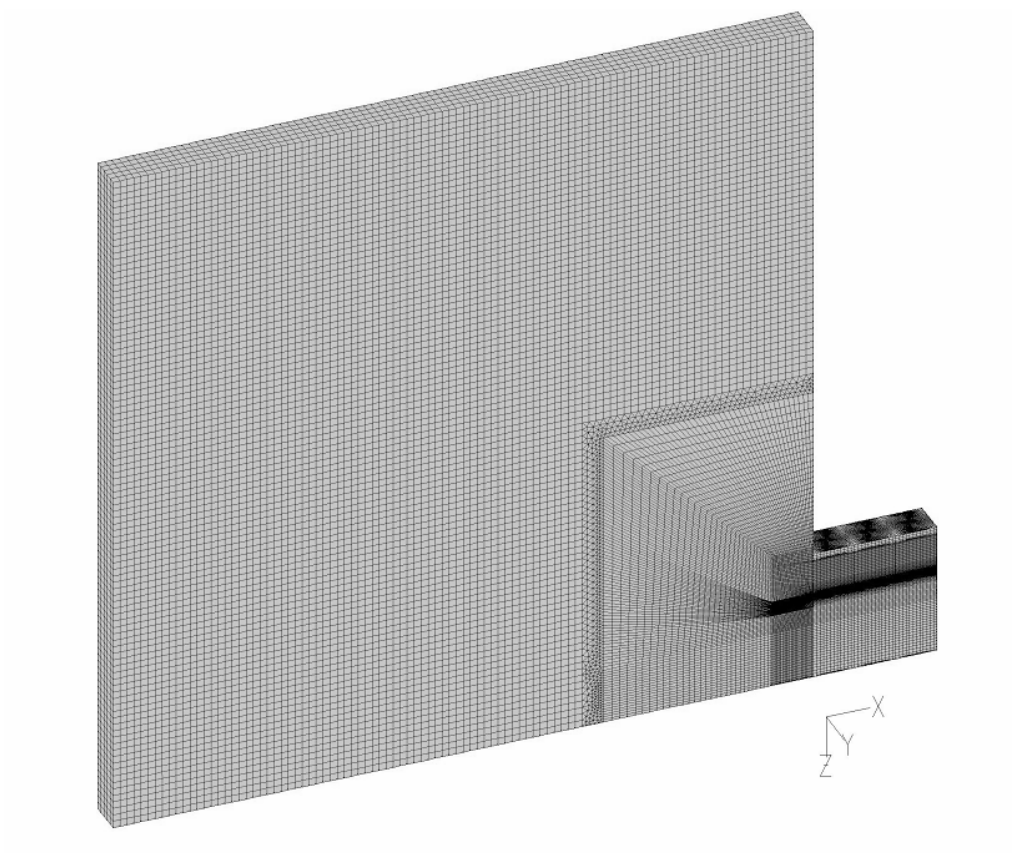

Figure 5.3. Computational grid for modelling a section of the ACSC under windless conditions

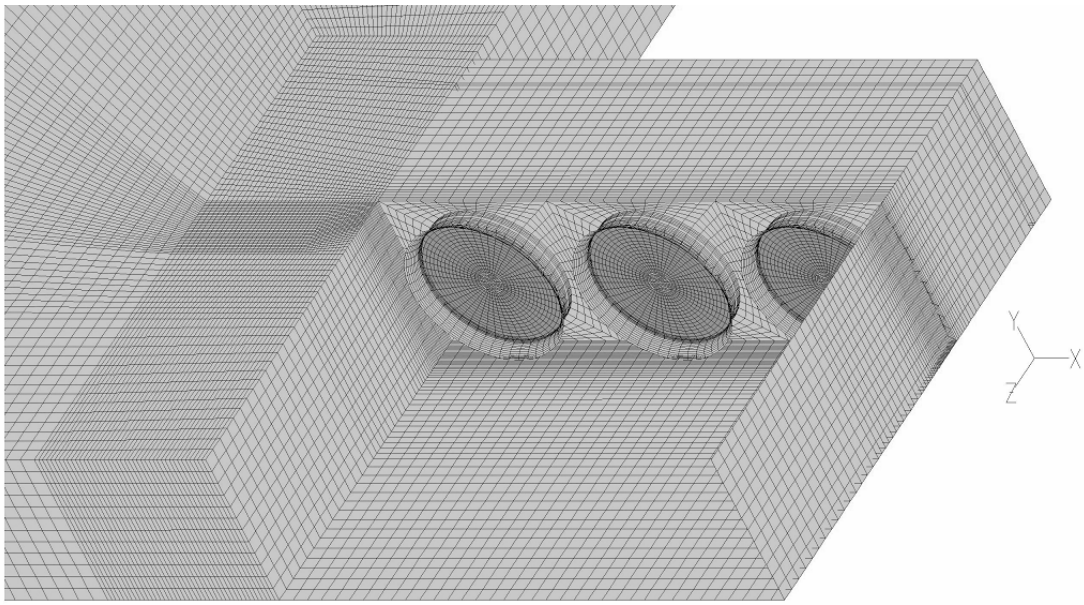

Figure 5.4. Enlarged sectional view of the computational grid near the fan units

The atmospheric inlet boundary was modelled with a total pressure boundary condition, with p_{tot}=0. With no recirculation or outflow occurring, the boundary condition presented no significant problem with regards to numerical stability. The outlet boundary, located 2 m above the fan units, was modelled as a static pressure boundary condition, with p=0. The ground, plenum walls, fan inlet, and fan hub were modelled as zero-slip walls. Four different platform heights (H_i=26 m, 22 m, 18 m, and 14 m) were considered. The dimensions of a fan unit are given in figure 4.17. The thermo-physical properties of the air at the prescribed ambient conditions are given in Appendix A.

Due to the complexity of the flow (e.g., flow separation at fan inlets, the addition of body forces in the actuator disc model) first order upwind discritization was employed in the momentum and turbulence equations in order to maintain numerical stability. Overall convergence of a simulation was established when the mass flow rate through all three fan units converged to the fifth significant digit (typically obtained after 800 iterations).

In order to compare the performance of fans operating under distorted inlet conditions to the ideal case with no inlet flow distortions, the following parameters were defined:

The volumetric effectiveness of a fan, $e_{V(i)}$, defined by equation 5.1, is the ratio of the numerically determined flow rate through a particular fan unit in a multi-fan system simulation ,V_a, to the reference flow rate of the same freestanding fan unit,V_{ar}

$$e_{V(i)} = \frac{V_{a(i)}}{V_{ar}} \tag{5.1}$$

where i is an index corresponding to the appropriate fan number (i=1, 2, or 3). The system volumetric effectiveness, $e_{V(sys)}$, of a multi-fan system is similarly defined by equation 5.2.

$$e_{V(sys)} = \frac{\sum_{i=1}^{n_F} V_{a(i)}}{n_F V_{ar}} \tag{5.2}$$

where n_F is the number of fan rows. In subsequent sections, these parameters are used to quantify the effect of inlet flow distortions on fan performance.

The reference flow rates for a freestanding fan unit corresponding to the A-fan (d_F=9.145 m, γ_{pt}=16º) and the B-fan (d_F=9.145 m, γ_{cr}=34.5º) are determined in Section 4.1.2 as 653.88 m^3/s and 659.49 m^3/s, respectively. Numerical fan performance results of subsequent sections are given in Appendix E.

5.1.2. Effect of platform height

The effect of platform height on the performance of the A-fan (d_F=9.145 m, γ_{pt}=16º) is investigated by modelling a section of the ACSC at various platform heights (H_i= 26 m, 22 m, 18 m, and 14 m). The streamline plots for the extreme cases of H_i=26 m and H_i=14 m are shown in Figure 5.5 and Figure 5.6.

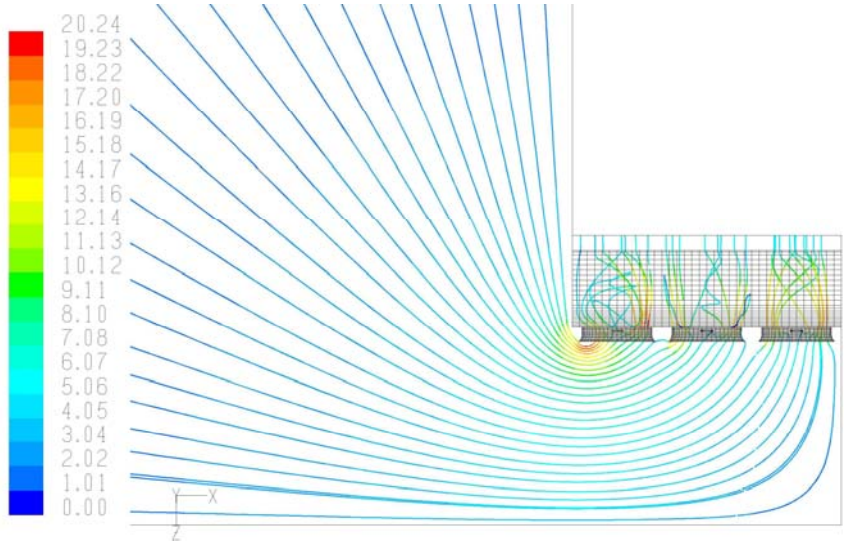

Figure 5.5. Streamline plot for H_i=26 m

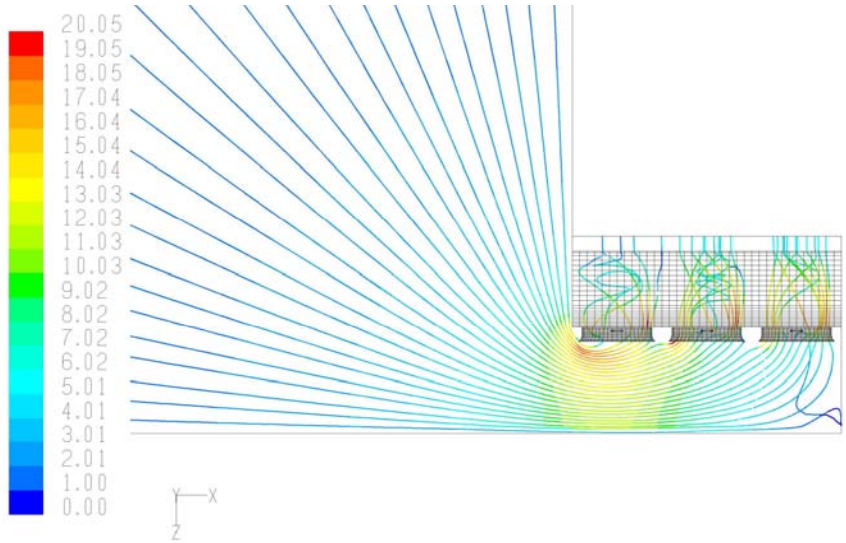

Figure 5.6. Streamline plot for H_i=14 m

Static pressure contours on plane Y-Y (refer to Figure 5.2), for H_i=26 m and H_i=14 m are shown in Figure 5.7 and Figure 5.8, respectively.

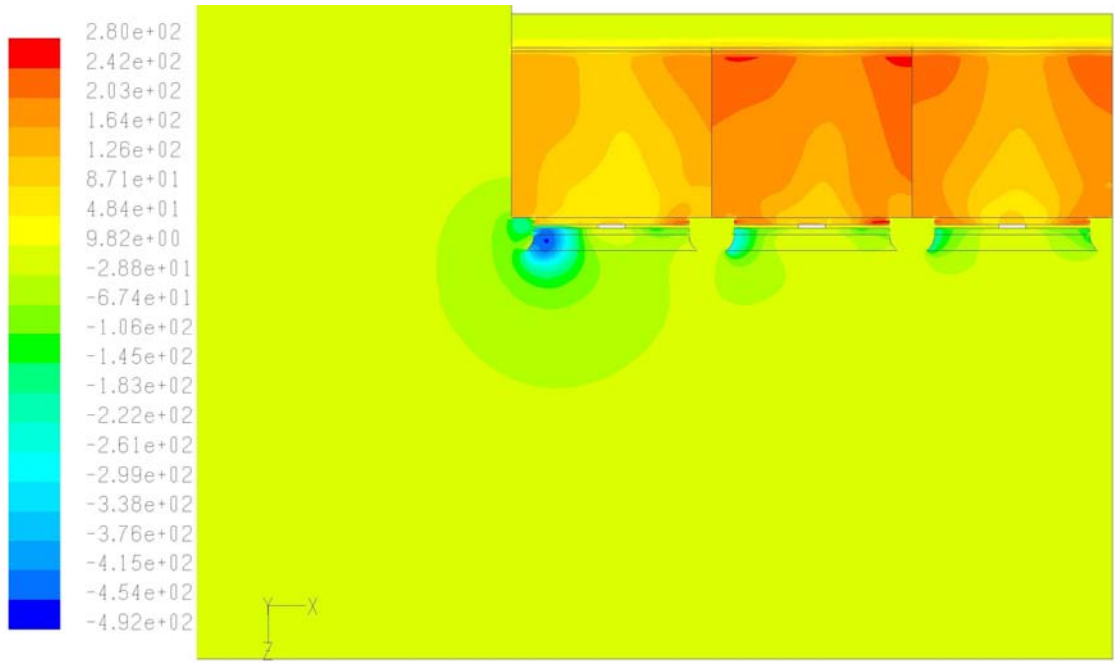

Figure 5.7. Static pressure (Pa) plot for H_i=26 m (plane Y-Y)

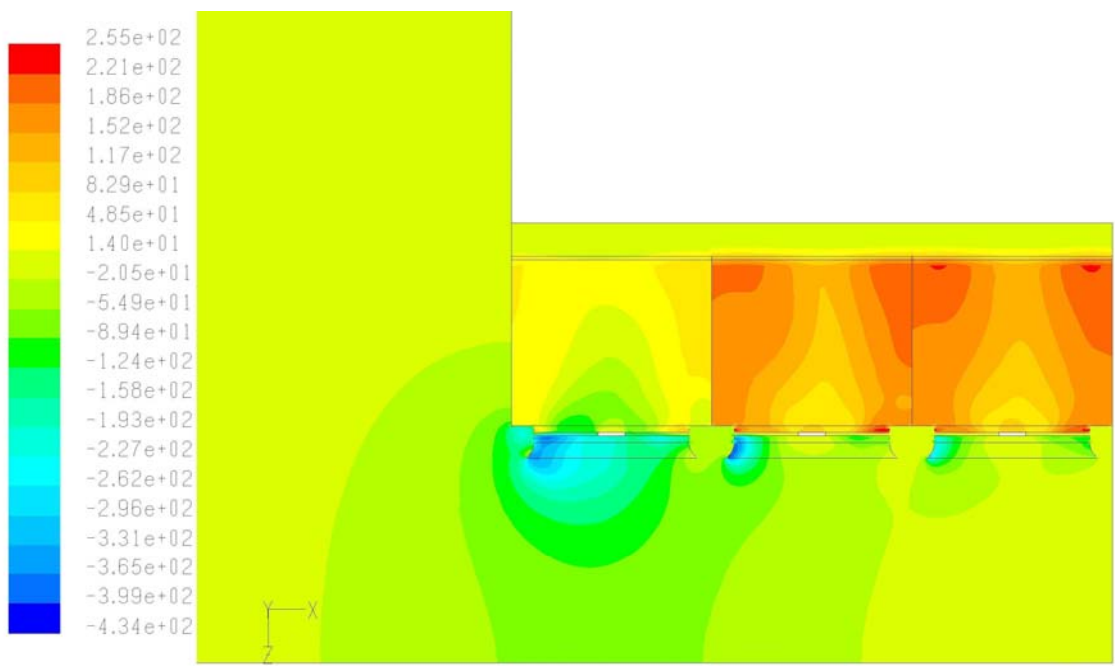

Figure 5.8. Static pressure (Pa) plot for H_i=14 m (plane Y-Y)

The corresponding vector plots of the flow through the edge fan are shown, respectively, in Figure 5.9 and Figure 5.10.

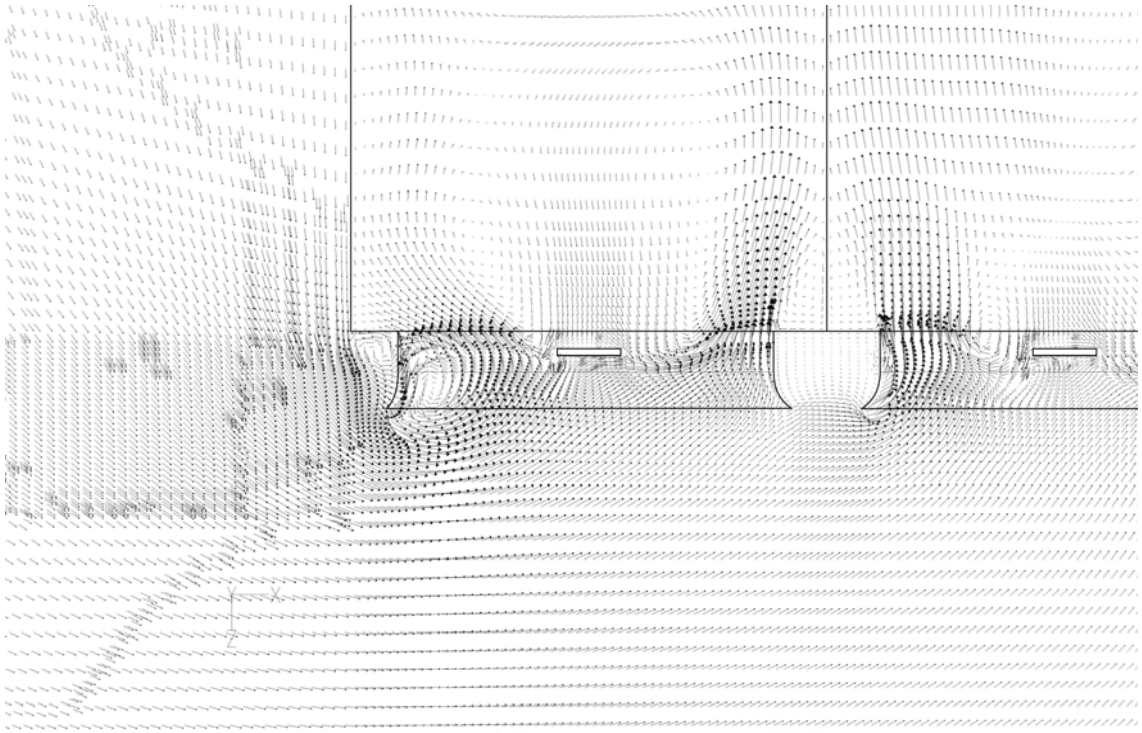

Figure 5.9. Vector plot for H_i=26 m (plane Y-Y)

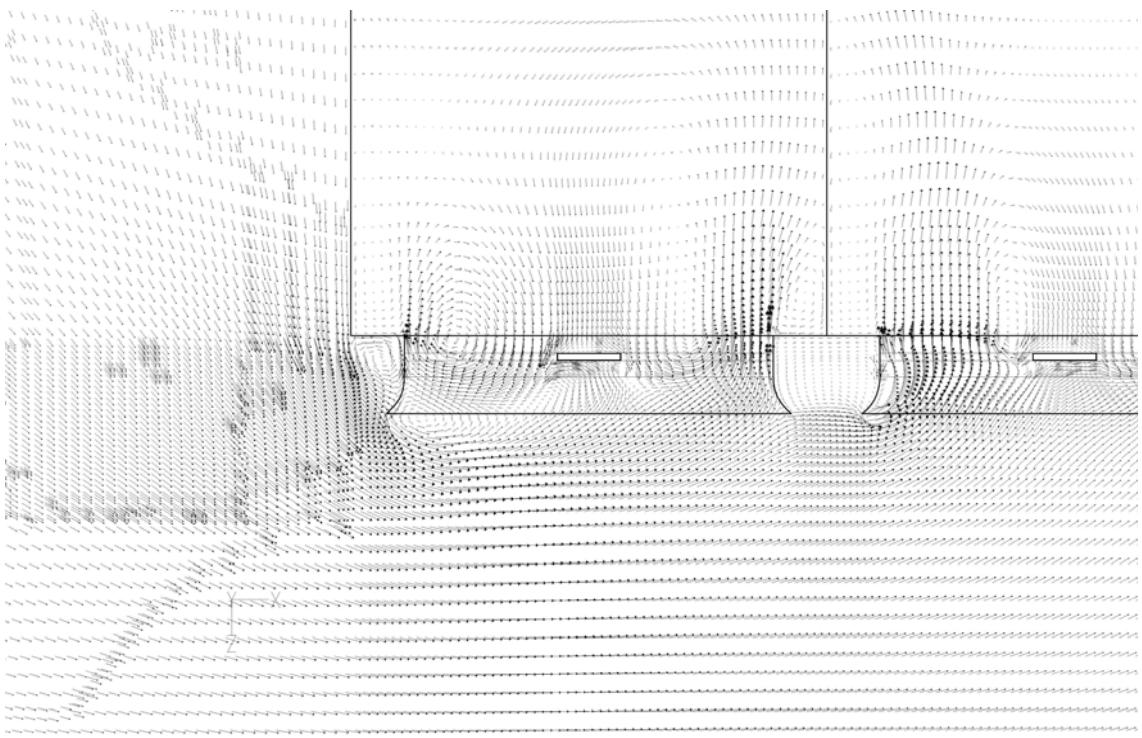

Figure 5.10. Vector plot for H_i=14 m (plane Y-Y)

Static pressure contours on plane Z-Z (refer to Figure 5.2) at the inlet of the edge fan, for H_i=26 m and H_i=14 m are shown in Figure 5.11 and Figure 5.12, respectively.

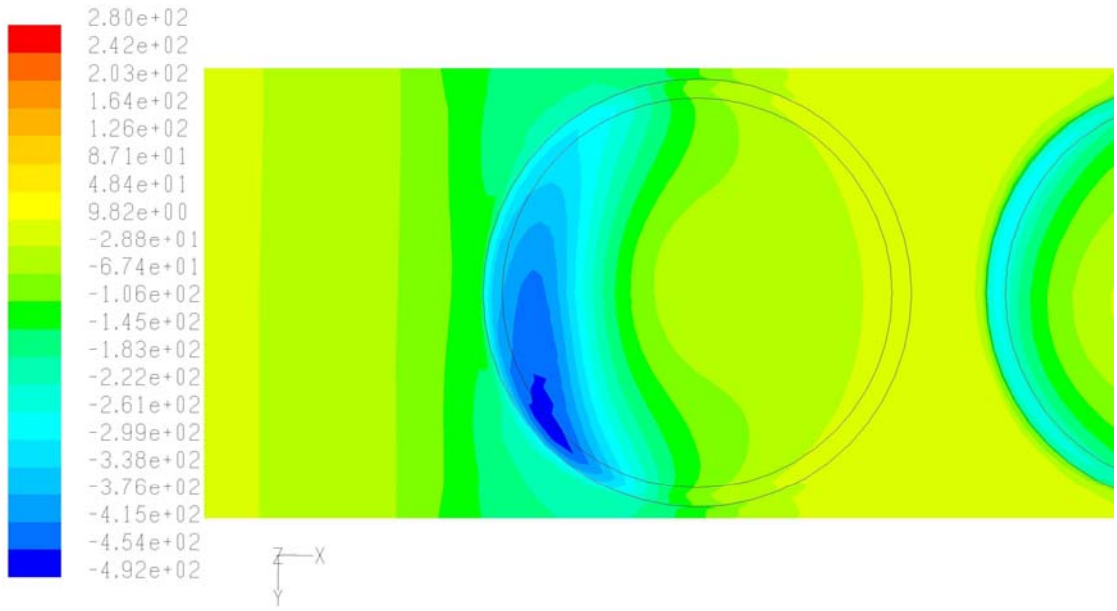

Figure 5.11. Static pressure (Pa) plot for H_i=26 m (plane Z-Z)

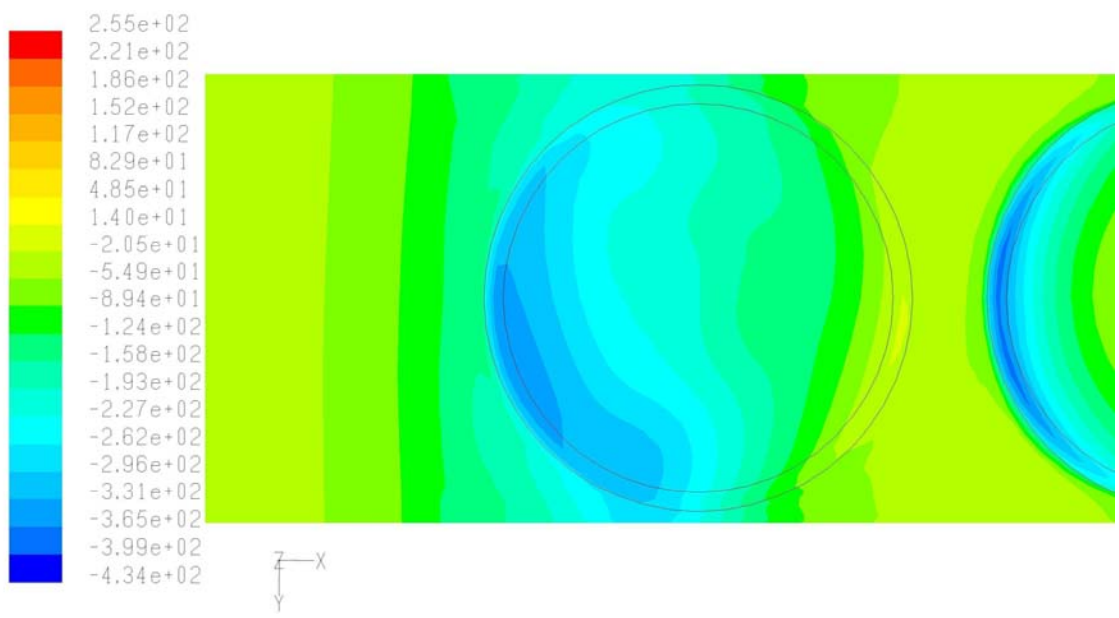

Figure 5.12. Static pressure (Pa) plot for H_i=14 m (plane Z-Z)

The corresponding vector plots on plane Z-Z are shown, respectively, in Figure 5.13 and Figure 5.14.

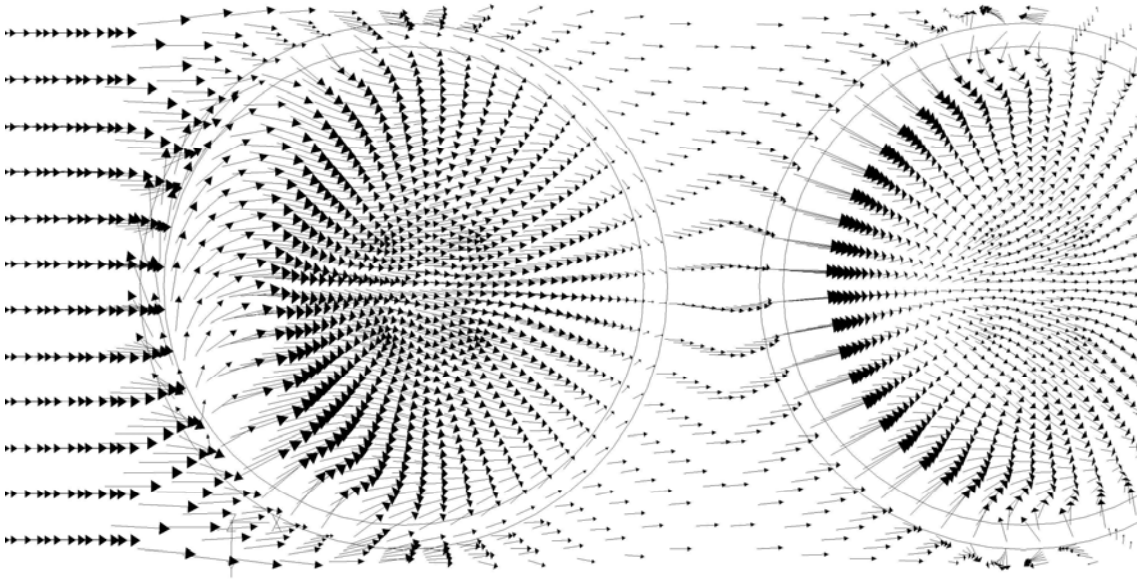

Figure 5.13. Vector plot for Hi=26 m (plane Z-Z)

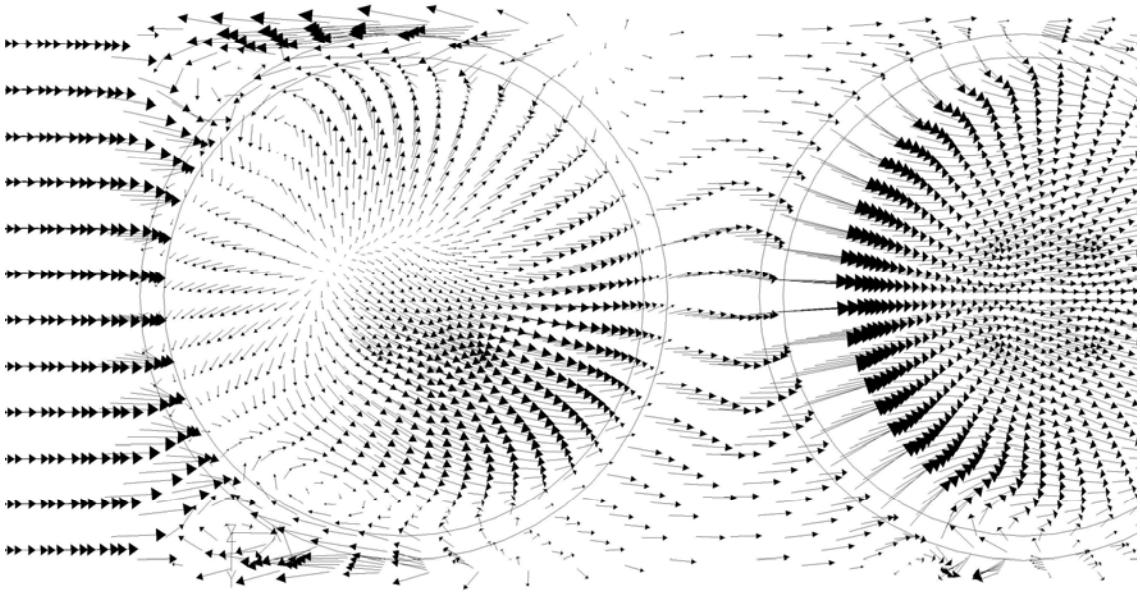

Figure 5.14. Vector plot for H_i=14 m (plane Z-Z)

In figures 5.7 to 5.14, the flow separation or distortion occurring at the inlet of the edge fan is evident. The adverse effect of these flow distortions on fan performance is shown in Figure 5.15.

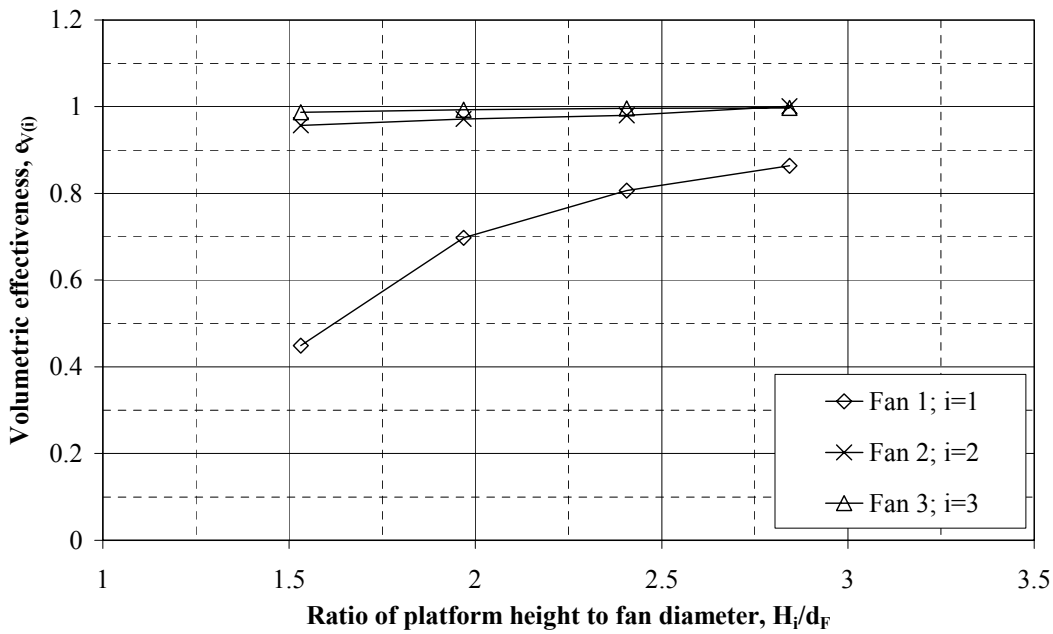

Figure 5.15. Volumetric effectiveness of the fans in a section of an ACSC at various platform heights

Salta and Kröger (1995) present the following empirical relation to describe the reduction in system volumetric effectiveness, $e_{V(sys)}$, with a decrease in platform height, H_i, for an ACHE or ACC with n_F fan rows

$$e_{V((sys)} = 0.985 - \exp^{(-X)} \tag{5.3}$$

where

$$X = \frac{(1 + 45/n_F)H_i}{(6.35d_F)} \tag{5.4}$$

This correlation is applicable for $n_F>1$, $H_b/d_F=0.19$, $L_F/d_F=1.27$, and $d_h/d_F=0.26$. For the ACSC under consideration, $n_F=6$, $H_b/d_F=0.21$, $L_F/d_F=1.29$, and $d_h/d_F=0.153$. Although the geometry of the numerical model differs slightly from the experimental apparatus used by Salta and Kröger (1995), the numerically determined system volumetric effectiveness shows a similar trend to that predicted by equation 5.3, as shown in Figure 5.12.

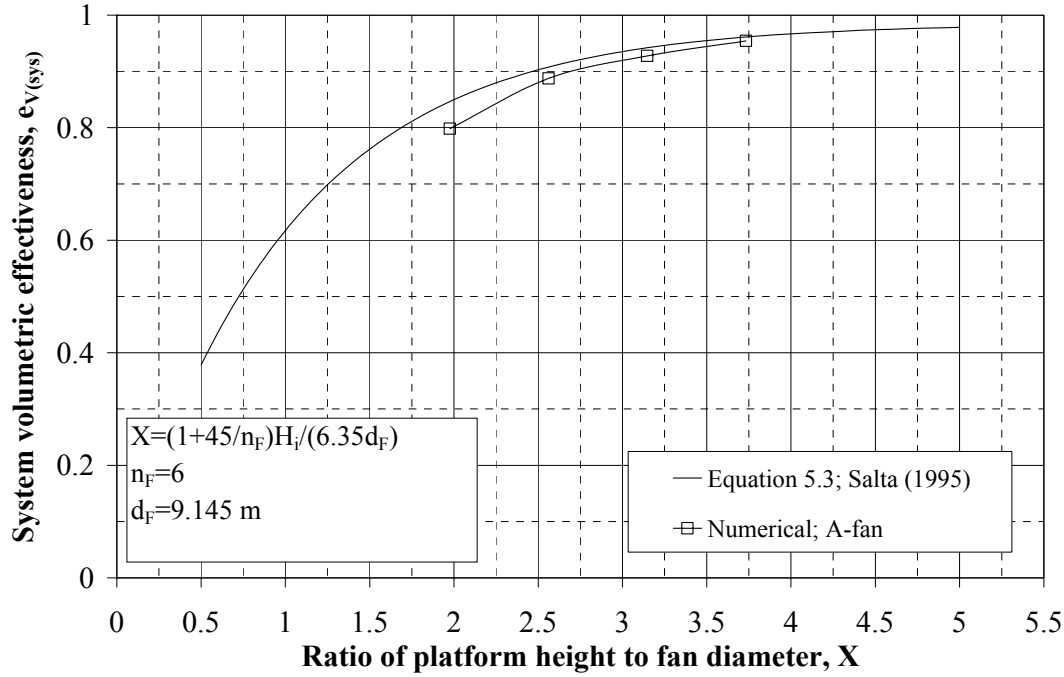

Figure 5.16. System volumetric effectiveness of an ACSC at various platform heights

5.1.3. Comparison of A-fan and B-fan (Effect of hub-tip ratio)

The numerically predicted performance of the B-fan (d_F=9.145 m, γ_{cr}=34.5º) in the section of the ACSC at different platform heights is considered. The pressure and vector plots of the edge fan for the worst case of H_i=14 m are shown in Figure 5.17 and Figure 5.18, respectively.

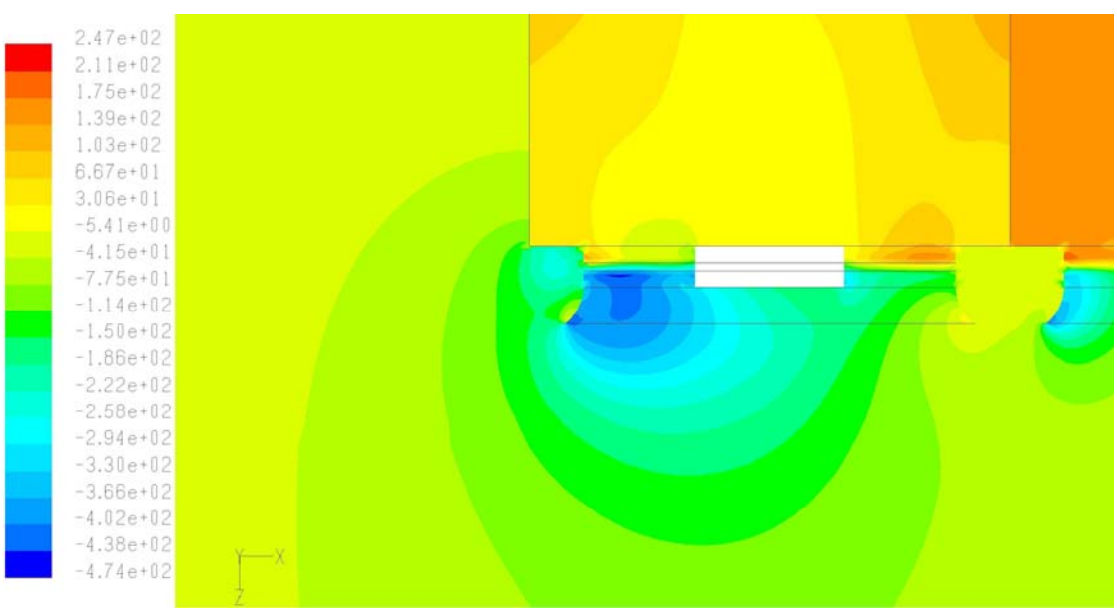

Figure 5.17. Static pressure (Pa) plot of edge fan employing the B-fan with H_i=14 m

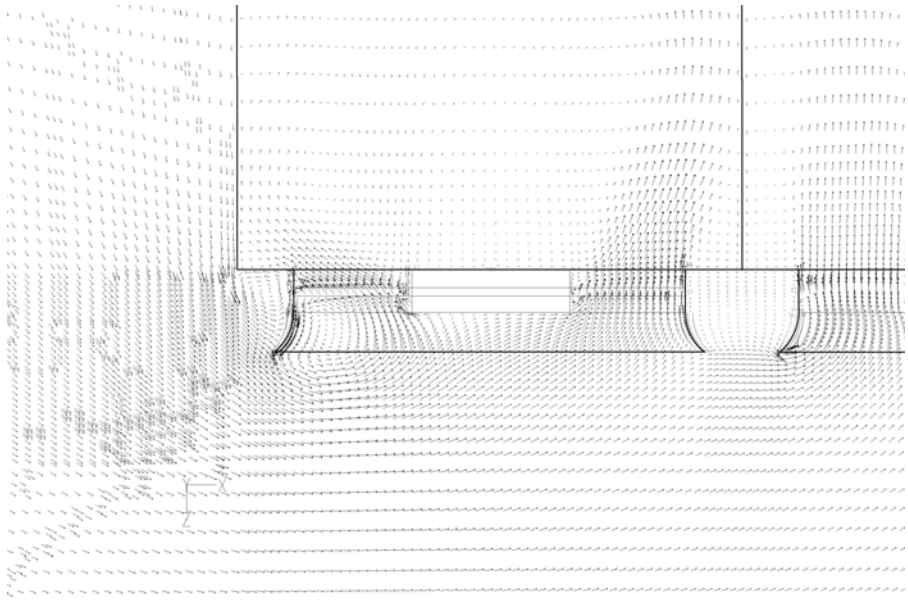

Figure 5.18. Vector plot of edge fan employing the B-fan with H_i=14 m

Figure 5.19 depicts the variation of volumetric effectiveness of the edge fan with platform height for both the A-fan and B-fan.

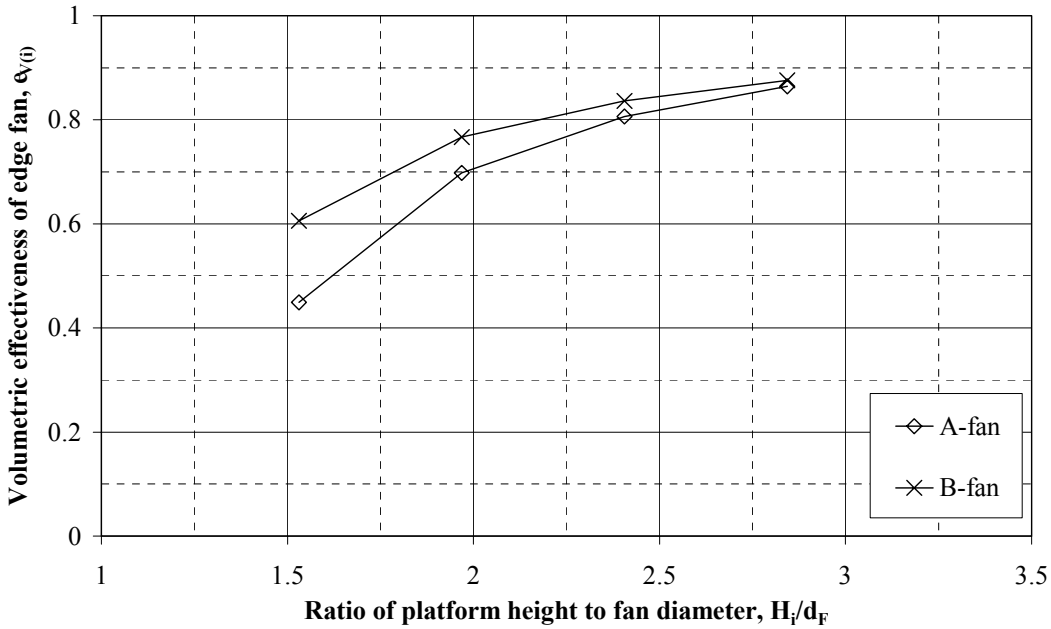

Figure 5.19. Volumetric effectiveness of the edge fan (for the A-fan and B-fan) in the section of the ACSC at various platform heights

The corresponding system volumetric effectiveness for the A-fan and B-fan is shown in Figure 5.20.

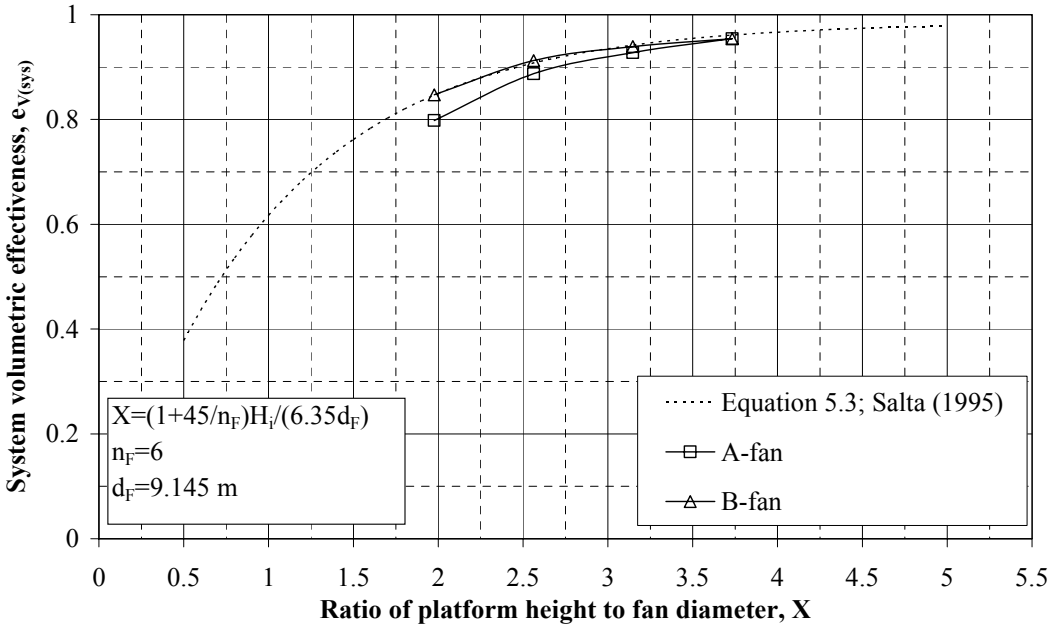

Figure 5.20. System volumetric effectiveness for the A-fan and B-fan

5.1.4. Effect of walkways and windscreens

Based on experimental tests, Salta and Kröger (1995) have shown that the volumetric effectiveness of an ACHE (or ACC) can be improved by adding a solid walkway around the fan platform. In this section the effect of such a walkway on fan performance is numerically investigated. The effect of additional shade net windscreens are also modelled. Four different configurations, or test cases, schematically shown in Figure 5.21, are considered.

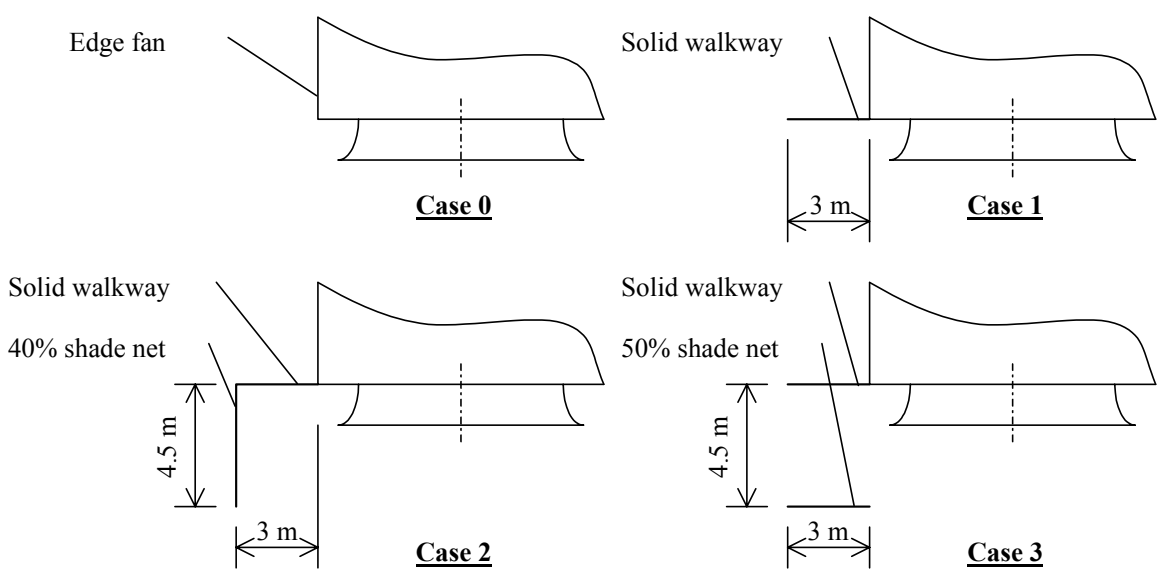

Figure 5.21. Four different walkway and windscreen configurations investigated

The shade net screens were numerically modelled in FLUENT using the *porous jump* boundary condition. This condition calculates a pressure drop across a face in the flow domain, based on the normal velocity and a prescribed loss coefficient, i.e., $\Delta p = K0.5\rho v^2$. The loss coefficients for normal flow through the 40% and 50% shade net were experimentally determined by von Gossler (2004) and found to have values of 0.5737 and 1.13, respectively. Furthermore the solid walkway was modelled as a zero-slip wall.

It was found that the solid walkway resulted in a significant increase in volumetric effectiveness, mainly due to improved inlet conditions of the edge fan. This is illustrated in the static pressure and vector plots, shown in Figure 5.22 and Figure 5.23, respectively, for case 1 employing the A-fan at a platform height of H_i=14 m.

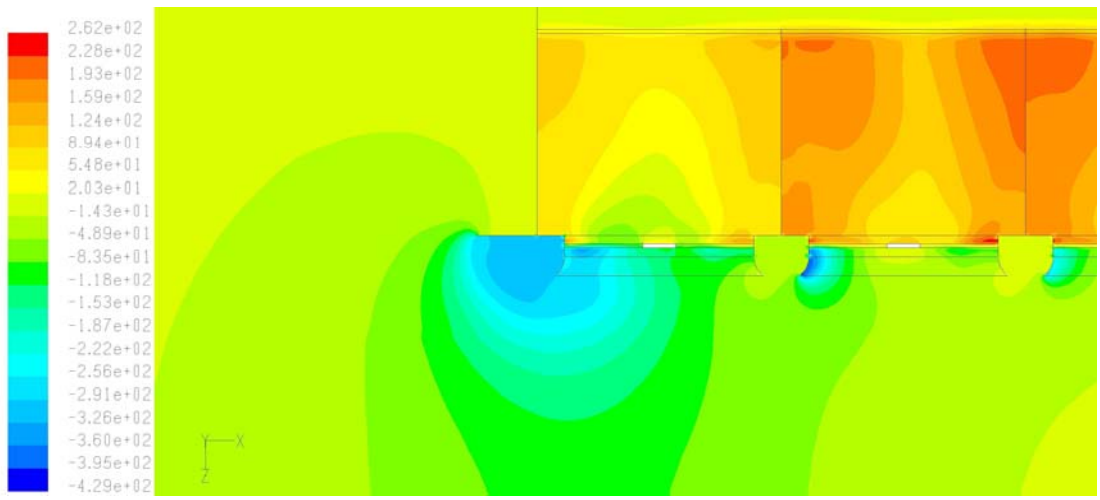

Figure 5.22. Static pressure (Pa) plot for case 1 employing the A-fan with H_i=14 m

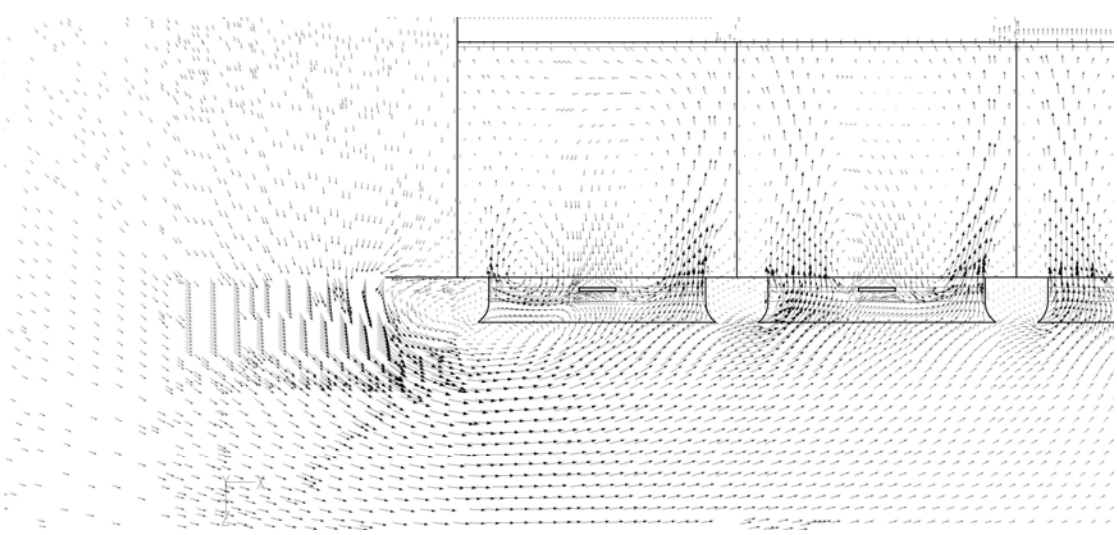

Figure 5.23. Vector plot for case 1 employing the A-fan with H_i=14 m

The volumetric effectiveness of the edge fan for cases 0 to 4 at various platform heights, employing the A-fan and B-fan, are shown, respectively, in Figure 5.24 and Figure 5.25.

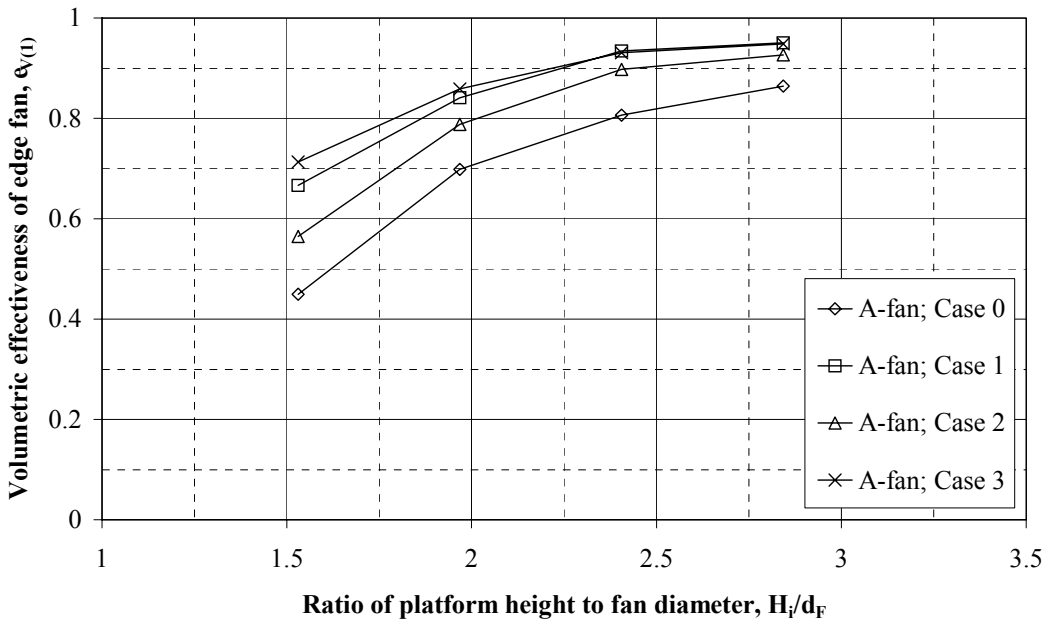

Figure 5.24. Volumetric effectiveness of the edge fan (A-fan) for cases 0 to 3

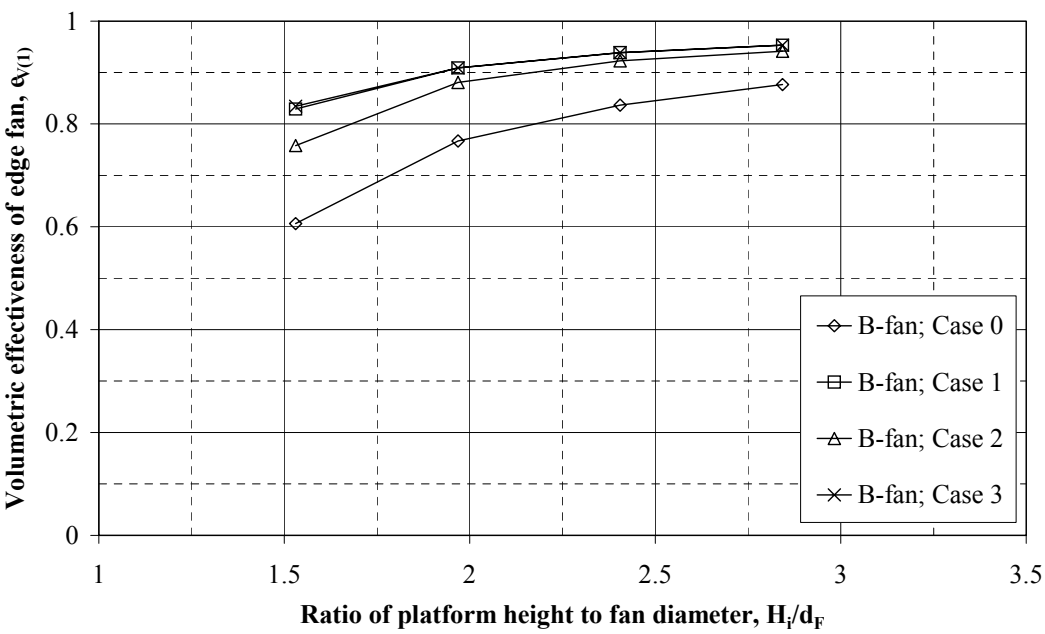

Figure 5.25. Volumetric effectiveness of the edge fan (B-fan) for cases 0 to 3

The system volumetric effectiveness for cases 0 to 4 at various platform heights, employing the A-fan and B-fan, are respectively shown in Figure 5.26 and Figure 5.27.

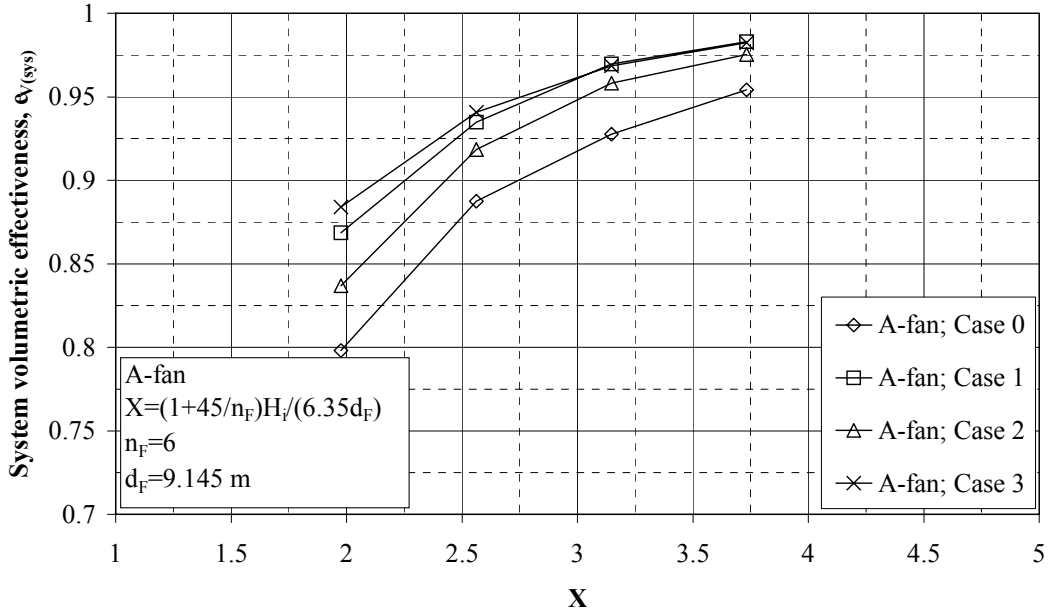

Figure 5.26. System volumetric effectiveness for cases 0 to 3 employing the A-fan

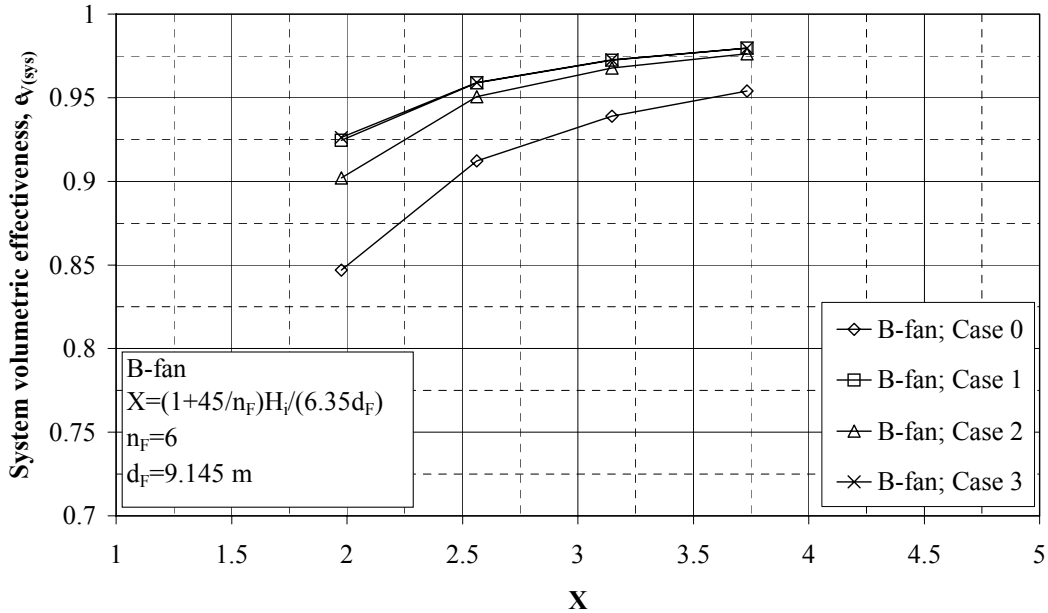

Figure 5.27. System volumetric effectiveness for cases 0 to 3 employing the B-fan

Numerical results showed that the vertical 40% shade net screen in case 2 had a choking effect on the flow. The horizontal 50% shade net in case 3 marginally improved the performance of the A-fan, whilst having no effect on the B-fan.

5.2. Crosswind Conditions

The modelling of the effect of crosswind (i.e., wind normal to the longitudinal axis of the fan platform) on the section of the ACSC using an *essentially two-dimensional* modelling approach is considered. The objective of this part of the study is to assess whether or not this modelling approach results in a realistic representation of the air flow through the section of the ACSC located near the centre.

5.2.1. Computational aspects

The applied boundary conditions and the layout of the computational grid are shown in Figure 5.28.

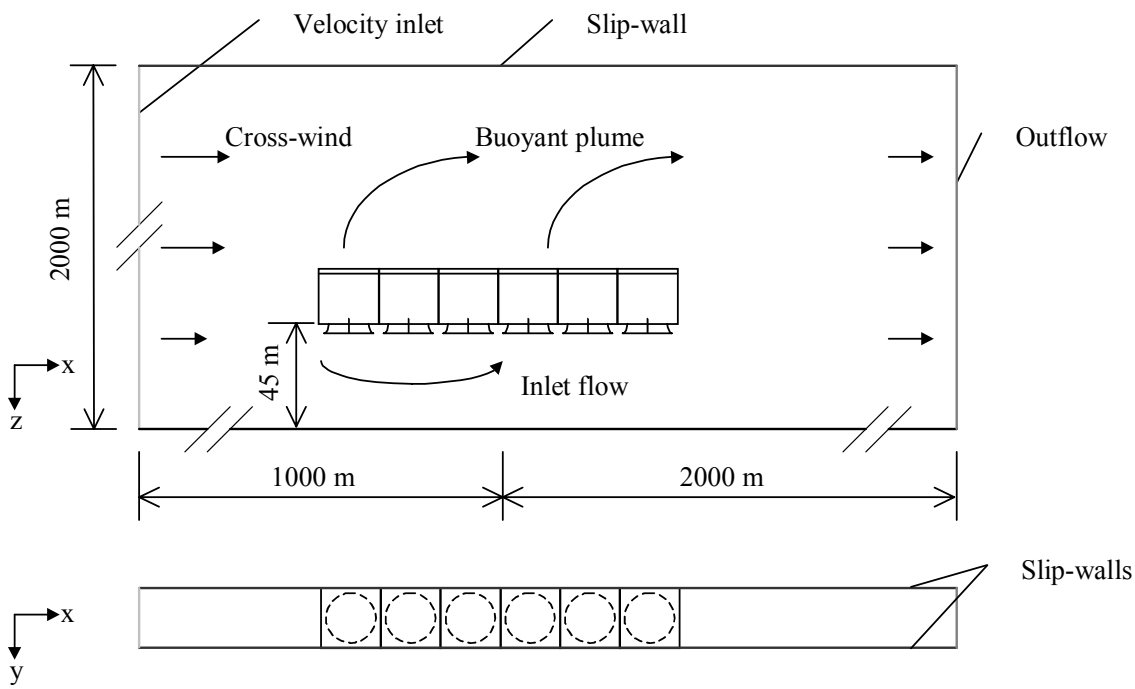

Figure 5.28. Layout of computational grid for modelling the section of an ACSC under crosswind conditions (essentially two-dimensional modelling approach)

Air entering the flow domain through the velocity inlet boundary is confined to a channel-type flow by the top, side, and bottom slip-wall boundaries. The flow exits the domain through the outflow boundary, which is placed far enough downstream so as to avoid inflow across it.

The inlet profiles for the wind velocity (v_w), turbulent kinetic energy (k), and rate of dissipation (ε) as a function of vertical distance above the ground (h), as per Richards and Hoxey (1993) are given, respectively, by equations 5.3, 5.4, and 5.5

$$v_w = \frac{u_*}{\kappa} \ln\left(\frac{h + z_0}{z_0}\right) \tag{5.3}$$

$$k = \frac{u_*^2}{\sqrt{C_\mu}} \tag{5.4}$$

$$\varepsilon = \frac{u_*^2}{\kappa(h + z_0)} \tag{5.5}$$

where the friction velocity u_* is defined as

$$u_* = \frac{\kappa v_r}{\ln\left(\frac{h_r + z_0}{z_0}\right)} \tag{5.6}$$

The constants appearing in equations 5.3 to 5.6 are defined in Table 5.1.

Table 5.1. Constants in equations 5.3 to 5.6

Von Karman constant	κ=0.41
Surface roughness length*	z_0=0.05 m
Constant in k-ε turbulence model	C_μ=0.09
Reference height	h_r=45 m
Wind velocity at reference height	v_r=3 m/s

*According to Eurocode 1 (1991) for terrain category II (i.e., farmlands with occasional small farm structures, houses, or trees)

Buoyancy effects on the plume were taken into account by means of the Boussinesq model, whereby the buoyancy body force in the momentum equation is approximated by

$$F_z = (\rho - \rho_a)g \approx -\rho_a \beta_T (T - T_a) g \tag{5.7}$$

where β_T is the thermal expansion coefficient, which is 1/T for an ideal gas, and g is the gravitational acceleration acting in the positive z-direction.
The computational grid, consisting of 810,000 cells, is shown in Figure 5.29 and Figure 5.30.

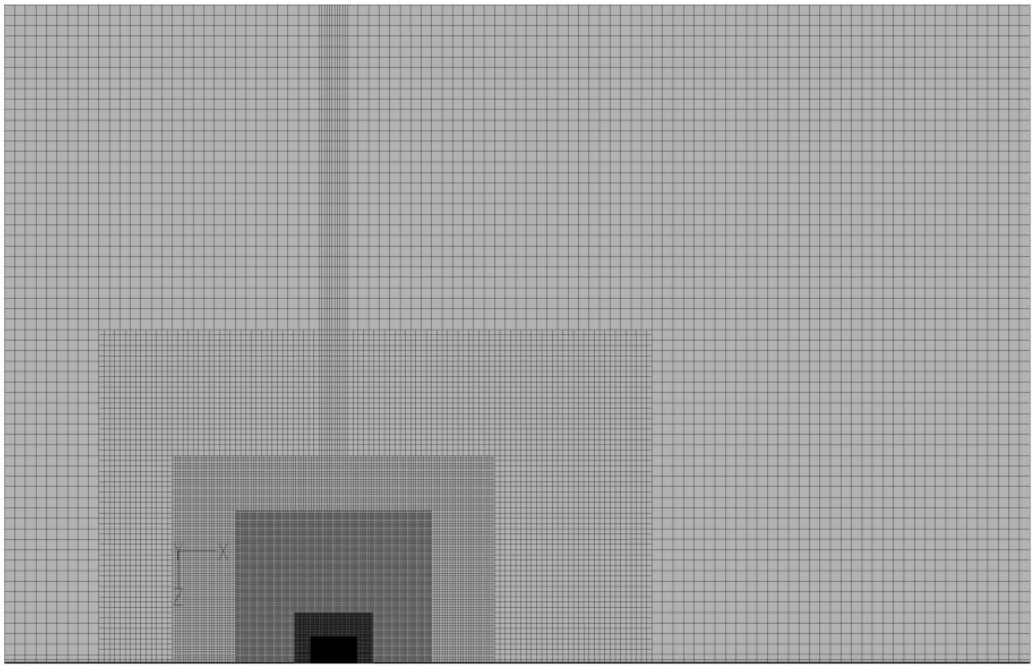

Figure 5.29. Computational grid for modelling the section of an ACSC under crosswind conditions

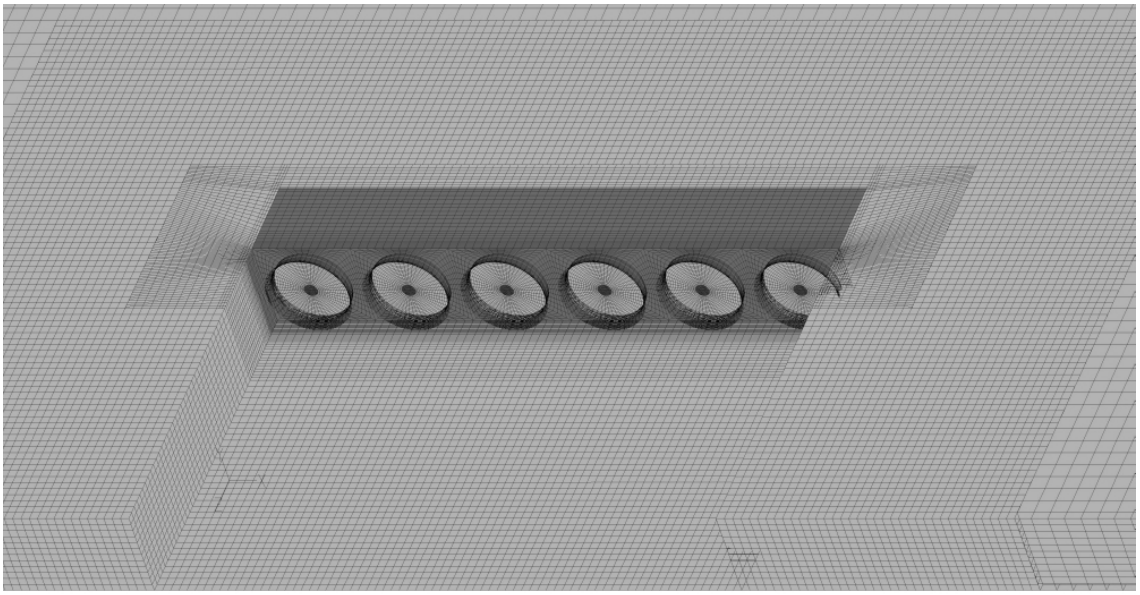

Figure 5.30. Enlarged section view of computational grid near the fan units

5.2.2. Discussion

Figure 5.31 and Figure 5.32 respectively show the streamline and temperature plots after 70 iterations.

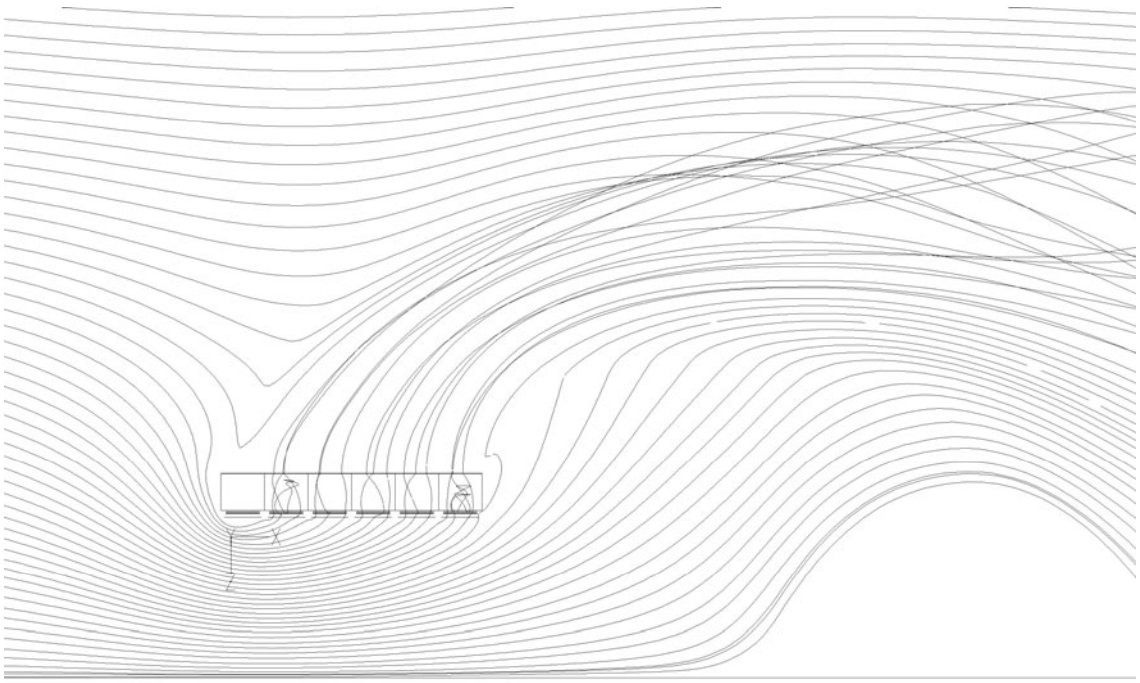

Figure 5.31. Streamline plot for a crosswind of 3 meters per second (m/s) after 70 iterations

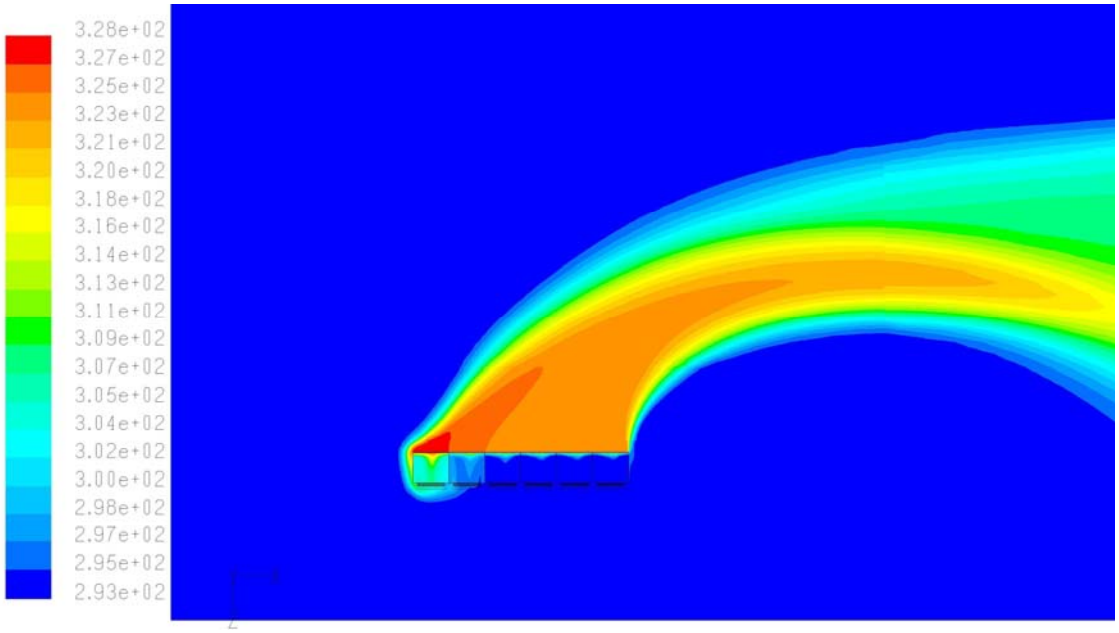

Figure 5.32. Temperature (K) plot for a crosswind of 3 m/s after 70 iterations

For this channel-type flow, the air is prevented from moving around the buoyant plume, resulting in the plume being forced horizontally by the oncoming flow, or wind. Because the oncoming air or wind cannot penetrate or move around the plume, a low-pressure pocket, or region, is formed underneath the plume, as shown in Figure 5.33. Consequently, unrealistically high velocities are induced underneath the fan platform as the air is drawn to the low-pressure region, as shown in Figure 5.34.

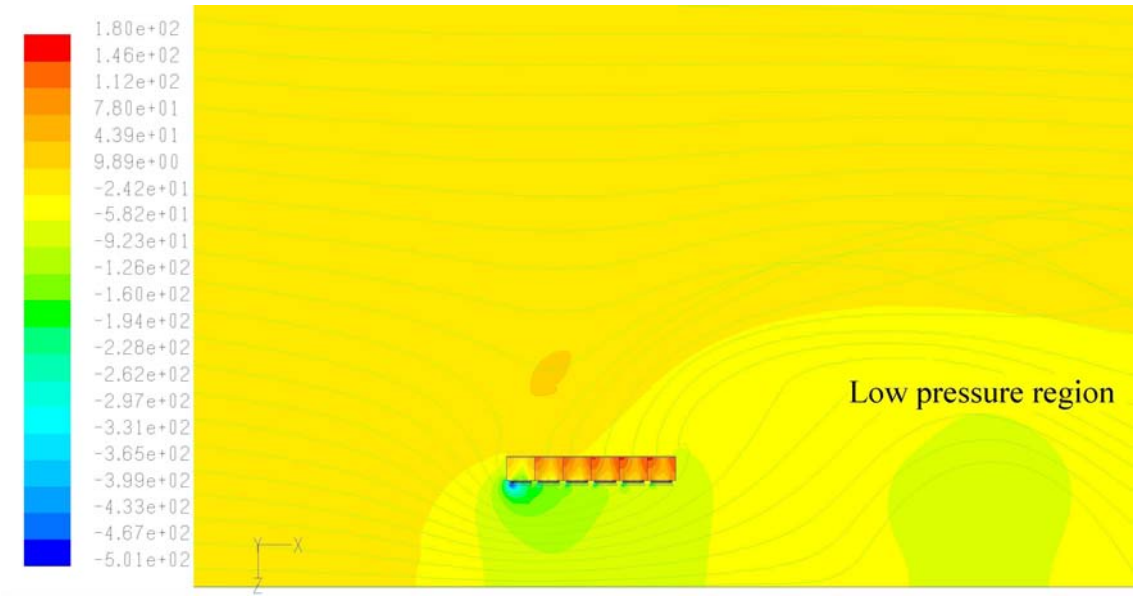

Figure 5.33. Static pressure (Pa) plot for a crosswind of 3 m/s after 70 iterations

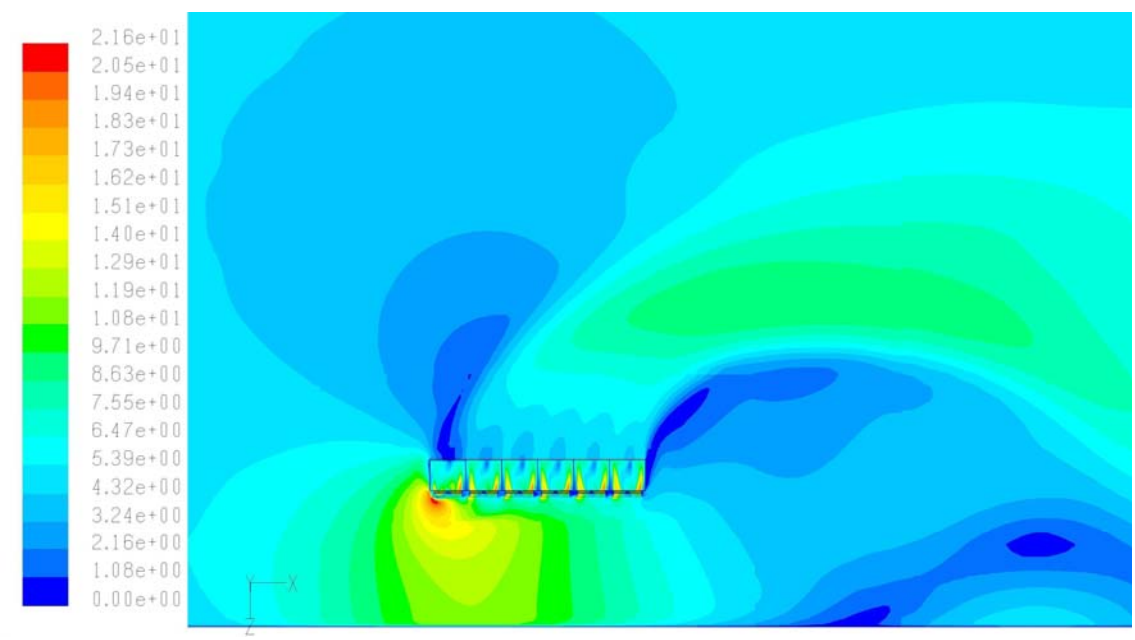

Figure 5.34. Velocity magnitude (m/s) plot for a crosswind of 3 m/s after 70 iterations

With further iterations, it was found that the average velocity underneath the fan platform increased to around 20 m/s, resulting in backflow through the first two fan units, as shown in the temperature plot in Figure 5.35.

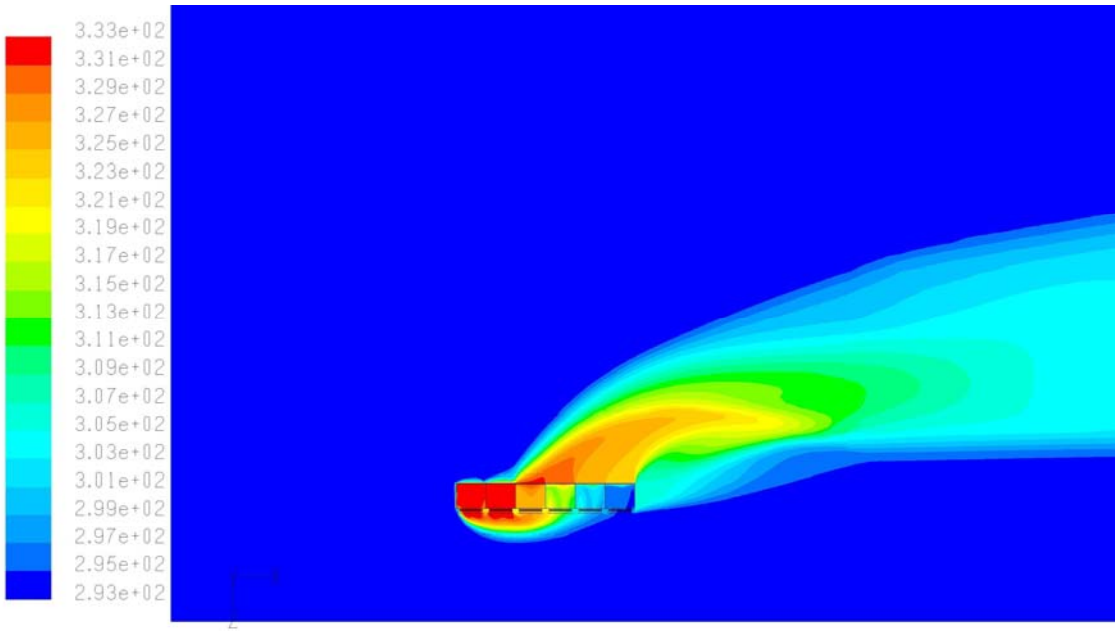

Figure 5.35. Temperature (K) plot for a crosswind of 3 m/s after 300 iterations

Van Staden (2000) numerically modelled the air flow through the ACSC of the Matimba power plant (refer to Figure 1.4 and Figure 1.5) using a *full three-dimensional* modelling approach. For this relatively long ACSC with a platform height of 45 m, van Staden (2000) reports a plume rise angle in the order of 40º to 50º for low crosswind speeds (≈3m/s). Van Aarde (1990), who conducted extensive experimental testing at Matimba under various wind conditions, does not report any backflow occurring. The nearly horizontal, or 90º, plume dispersion and backflow predicted by the *essentially two-dimensional* numerical model in the current investigation, is therefore considered to be unrealistic.

It can be deduced that the effective and realistic numerical simulation of the effect of wind on fan performance and plume dispersion associated with an ACSC, requires a *full three-dimensional* numerical model.

6. Conclusions and Recommendations

6.1. Importance of this Study

A forced draft air-cooled steam condenser (ACSC) in a direct-cooled power plant condenses steam in a closed power cycle. Axial flow fans in the ACSC move ambient air through an A-frame configuration of finned tube heat exchanger bundles in order to reject the latent heat of the condensing steam to the environment. The heat rejection capacity of an ACSC is proportional to the air mass flow rate and the temperature difference between the ambient air and the finned tubes. Therefore, owing to the dynamic interaction between the steam turbines and the ACSC, ambient conditions (e.g., dry bulb temperature, wind) and the flow rate delivered by the axial fans have a direct influence on the efficiency of such a direct air-cooled power plant. Consequently, the design and optimisation of an ACSC requires a fundamental understanding of the performance reducing effects on axial fans.

6.2. Research Findings

Inlet flow distortions caused by structures, wind and induced cross-drafts have an adverse effect on fan performance, due to a combination of increased inlet flow losses (i.e., flow separation at the inlet section), maldistribution of air into the fan (i.e., non-uniform inlet profiles), and off-axis inflow conditions. In this study the effect of inlet flow distortions on fan performance in a section (or sector) of an ACSC is numerically investigated using the commercial computational fluid dynamics (CFD) code, FLUENT. With reference to the objectives stated in Section 1.3, a discussion of the research results is given.

6.2.1. Numerical prediction of fan characteristics

Two axial flow fans referred to as the A-fan and the B-fan were considered. The A-fan is a commercially available fan commonly found in industrial cooling plants, whilst the B-fan is a prototype fan designed by Bruneau (1994) for application in an ACSC. The A-fan and the B-fan have the same diameter (d_F=9.145 m), number of blades (n_F=8), and rotational speed (N=125 rotations per minute, or rpm), but feature hub-tip ratios of d_h/d_F=0.153 and d_h/d_F=0.4, respectively.

An actuator disc model was used to numerically simulate and predict the performance of the axial fans. The model entails the calculation of momentum source terms based on blade element theory, thereby modelling the effect of an axial flow fan without actually modelling the fan blades as rotating solid surfaces in the flow domain. In order to validate the numerical fan model, the numerically predicted free inlet/free outlet fan characteristics were compared to data provided by the manufacturer in the case of the A-fan, and to experimental data measured by Stinnes (1998) in the case of the B-fan. Good consistency of the numerical predictions was found, as discussed in Section 4.3.

6.2.2. Effect of platform height on fan performance

An ACSC consisting of six long adjacent fan rows was considered. A section located near the centre of the platform was modelled under windless conditions assuming *essentially two-dimensional* flow.

At a platform height of H_i=26 m (H_i/d_F=2.84), the volumetric efficiency (i.e., ratio of volume flow rate under distorted inlet conditions, to volume flow rate under ideal inlet conditions with no flow distortion) for the edge fan was found to be 86.4% in the case of the A-fan, due to the effect of inlet flow distortions. It was found that lowering the platform height caused the flow separation and distortion at the inlet to become more severe, consequently reducing fan performance further. Volumetric effectiveness of the edge fan at the lowest platform height of H_i=14 m (H_i/d_F=1.53) for the case of the A-fan was predicted to be 44.9%, which corresponded to a system volumetric effectiveness of 79.8%. Numerical predictions displayed trends similar to the experimental results of Salta and Kröger (1995).

Although a platform height of H_i=14 m (H_i/d_F=1.53) is perhaps unrealistically low for practical ACSCs of this size, Duvenhage and Kröger (1996) state that, "The influence of wind on fan performance appears to exhibit features similar to the influence of platform height on fan performance." The reduction in fan performance under windless conditions at low platform heights (i.e., induced cross-draft conditions) may to a certain extent represent the effect of crosswinds on the performance of fans located on the windward edge of the fan platform. The relevance of this part of the study is therefore not only limited to the case of windless conditions.

6.2.3. Comparison of the A-fan and B-fan

Numerical simulation of the B-fan at different platform heights showed overall superior performance of this particular fan. Volumetric effectiveness of the edge fan ranged between 87.6% for H_i/d_F=2.84, and 60.6% for H_i/d_F=1.53. The fact that the B-fan is less affected by inlet flow disturbances can in part be explained by referring to the performance characteristics of the A-fan and the B-fan shown in Figure 6.1.

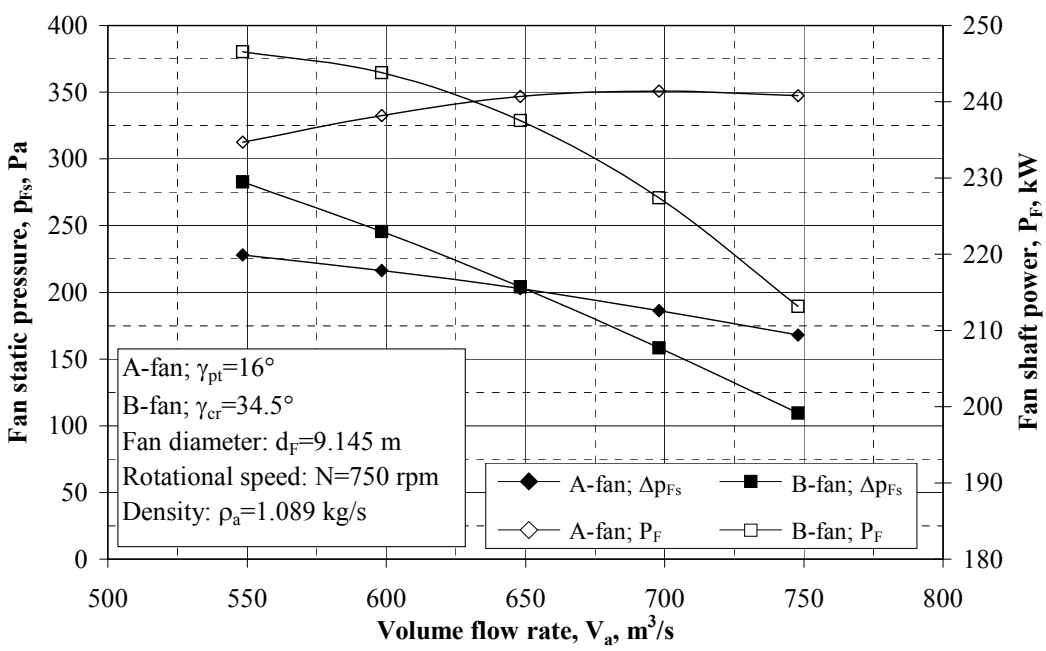

Figure 6.1. Numerically determined performance characteristics for A-fan on B-fan

The B-fan exhibits a steeper fan static pressure gradient compared to that of the A-fan. Close scrutiny of the axial velocity profiles in the actuator disc model of the A-fan and B-fan clarified the difference in the corresponding fan static pressure gradients. Figure 6.2 shows the axial velocity profiles for the A-fan and the B-fan at volume flow rates of 550 m^3/s and 650 m^3/s.

The flow blockage effect caused by the recirculation or backflow near the hub of the A-fan (refer to Figure 4.7) is clearly illustrated in the corresponding axial velocity profiles. It can be seen that for a flow rate of 550 m^3/s, only about 52% of the blade span is effectively utilised. Increasing the flow rate to 650 m^3/s results in reduced flow blockage, so that approximately 64% of the blade span is utilised. Thus, the effective through-flow area increases with flow rate. The conclusion drawn is that the average axial velocity is not proportional to the flow rate.

In contrast, the entire blade span of the B-fan operates below stall for the flow rates considered. With no flow blockage or recirculation occurring, the through-flow area remains constant and the average axial velocity is proportional to the flow rate.

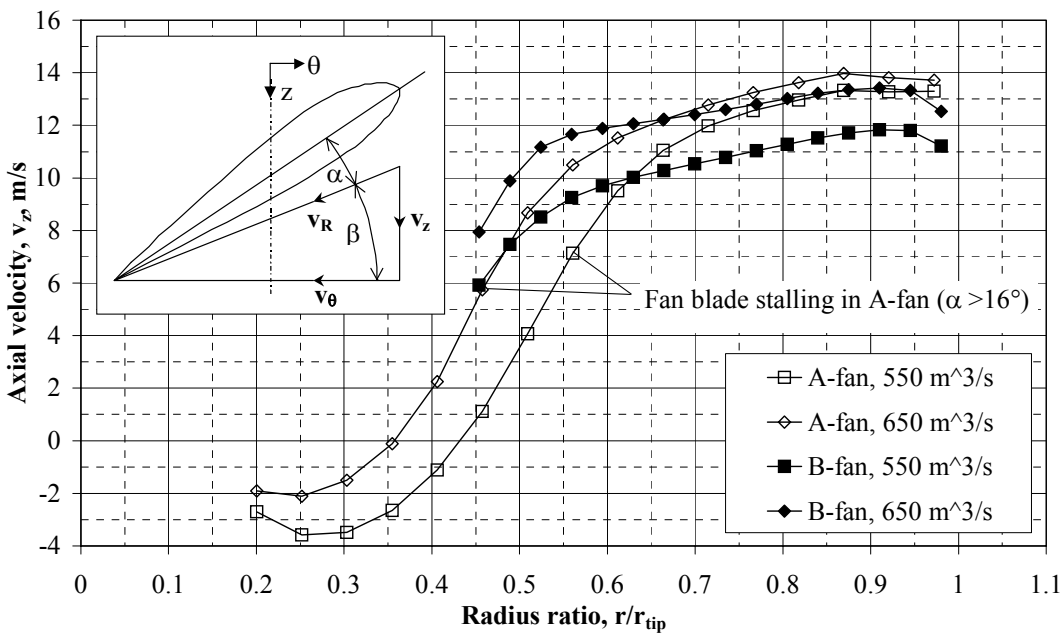

Figure 6.2. Axial velocity profiles in actuator disc model for A-fan and B-fan

It can be seen in Figure 6.2 that for a given change in flow rate, the corresponding change in axial velocity ($\mathbf{v_z}$), and consequently resultant relative velocity ($\mathbf{v_R}$), (referring especially to the velocities in the outer annulus near the blade tip, where most of the useful work is done) in the B-fan is greater than in the case of the A-fan. This effectively gives rise to a greater change in static pressure over the actuator disc model, due to the fact that the axial momentum source term given by equation 3.14, is proportional to $|\mathbf{v_R}|^2$, and therefore explains the steeper gradient displayed by the fan static pressure curve of the B-fan.

For an additional flow loss or pressure drop caused by inlet flow distortions, denoted δp_i, the resultant change in volume flow rate for the A-fan and B-fan is respectively δV_A and δV_B, with $\delta V_A > \delta V_B$, as illustrated in Figure 6.3.

Note however that although the fan characteristics are influenced by cross-flow and inlet flow distortion, as respectively reported by Stinnes (1998) and Thiart and von Backström (1993), the fan static pressure curve of the B-fan would still display a steeper gradient than that of the A-fan under similar inlet conditions. Stinnes (1998) compared the experimentally determined performance characteristics of two fans, having hub-tip ratios of respectively d_h/d_F=0.26 and d_h/d_F=0.4, over a range of off-axis inflow conditions. He reports similar trends as observed in this study, with the fan with d_h/d_F =0.26 being more sensitive to cross-flow than the fan with d_h/d_F =0.4. An important result emerging from this study is therefore the effect of hub-tip ratio on the performance of fans operating under distorted inlet conditions.

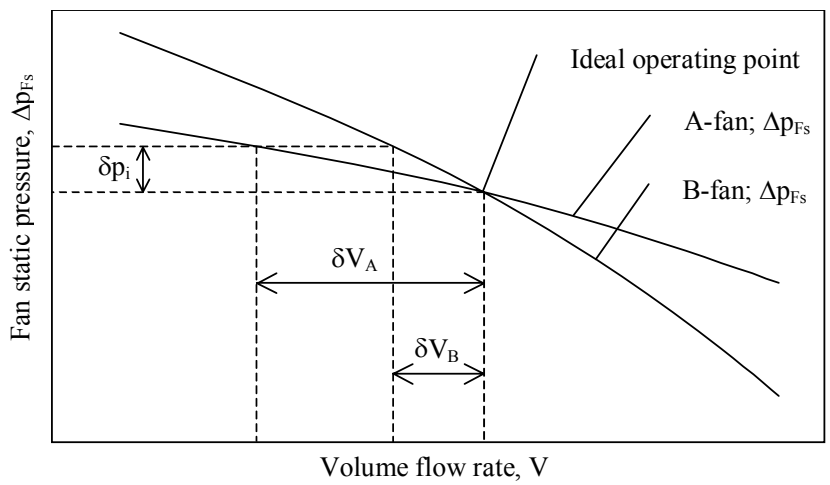

Figure 6.3. Effect of inlet flow distortion on volume flow rate

6.2.4. Effect of a walkway on fan performance

Previous experimental studies have shown that the volumetric effectiveness of the fans in an ACHE (or ACC) can significantly be improved by adding a walkway or by extending the fan platform. This was found to be especially applicable to the edge fans at low platform heights. In this part of the study the effect of a solid walkway with a width of W_w/d_F=0.33 was numerically investigated. At a platform height of H_i/d_F=1.53 (i.e., severely distorted inlet conditions), the numerically predicted volumetric effectiveness of the edge fan in the case of the A-fan and the B-fan were respectively 66.7% and 83.4%, corresponding to system volumetric effectiveness of 86.7% and 92.6%. From the vector and pressure plots it was concluded that the improvement in fan performance was mainly as a result of reduced cross-flow velocity and abatement of separation or distortion occurring at the inlet of the edge fan. The effectiveness of an ACSC can therefore be improved through relatively simple and economical modifications. Numerical techniques can successfully be used to design and evaluate such performance-enhancing walkways and windscreens.

6.2.5. Modelling of crosswind using an essentially two-dimensional approach

The final part of the study involved the modelling of the effect of a 3 m/s crosswind on fan performance in a section of the ACSC at a platform height of H_i=45 m, using an *essentially two-dimensional* modelling approach. This modelling approach led to average cross-flow velocities of up to 20 m/s being induced underneath the fan platform, resulting in backflow through the first two fan units. Therefore, the assumption that no flow crosses the sectional planes posed an unrealistic restriction on the numerical flow problem. The major difference between the *essentially two-dimensional* modelling approach under windless conditions and crosswind conditions, is that under windless conditions, the flow through the domain is driven or generated entirely by the actuator disc model(s). In contrast, under crosswind conditions, the flow is restricted to a confined channel-type flow by the velocity inlet and slip-wall boundary conditions, preventing the oncoming flow from moving around the plume and resulting in unrealistic plume dispersion. From these observations it can be concluded that the effective and realistic modelling of wind-effects require a *full three-dimensional* modelling approach.

6.3. Future Research

As mentioned above, the modelling of wind-effects require a *full three-dimensional* modelling approach, taking into account the entire ACSC. Such a model can be used to investigate performance reducing factors such as inlet flow distortions and recirculation. Also, it can be used to evaluate ways of improving performance through the use of such measures as windscreens, walkways, alternative inlet sections, and others.

The primary focus of this study was on the implementation and comparison of different numerical techniques and methods used in the modelling of ACHE and ACC. Experimental validation of numerical results of such complex thermal-flow problems is, however, imperative. Therefore, more attention should be paid to this aspect in future research.

Development and refinement of the actuator disc model into a useful fan design and analysis tool is another field of potential future research. Suggested improvements and modifications include the following:

(a) The use of improved fan blade lift and drag characteristics.

(b) The modelling of radial forces, in addition to axial and tangential forces.

(c) Determining the effect of different turbulence models.

(d) Under distorted inlet flow conditions, fan blades are subjected to severe cyclic loading. The actuator disc model can be used to analyse the aerodynamic forces on a fan blade.

The effective operation of an ACSC under excessive ambient temperatures may require additional wet cooling in order to maintain the backpressure on the steam turbines within specified limits. According to Kröger (2004), this may be achieved by deluging the heat exchanger bundles with water, or by precooling through humidification. Although deluging

may increase the heat transfer rate by a factor of up to five, disadvantages such as corrosion and fouling make it impractical and expensive, especially for large ACSC. Precooling by humidification or adiabatic cooling of the ambient air can be achieved by spraying water into the cooling air stream. To prevent corrosion, the spray should preferably not wet the finned tube surfaces. It is therefore advisable to locate the sprayers upstream of the fans, so as to allow the spray droplets to evaporate before they move through the heat exchangers bundles. FLUENT offers extensive Lagrangian particle-modelling capabilities (e.g., trajectory calculation, heat and mass transfer models) that can be employed to simulate precooling. These techniques can be used to strategically position the sprayers for optimum precooling.

Diminishing fossil fuel reserves and stringent environmental legislation require air-cooled power and petrochemical plants to be highly efficient. This study has shown that CFD can effectively be used to predict trends in fan performance, and therefore ACHE (or ACC) effectiveness.

7. References

Bender, T. J., Bergstrom, D. J. and Rezkallah, K. S., A Study on the Effects of Wind Intake Flow Rate of a Cooling Tower. Part 3: Numerical Study, *Journal of Wind Engineering and Industrial Aerodynamics,* Vol. 64, pp. 81-100, 1996. [96BE1]

British Standards Institution, Fans for General Purposes, Part 1, Methods for Testing Performance, BS 848, 1997. [97BS1]

Bruneau, P. R. P., The Design of a Single Rotor Axial Flow Fan for a Cooling Tower Application, MSc Thesis, Department of Mechanical Engineering, University of Stellenbosch, 1994. [94BR1]

Coetzee, R.V., Numerical simulation of an Air-cooled Heat Exchanger, MSc Thesis, Department of Mechanical Engineering, Potchefstroom University for Christian Higher Education, 2000. [00CO1]

Coetzee, R. V., and du Toit, C. G., Numerical Modeling of an Air-cooled Heat Exchanger, *R&D Journal of the South African Institution of Mechanical Engineering,* Vol. 20, No. 1, 2004. [04CO1]

du Toit, C. G., and Kröger, D.G., Modeling of the Recirculation in Mechanical Draft Heat Exchangers, *R&D Journal of the South African Institution of Mechanical Engineering,* Vol. 9, No. 1, pp. 2-8, 1993. [93DU1]

Duvenhage, K., and Kröger, D. G., Plume Recirculation in Mechanical Draft Air-cooled Heat Exchangers, *Heat Transfer Engineering,* Vol. 16, No. 4, 1995. [95DU1]

Duvenhage, K., and Kröger, D. G., The Influence of Wind on the Performance of Forced Draft Air-Cooled Heat Exchangers, *Journal of Wind Engineering and Industrial Aerodynamics,* Vol. 62, pp. 259-277, 1996. [96DU1]

Duvenhage, K., Vermeulen, J. A., Meyer, C. J., and Kröger, D.G., Flow Distortions at the Fan Inlet of Forced Draft Air-cooled Heat Exchangers, *Applied Thermal Engineering,* Vol. 16, No. 8/9, pp.741-752, 1996. [96DU2]

Eurocode 1: Actions on Structures, EN 1991-1-4 General actions- Wind actions, 1991. [91EU1]

Goldschagg, H. B., Lessons Learned from the World's Largest Forced Draft Direct Air-cooled Condenser, Paper presented at the EPRI Int. Symp. On Improved Technology for Fossil Fuel Power Plants – New and Retrofit Applications, Washington, 1993. [93GO1]

Gunter, A.Y., and Shipes, K.V., Hot Air Recirculation by Air-coolers, Paper presented at the Twelfth National Heat Transfer Conference (AIChE –ASME), Tulsa, Oklahoma, USA, 1971. [71GU1]

Hoerner, S. F., *Fluid-dynamic Drag,* Brick Town, New York, 1965. [65HO1]

Hoerner, S. F., and Borst, H.V., *Fluid-dynamic Lift,* Brick Town, New York, 1975. [75HO1]

Hotchkiss, P., Development of a Rotor Model for the Numerical Simulation of Helicopter Exterior Flow-fields, MSc Thesis, Department of Mechanical Engineering, University of Cape Town, 2004. [04HO1]

Houghton, E. L., and Carpenter, P. W., *Aerodynamics for Engineering Students,* Edward Arnold, London, 1982. [82HO1]

Kröger, D.G., Reduction in Performance Due to Recirculation in Mechanical Draft Cooling Towers, *Heat Transfer Engineering,* Vol. 10, No. 4, pp. 37-43, 1989. [89KR1]

Kröger, D.G., *Air-cooled Heat Exchangers and Cooling Towers,* PennWell Corp., Tulsa, 2004. [04KR1]

Launder, B. E., and Spalding, D. B., The Numerical Computation of Numerical Flows, *Computer Methods in Applied Mechanics and Engineering,* Vol. 3, pp. 269-289, 1974. [74LA1]

McGhee, R. J., Beasley, W. D., and Somers, D. M., Low-speed Characteristics of a 13-percent-thick Airfoil Section Designed for General Aviation Applications, NASA Technical Memorandum, NASA TM X-72697, 1977. [77MC1]

Menter, F. R., Two-Equation Eddy-Viscosity Turbulence Models for Engineering Applications, AIAA Journal, Vol. 32, No. 8, pp. 1598-1605, 1994. [94ME1]

Meyer, C. J., A Numerical Investigation of the Plenum Chamber Aerodynamic Behavior of Mechanical Draught Air-cooled Heat Exchangers, PhD Thesis, Department of Mechanical Engineering, University of Stellenbosch, 1992. [00ME1]

Meyer, C. J., and Kröger, D.G., Plenum Chamber Flow Losses in Forced Draft Air-cooled Heat Exchangers, *Applied Thermal Engineering,* Vol. 18, pp.875-893, 1998. [98ME1]

Meyer, C. J., and Kröger, D. G., A Numerical Investigation of the Errors Associated with the Scaling of Axial Flow Fan Performance Characteristics, *R&D Journal of the South African Institution of Mechanical Engineering,* Vol. 20, No. 4, 2004. [04ME1]

Patankar, S. V., *Numerical Heat Transfer,* McGraw-Hill, New York, 1980. [80PA1]

Pericleous, K. A., and Patel, M.K., The Modeling of Tangential and Axial Agitators in Chemical Reactors, *Physicochemical Hydrodynamics,* Vol. 8, pp.105-123, 1986.[86PE1]

Richards, P. J., and Hoxey, R. P., Appropriate Boundary Conditions for Computational Wind Engineering Models using the k-ε Turbulence Model, *Journal of Wind Engineering and Industrial Aerodynamics,* Vol. 46/47, pp. 145-153, 1993. [93RI1]

Rogers, J. A., Won, K., and Stang, W., Validation of CFD Models for Evaluating Hot-air-recirculation in Air-cooled Heat Exchangers, Paper presented at the AIChE Spring Meeting, Houston, Texas, USA 1999. [99RO1]

Salta, C. A., and Kröger, D. G., Effect of Inlet Flow Distortions on Fan Performance in Forced Draft Air-cooled Heat Exchangers, *Heat Recovery Systems & CHP,* Vol. 15, No. 6, pp. 555-561, 1995. [95SA1]

Schlichting, H., *Boundary Layer Theory,* McGraw-Hill, New York, 1960. [60SC1]

Schreüder, W.A., and du Plessis, J.P., Numerical Modeling of Interior Boundaries, *Numerical Heat Transfer,* Vol. 17, pp. 197-215, 1990. [90SC1]

Stinnes, W., The Performance of Axial Fans Subjected to Forced Cross-flow at Inlet, MSc Thesis, Department of Mechanical Engineering, University of Stellenbosch, 1998. [98ST1]

Turner, J. T., The Aerodynamics of Forced Draft Air-cooled Heat Exchangers, International Symposium on Cooling Systems, BHRA Fluid Engineering, Cranfield, England, pp. 81-99, 1975. [75TU1]

Thiart, G. D., A Numerical Procedure for Predicting the Effects of Distorted Inflow Conditions on the Performance of Axial Flow Fans, PhD Thesis, Department of Mechanical Engineering, University of Stellenbosch, 1990. [90TH1]

Thiart, G. D., and von Backström, T. W., Numerical Simulation of the Flow Field near an Axial Flow Fan Operating under Distorted Inflow Conditions, *Journal of Wind Engineering and Industrial Aerodynamics,* Vol. 45. pp. 189-214, 1993. [93TH1]

van Aarde, D. J., Vloeiverliese deur ’n A-raam Vinbuisbundel in ’n Lugverkoelde Kondensator, MSc Thesis, Department of Mechanical Engineering, University of Stellenbosch, 1990. [90VA1]

Van Dam, C. P., Recent Experience with Different Methods of Drag Prediction, *Progress in Aerospace Science,* Vol. 35, pp. 751-798, 1999. [99VA1]

van Staden, M. P., An Integrated Approach to Transient Simulation of Large Air-cooled Condensers using Computational Fluid Dynamics, PhD Thesis, Department of Mechanical Engineering, Rand Afrikaans University, 2000. [00VA1]

van Staden, M. P., and Pretorius, L., Integrated Approach to CFD Modelling of Air-cooled Condensers, Paper presented at the 1st South African Conference on Applied Mechanics (SACAM), Midrand, South Africa, 1996. [96VA1]

Venter, S. J., The Effectiveness of Axial Flow Fans in A-frame Plenums, MSc Thesis, Department of Mechanical Engineering, University of Stellenbosch, 1990. [90VE1]

Versteeg, H. K., and Malalasekera, W., *An Introduction to Computational Fluid Dynamics,* Prentice Hall, Harlow, 1995. [95VE1]

Von Gossler, J., Effects of Screens on the Performance of Fans in Forced Draft Air-Cooled Heat Exchangers, BEng Mechanical Project, Department of Mechanical Engineering, University of Stellenbosch, 2004. [04VA1]

Wallis, R. A., *Axial Flow Fans and Ducts,* Willey, New York, 1980. [80WA1]

White, F. M., *Viscous Fluid Flow,* McGraw-Hill, New York, 1991. [91WH1]

8. Nomenclature

A	Area, m^2
C	Constant
C_D	Drag coefficient
C_L	Lift coefficient
c	Chord length, m
c_p	Specific heat at constant pressure, J/kgK (joule per kilogram-kelvin)
D	Drag force, Newtons
d	Diameter, m
e	Effectiveness
F	Momentum source term, N/m^3
f	Force, N
G	Production term
H	Height, m
h	Vertical distance above the ground, m
K	Loss coefficient
k	Turbulent kinetic energy, m^2/s^2
L	Length, m or lift force, N
M	Fan shaft torque, Nm
m	Mass flow rate, kg/s
N	Rotational speed, rpm
n	Number
P	Power, W
p	Pressure, Pa
Q	Heat transfer rate, W
R	Gas constant, J/kgK
r	Radial co-ordinate, or radius, m
S	Source term
T	Temperature, °C or K
t	Axial thickness of the actuator disc model, m
u	x-velocity component, m/s
u_*	Friction velocity, m/s
V	Volume flow rate, m^3/s
v	y-velocity component, m/s, or velocity, m/s
$\mathbf{v}$	Velocity vector, m/s
W	Width, m
w	z-velocity component, m/s
x	Co-ordinate
y	Co-ordinate
z	Co-ordinate
z_0	Surface roughness length, m

Greek symbols

α	Angle of attack, °
β	Relative flow angle, °
β_T	Thermal expansion coefficient, 1/K
Δ	Differential

δ	Incremental
ε	Dissipation rate of turbulent kinetic energy, m^2/s^3
ϕ	Field variable
Γ	Diffusion coefficient
γ	Blade angle
η	Efficiency, %
κ	von Karman constant
μ	Viscosity, kg/ms
θ	Angle, °, or tangential co-ordinate
ρ	Density, kg/m^3
σ	Area ratio, or blade solidity, or constant in k-ε turbulence model
Ω	Angular velocity, rad/s (radian per second)

Dimensionless Groups

Pr	Prandtl number, $\mu c_p/k$
Re	Reynolds number, $\rho vL/\mu$

Subscripts

a	Air, or ambient
b	Bundle
c	Chord, or contraction
d	Dynamic
do	Downstream
E	Energy
e	Effective
F	Fan
fr	Frontal
gauge	Gauge
h	Hub
he	Heat exchanger
i	Numerical index, 1,2,3…
in	Inlet
j	Jetting
m	Mean
o	Outlet
p	Practice
R	Relative
r	Reference, or root
s	Static, or steam
sc	Settling chamber
sys	System
T	Test, or thermal
t	Tip, or tube
tot	Total
up	Upstream
V	Volumetric
w	Walkway, or wind, or windwall

9. Glossary

ACC	air-cooled condenser
ACHE	air-cooled heat exchanger
ACSC	air-cooled steam condenser
CFD	computational fluid dynamics code
FLUENT	A CFD code
kW	kilowatt
m	meter
m/s	meters per second
m^3/s	cubic meters per second
MW	megawatt
MW(e)	megawatt (electrical)
NASA	National Aeronautics and Space Administration
rpm	rotations per minute
SST	shear stress transport

Appendix A. System Specifications

A.1. ACSC fan unit specifications

The following specifications are applicable to a typical A-frame fan unit in an array of fan units in an ACSC. A schematic illustration of such a unit is shown in figure A.1.

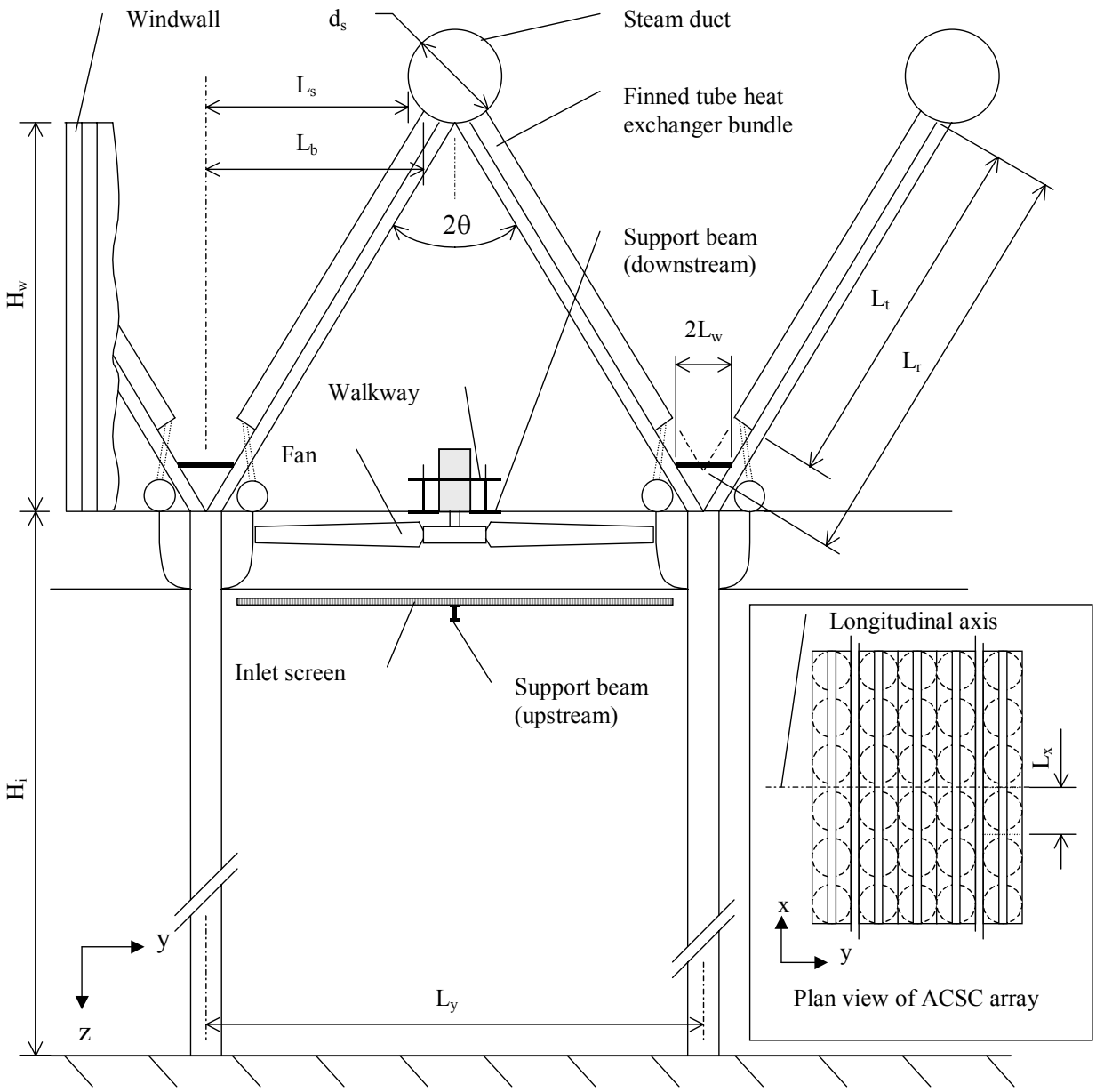

Figure A.1: ACSC fan unit dimensions

A.1.1. Atmospheric and steam design conditions

Air temperature at ground level	T_a=20 ºC
Barometric pressure at ground level	p_a=91330 Pa
Saturated steam supply temperature	T_v=60 ºC

A.1.2. Air properties

The thermo-physical properties of air, evaluated at ambient temperature and pressure, are given below:

Density	ρ_a=1.085 kg/s
Thermal conductivity	k_a=0.02559 W/mK
Specific heat	c_p=1006.729 W/kgK
Molecular viscosity	μ_a=1.849 × 10^{-5} kg/ms
Prandtl number	Pr=0.71133

A.1.3. Finned tube bundle specifications

Number of heat exchanger bundles above one fan	n_b=8
Frontal area of one bundle	A_{fr}=27.434 m^2
Effective finned tube length	L_t=9.55 m
Heat exchanger apex angle	2θ=56º
Number of finned tubes tube rows	n_r=2
Number of finned tubes per bundle in the first row	n_{tb1}=57
Number of finned tubes per bundle in the second row	n_{tb2}=58
Ratio of minimum to free stream flow area through finned tube bundle	σ=0.41
Ratio of minimum to free stream flow area at inlet of finned tube bundle	σ_{21}=0.86

The experimentally determined characteristic heat transfer parameter, Ny, for normal flow through the first row of tubes is

$$Ny_1 = 583.8307 Ry^{0.4031} \tag{A.1}$$

and for the second row

$$Ny_2 = 1277.726 Ry^{0.3806} \tag{A.2}$$

The loss coefficient for both rows under normal flow conditions is

$$K_{he} = 4464.831 Ry^{-0.43927} \tag{A.3}$$

where Ny and Ry are respectively defined by equation A.4 and equation A.5.

$$Ny = \frac{hA}{k_a A_{fr} \Pr^{0.333}} \tag{A.4}$$

and

$$Ry = \frac{m_a}{\mu_a A_{fr}} \tag{A.5}$$

Note that in equation A.4 and equation A.5, A_{fr} and m_a refer to the total frontal area and the corresponding mass flow rate.

A.2. Upstream and downstream obstacles

The following dimensions refer to obstacles upstream and downstream of the fan, as shown in figure A.1.

Inlet screen distance from fan blade (upstream)	x_{si}=1.29 m
Support beam distance from fan blade (upstream)	x_{bi}=1.336 m
Support beam distance from fan blade (downstream)	x_{bo}=0.5345 m
Walkway distance from fan blade (downstream)	x_{wo}=0.995 m
Ratio of inlet screen area to fan casing area	σ_{si}=0.109
Ratio of support beam area to fan casing area (upstream)	σ_{bi}=0.154
Ratio of support beam area to fan casing area (downstream)	σ_{bo}=0.0523
Ratio of walkway area to fan casing area	σ_{wo}=0.0912

A.3. Platform dimensions

With reference to figure A.1, the following dimensions are given

Average steam header diameter	d_s=2.34 m
Half-width of walkway between A-frames	L_w=0.397 m
Height of windwall	H_w=10 m
Dimension shown in figure A.1.	L_x=10.56 m
Dimension shown in figure A.1.	L_y=11.8 m
Dimension shown in figure A.1.	L_r=10.6 m
Dimension shown in figure A.1.	L_b=4.924 m
Dimension shown in figure A.1.	L_s=4.102 m

A.4. Effective system resistance

In this section the effective system resistance of the ACSC is calculated. Equations based on extensive experimental and theoretical research by Kröger (2004), are used to evaluate the loss coefficients. For the calculation of the loss coefficients the flow is assumed to be isothermal. Variation in thermo-physical properties is also neglected.

A.4.1. Definition of loss coefficients in an ACSC

For ease of reference, the effective system resistance, Δp_e, given by equation 3.6, is repeated here

$$\Delta p_e = -\left[K_{ts} \frac{1}{2\rho_{a1}} \left(\frac{m_a}{n_b A_{fr}} \right)^2 + K_{up} \frac{1}{2\rho_{a3}} \left(\frac{m_a}{A_e} \right)^2 + K_{do} \frac{1}{2\rho_{a3}} \left(\frac{m_a}{A_e} \right)^2 + K_{\theta t} \frac{1}{2\rho_{a56}} \left(\frac{m_a}{n_b A_{fr}} \right)^2 \right] \tag{A.6}$$

$K_{\theta t}$ is the total loss coefficient across the heat exchanger bundles and includes the kinetic energy losses at the outlet of the A-frame. For isothermal flow $K_{\theta t}$ is given by

$$K_{\theta t} = K_{he} + \left(\frac{1}{\sin\theta_m} - 1 \right) \left[\left(\frac{1}{\sin\theta_m} - 1 \right) + 2K_{ci}^{0.5} \right] + K_{dj} + K_o \tag{A.7}$$

where θ_m is the actual mean flow incidence angle and is given as a function of the semi-apex angle in the following empirical equation

$$\theta_m = 0.0019\theta^2 + 0.9133\theta - 3.1558 \tag{A.8}$$

The heat exchanger loss coefficient for normal isothermal flow, K_{he}, is given by equation A.3. K_{ci} is the entrance contraction loss coefficient for normal flow and is based on the normal approach free stream velocity.

$$K_{ci} = \left[\frac{1 - 1/\sigma_c}{\sigma} \right]^2 \tag{A.9}$$

where σ_c is a function of σ_{21}, is given by the following empirical equation

$$\sigma_c = 0.6155417 + 0.04566493\sigma_{21} - 0.336651\sigma_{21}^2 + 0.4082743\sigma_{21}^3 + 2.672041\sigma_{21}^4 - 5.963169\sigma_{21}^5 + 3.558944\sigma_{21}^6 \tag{A.10}$$

The jetting loss coefficient is expressed by the following correlation

$$K_{dj} = \left[\left\{ -2.89188\left(\frac{L_w}{L_t} \right) + 2.93291\left(\frac{L_w}{L_t} \right)^2 \right\} \left(\frac{L_t}{L_s} \right) \left(\frac{L_b}{L_s} \right) \left(\frac{28}{\theta} \right)^{0.4} + \left\{ \left(\frac{L_s}{L_b} \right) \exp\left(2.36987 + 5.8601\times10^{-2}\theta - 3.3797\times10^{-3}\theta^2 \right) \right\}^{0.5} \left(\frac{L_t}{L_r} \right) \right]^2 \tag{A.11}$$

where θ is in degrees. Refer to figure A.1 for the length dimensions denoted by L and an appropriate subscript.
The outlet loss coefficient is given by

$$K_o = \left[\left\{ -2.89188\left(\frac{L_w}{L_t}\right) + 2.93291\left(\frac{L_w}{L_t}\right)^2 \right\}\left(\frac{L_s}{L_b}\right)^3 + 1.9874 - 3.02783\left(\frac{d_s}{2L_b}\right) + 2.0187\left(\frac{d_s}{2L_b}\right)^2 \right]\left(\frac{L_t}{L_s}\right)^2 \tag{A.12}$$

Loss coefficients resulting from upstream and downstream obstacles, K_{up} and K_{do}, are based on the mean velocity through the fan. These coefficients are given by Kröger (2004) in empirical relations as a function the projected area of the obstacle and the distance from the fan. The upstream obstacles that are of importance are the inlet screen and the screen support beam. Important downstream obstacles are the fan drive system support beam and walkway (refer to figure A.1). The pressure drop resulting from the platform supports is taken into account by the loss coefficient K_{ts}.

A.4.2. Evaluation of loss coefficients

The loss coefficient are evaluated for the air properties given in section A.1.2.

K_{he} is evaluated according to equation A.3

$$K_{he} = 4464.831 Ry^{-0.43927} = 4464.831\left(\frac{m_a}{\mu_a n_b A_{fr}}\right)^{-0.43927} = 4464.831\left(\frac{m_a}{1.849\times10^{-5}\cdot 8\cdot 27.434}\right)^{-0.43927}$$
$$= 397.3837 m_a^{-0.43927}$$

θ_m is given by equation A.8

$$\theta_m = 0.0019\theta^2 + 0.9133\theta - 3.1558 = 0.0019\cdot 28^2 + 0.9133\cdot 28 - 3.1558 = 23.91°$$

where, according to equation A.10, σ_c is

$$\sigma_c = 0.6155417 + 0.04566493\cdot 0.86 - 0.336651\cdot 0.86^2 + 0.4082743\cdot 0.86^3 + 2.672041\cdot 0.86^4 - 5.963169\cdot 0.86^5 + 3.558944\cdot 0.86^6 = 0.761$$

so that contraction loss coefficient given by equation A.9 is

$$K_{ci} = \left[\frac{1 - 1/0.761}{0.41}\right]^2 = 0.587$$

The jetting loss coefficient is calculated according to equation A.11

$$K_{dj} = \left[\left\{-2.89188\left(\frac{0.397}{9.55}\right)+2.93291\left(\frac{0.397}{9.55}\right)^2\right\}\left(\frac{9.55}{4.102}\right)\left(\frac{4.924}{4.102}\right)\left(\frac{28}{28}\right)^{0.4}\right.$$

$$\left.+\left\{\left(\frac{4.102}{4.924}\right)\exp\left(2.36987+5.8601\times10^{-2}\cdot28-3.3797\times10^{-3}\cdot28^2\right)\right\}^{0.5}\left(\frac{9.55}{10.6}\right)\right]^2$$

$$=1.696$$

According to equation A.12 the outlet loss coefficient is given as

$$K_o = \left[\left\{-2.89188\left(\frac{0.397}{9.55}\right)+2.93291\left(\frac{0.397}{9.55}\right)^2\right\}\left(\frac{4.102}{4.924}\right)^3+1.9874\right.$$

$$\left.-3.02783\left(\frac{2.34}{2\cdot4.924}\right)+2.0187\left(\frac{2.34}{2\cdot4.924}\right)^2\right]\left(\frac{9.55}{4.102}\right)^2$$

$$=7.129$$

The total loss coefficient across the heat exchanger bundles can now be calculated in terms of m_a.

$$K_{\theta t} = K_{he}+\left(\frac{1}{\sin\theta_m}-1\right)\left[\left(\frac{1}{\sin\theta_m}-1\right)+2K_{ci}^{0.5}\right]+K_{dj}+K_o$$

$$=397.3837m_a^{-0.43927}+\left(\frac{1}{\sin 23.906}-1\right)\left[\left(\frac{1}{\sin 23.906}-1\right)+2\cdot0.587^{0.5}\right]+1.696+7.129$$

$$=397.3837m_a^{-0.43927}+13.232$$

The upstream and downstream loss coefficients, according to Kröger (2004), are given in table A.1.

Table A.1: **Upstream and downstream loss coefficients**

Upstream or downstream	Obstacle	x_{ob}/d_c	A_{ob}/A_c	Loss coefficient
Upstream	Screen	0.140	0.109	0.11
Upstream	Support Beam	0.145	0.154	0.17
Downstream	Support Beam	0.058	0.0523	0.16
Downstream	Walkway	0.108	0.0912	0.19

Based on table A.1 the upstream and down stream loss coefficients are K_{up}=0.28 and K_{do}=0.35, respectively. Equation A.6 can now be written in terms of mass flow rate

$$\Delta p_e = -\left\{ \frac{1.6033}{2 \cdot 1.085(8 \cdot 27.434)^2} m_a^2 + \frac{0.28}{2 \cdot 1.085\left[\pi / 4\left(9.216^2 - 1.4^2\right)\right]^2} m_a^2 \right.$$

$$\left. + \frac{0.35}{2 \cdot 1.085\left[\pi / 4\left(9.216^2 - 1.4^2\right)\right]^2} m_a^2 + \frac{\left(397.3847 m_a^{-0.43927} + 13.232\right)}{2 \cdot 1.085(8 \cdot 27.434)^2} m_a^2 \right\}$$

$$= -\left(2.1029 \times 10^{-4} m_a^2 + 3.8018 \times 10^{-3} m_a^{1.56073}\right) \quad , Pa$$

or in terms of the volume flow rate V_a

$$\Delta p_e = -\left(2.4756 \times 10^{-4} V_a^2 + 4.31807 \times 10^{-3} V_a^{1.56073}\right) \quad , Pa \qquad \text{(A.13)}$$

Appendix B. Fan Installation Specifications

B.1. Fan installation dimensions

As mentioned in section 1.3, the performance of two types of axial fans are numerically investigated in this study. Fan blade geometry and performance characteristics, for the A-fan and B-fan are given in section B.2 and section B.3 respectively. Dimensions and specifications of the fan system in a typical fan unit in the ACSC under consideration are given below.

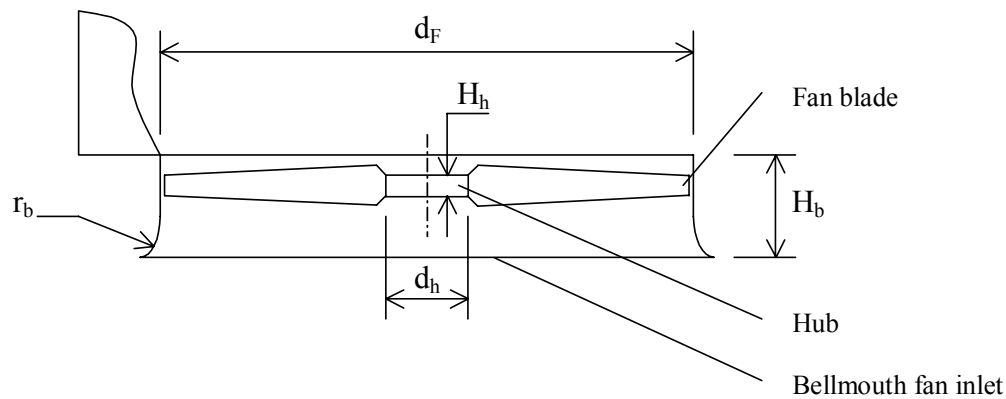

Figure B.1: Fan system dimensions

Fan diameter	d_F=9.145 m
Hub-tip ratio of A-fan	d_h/d_F=0.153
Hub-tip ratio of B-fan	d_h/d_F=0.4
Ratio of hub thickness to fan diameter of A-fan	H_h/d_h=0.02
Ratio of hub thickness to fan diameter of B-fan	H_h/d_h=0.1
Height of bellmouth fan inlet from fan platform	H_b=1.92 m
Bellmouth inlet radius	r_b=1.16 m
Number of fan blades	n_F=8
Rotational speed	N=125 rpm

B.2. A-fan specifications

The A-fan is an actual mass-produced commercial cooling fan. Information regarding its blade geometry was unavailable and therefore had to be determined by measurement. The performance characteristics given in section B.2.2 were obtained from the manufacturer. A single fan blade of the A-fan is shown in figure B.2.

Figure B.2: Photographic image of a single fan blade of the A-fan

B.2.1. Blade geometry of the A-fan

Figure B.3 shows the main dimensions of the A-fan blade.

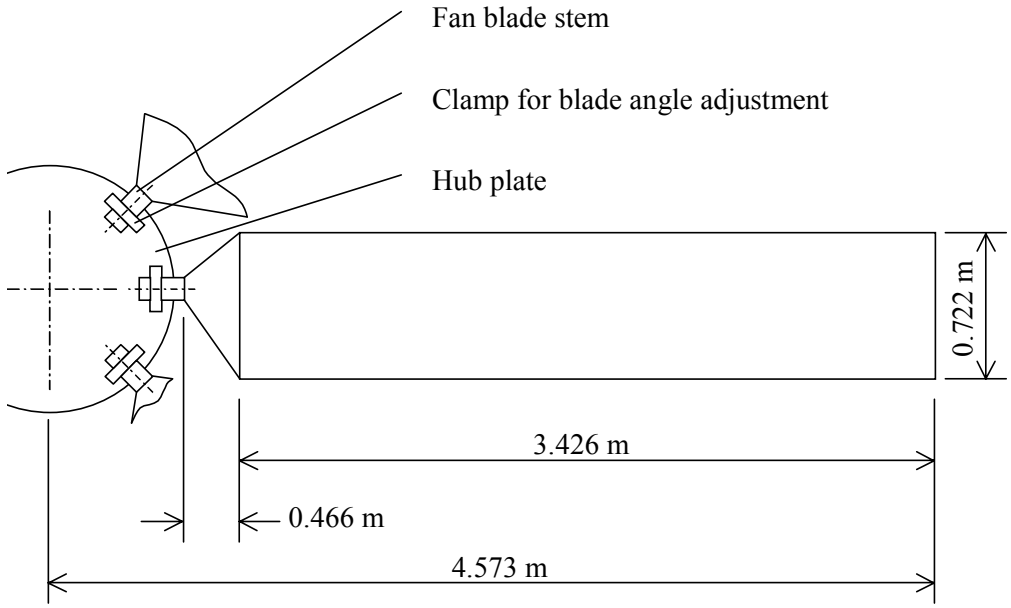

Figure B.3: A-fan blade dimensions

The A-fan employs a blade profile shown in figure B.4.

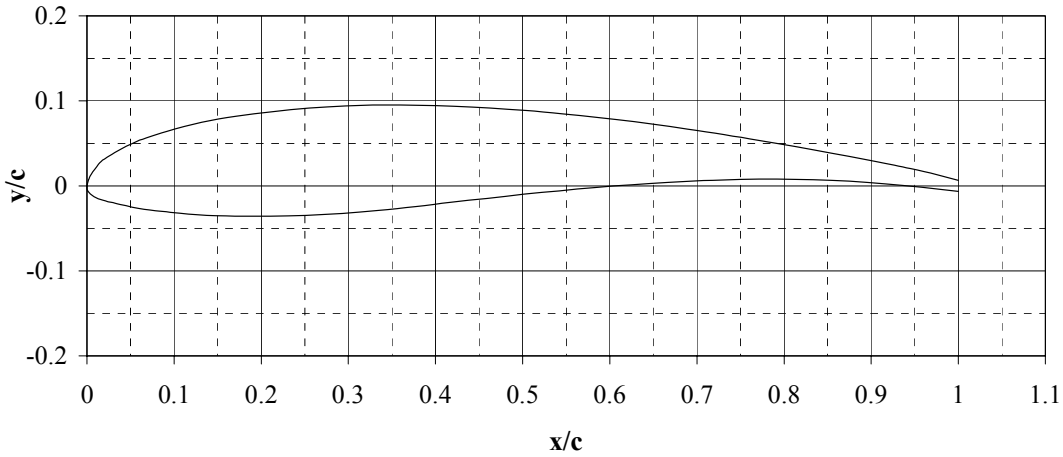

Figure B.4: A-fan blade profile

The blade angle distribution at a blade angle setting of, γ_{pt}=16°, is given in figure B.5.

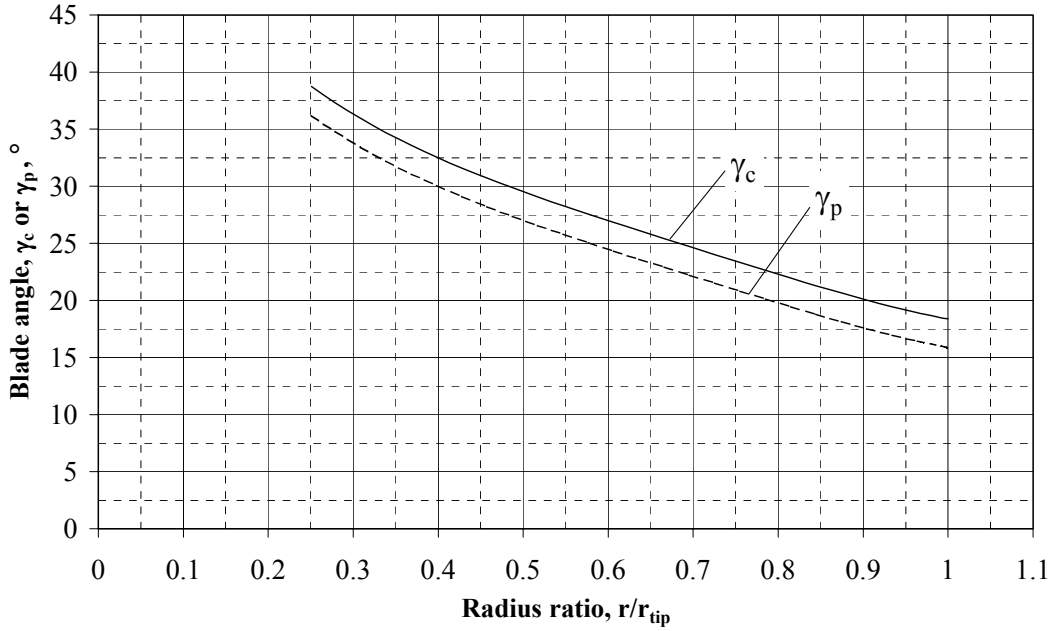

Figure B.5: Blade angle distribution at γ_{pt}=16°

B.2.2. Performance characteristics of the A-fan

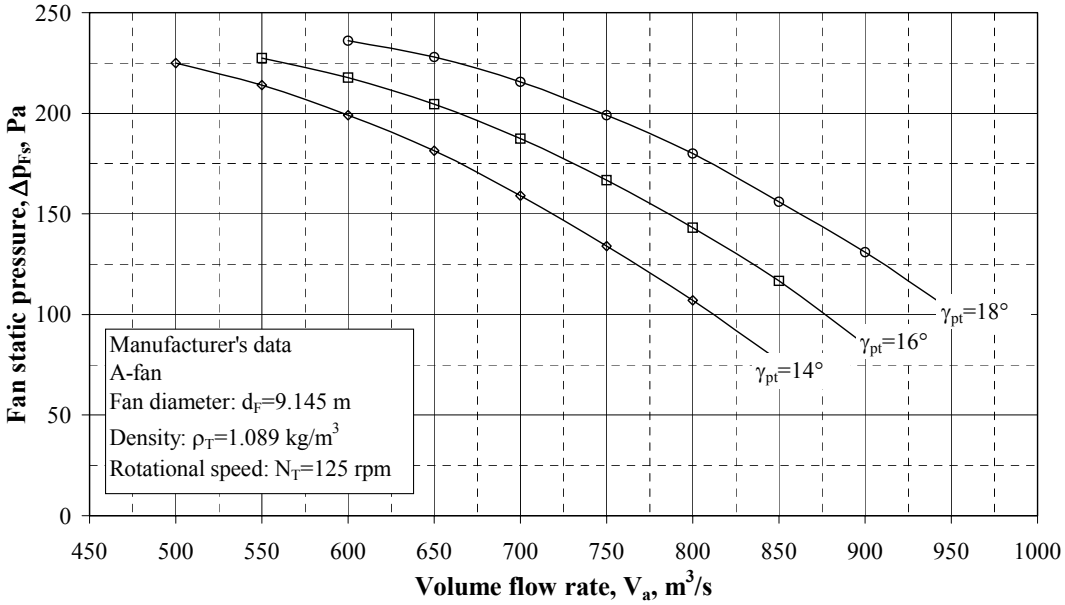

Figure B.6: Fan static pressure characteristic of the A-fan

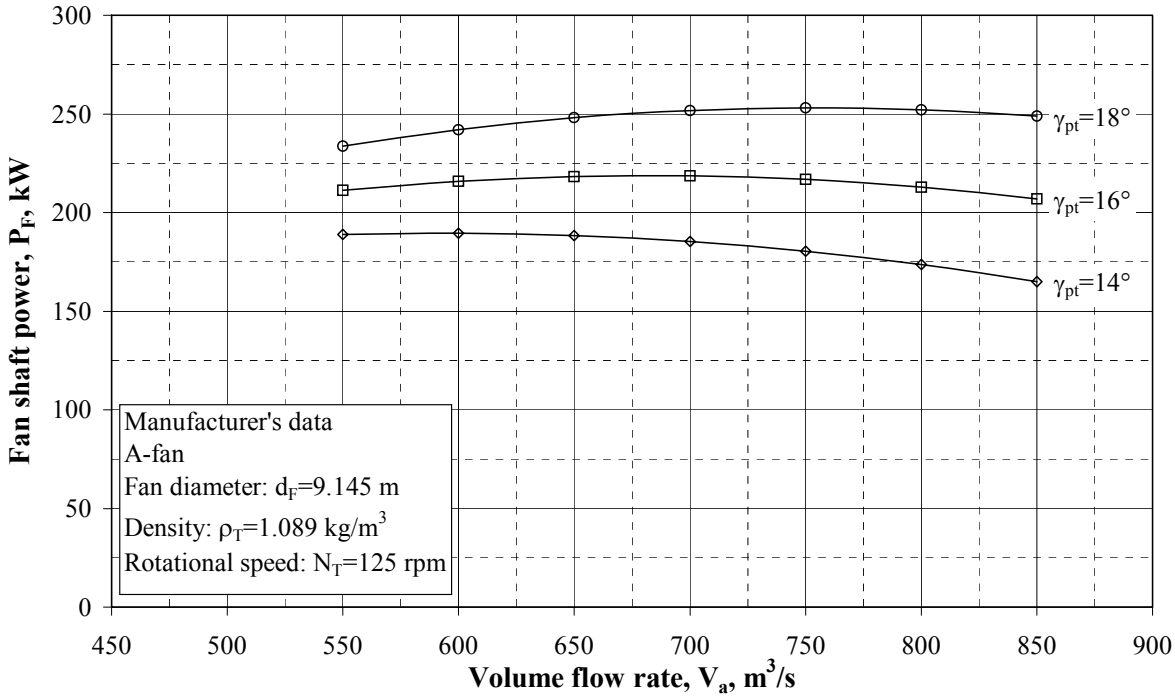

Figure B.7: Fan shaft power characteristic of the A-fan

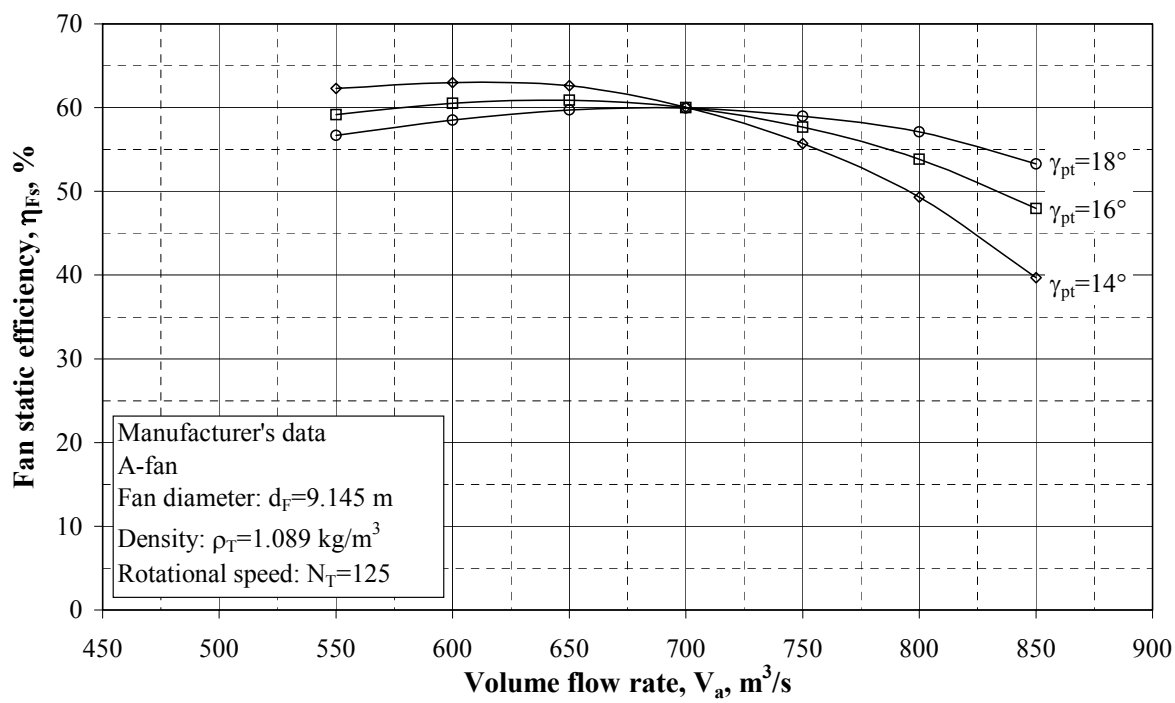

Figure B.8: Fan static efficiency of the A-fan

B.3. B-fan specifications

The B-fan is a prototype fan designed by Bruneau (1994) for application in an actual ACSC. A scale model with a diameter of d_F=1.542 m was built and tested at the Department of Mechanical Engineering, University of Stellenbosch. The characteristics of the model fan determined according to BS848 (British Standards Institution 1997) for a type A configuration, are given in section B.3.2. Figure B.9 shows the model B-fan from inside the settling chamber of the fan test facility.

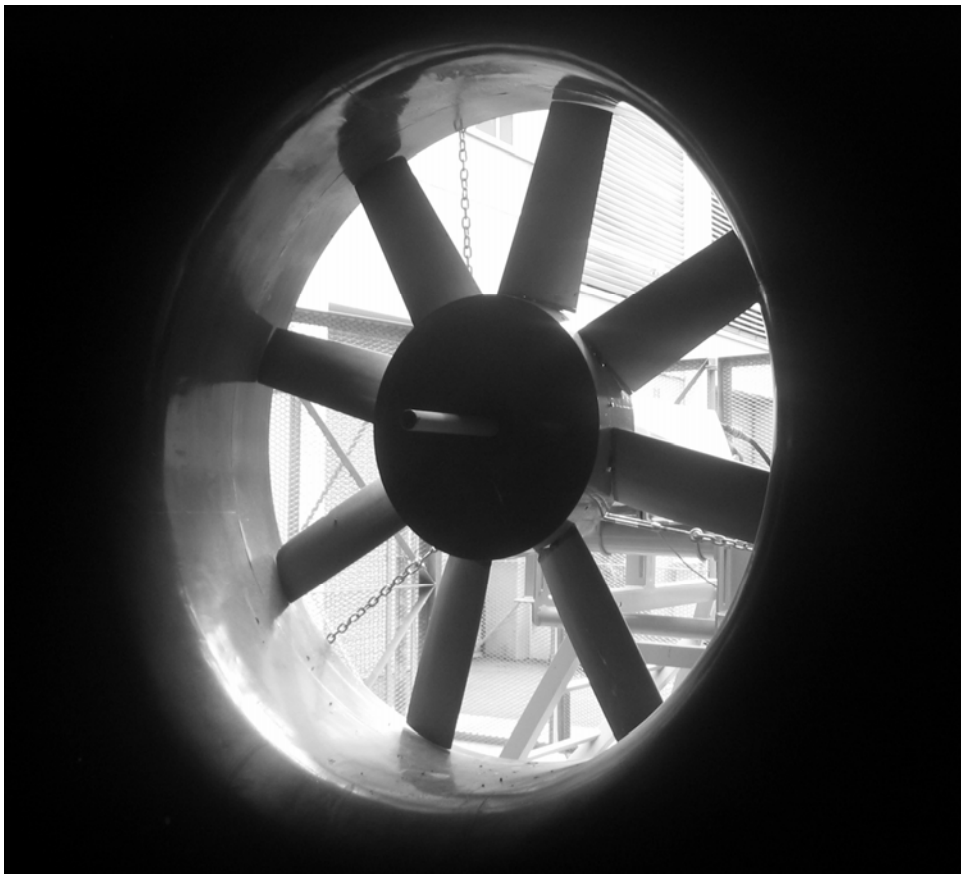

Figure B.9: Photographic image of the model B-fan

B.3.1. Blade geometry of the B-fan

The B-fan employs an NASA GA(W)-2 airfoil, the characteristics of which were determined by McGhee et al. (1977).

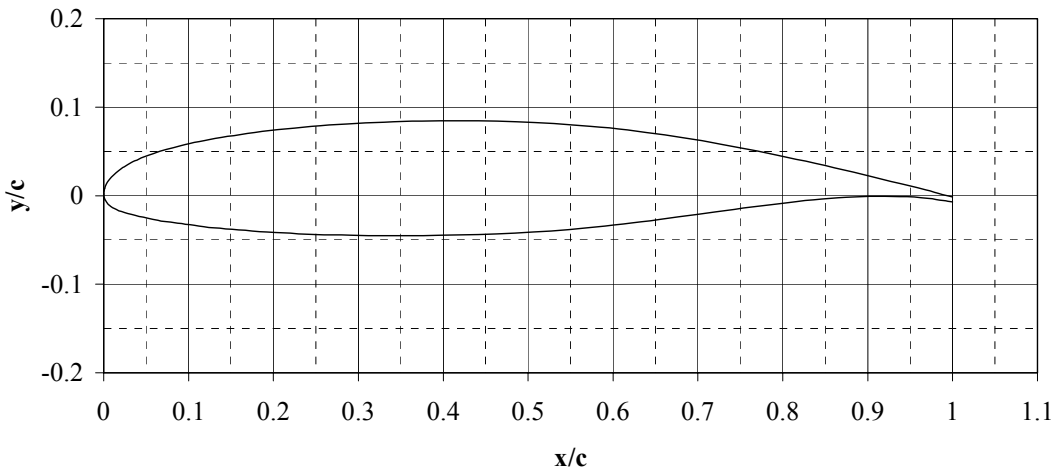

Figure B.10: B-fan blade profile, NASA GA(W)-2, McGhee et al. (1977)

The variation in blade angle referenced to the chord line, γ_c, and chord length, c, for d_F=1.542 m and γ_{cr}=30° is given in figure B.11 as a function of radius ratio.

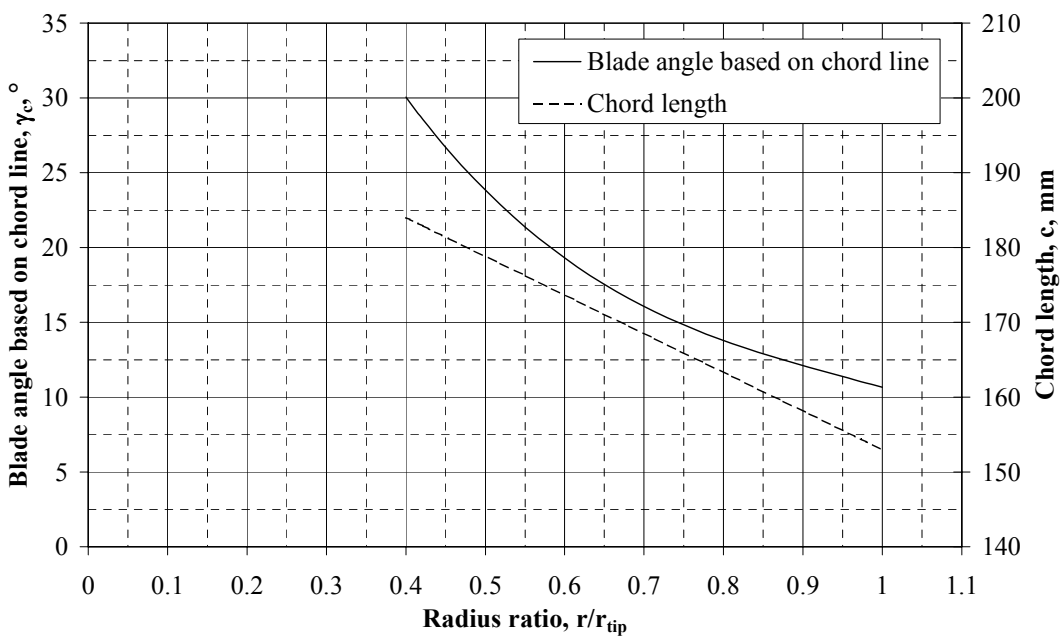

Figure B.11: Blade angle at γ_{cr}=30° and chord length as a function of r/r_{tip}

B.3.2. Performance characteristics of the B-fan model

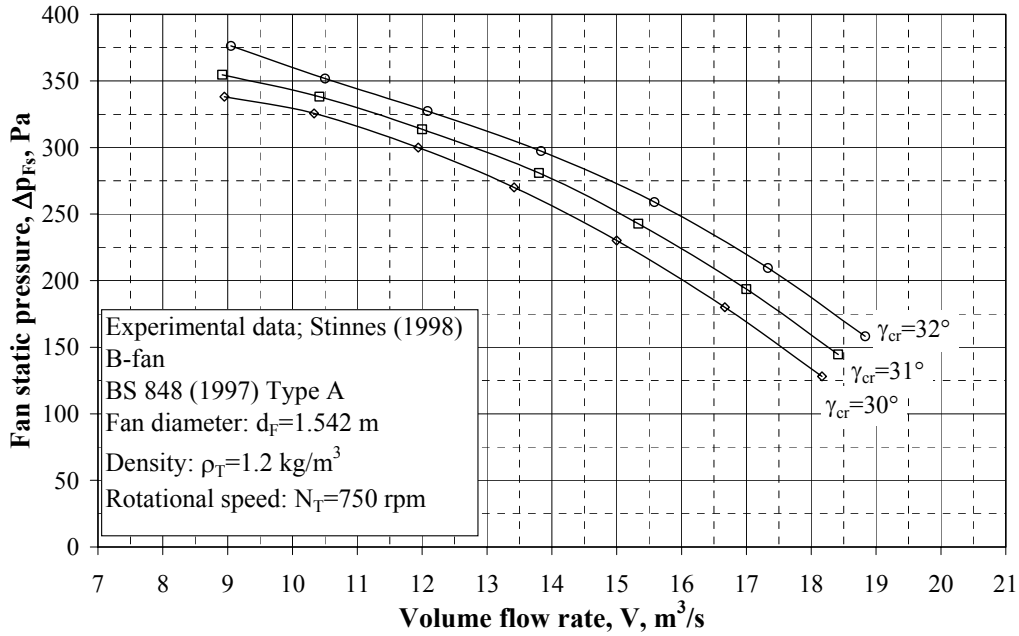

Figure B.12: Fan static pressure characteristic of the B-fan

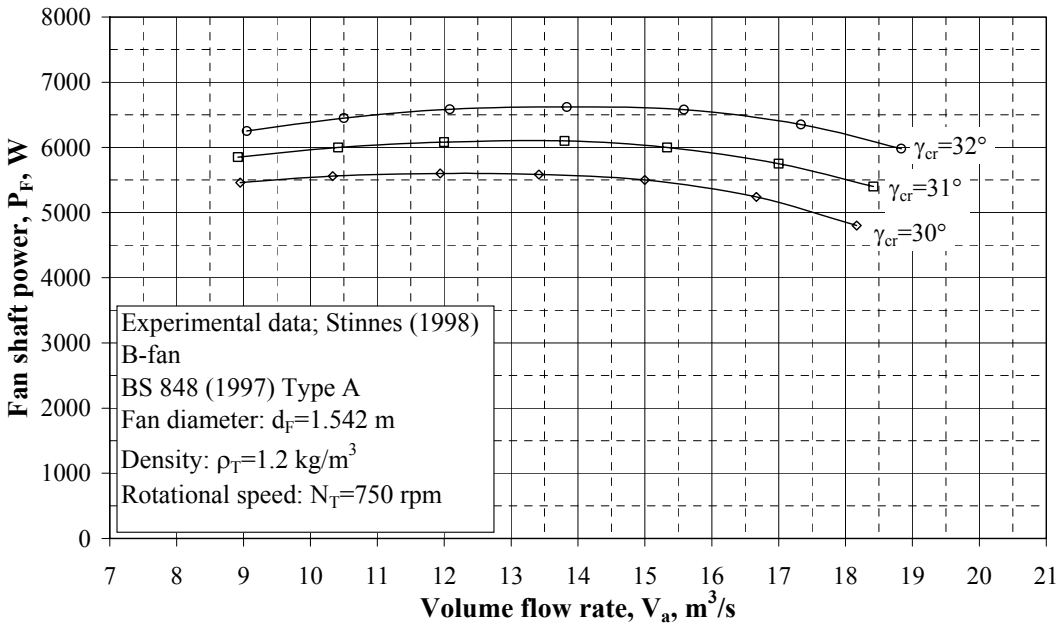

Figure B.13: Fan shaft power characteristic of the B-fan

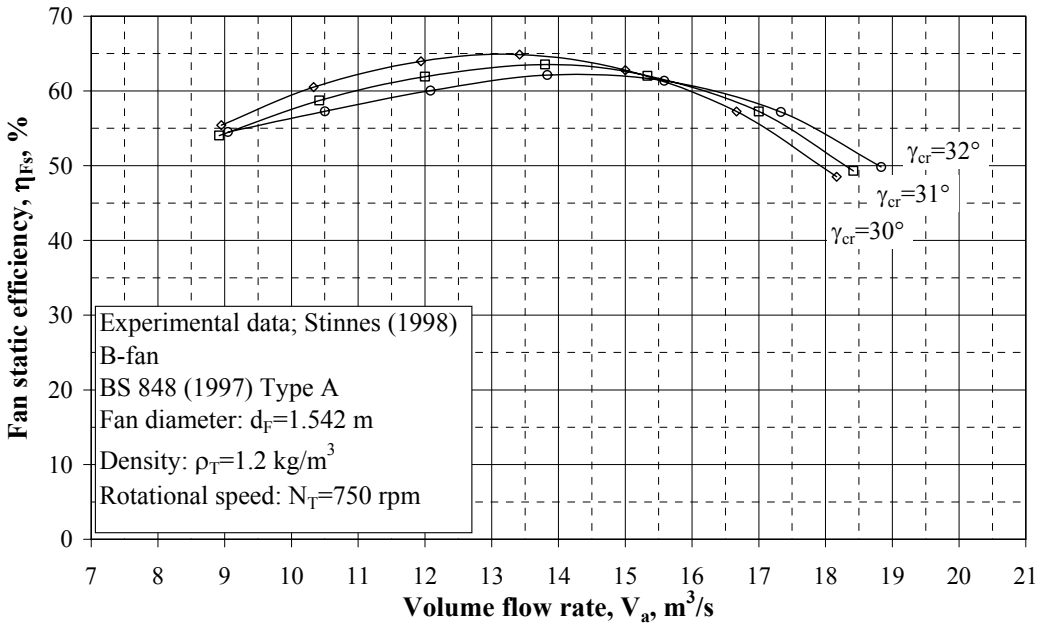

Figure B.14: Fan static efficiency of the B-fan

Appendix C. Calculation of Source Terms in the Numerical Heat Exchanger Model

C.1. Momentum sink terms

The numerical modelling of a flow resistance, or pressure drop, in a region of a flow domain, require the addition of a momentum sink terms to the relevant momentum equations. In this section, the calculation of the momentum sink terms for the numerical heat exchanger model, shown in figure C.1, is discussed.

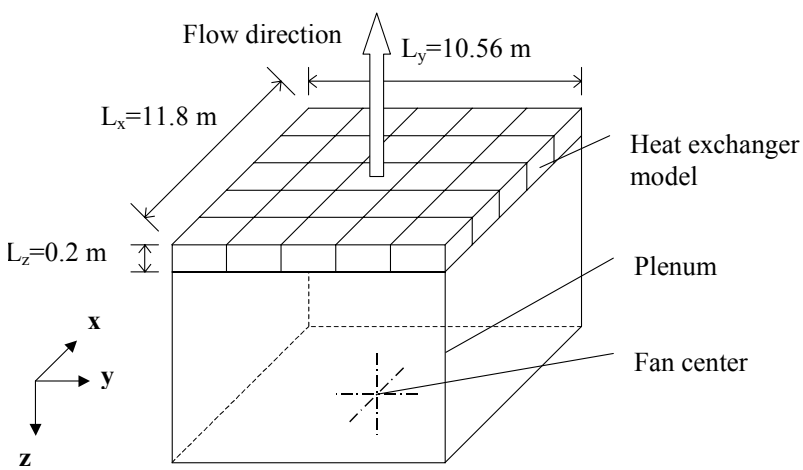

Figure C.1: Numerical heat exchanger model

Equation A.13 can be approximated by a second order polynomial

$$\begin{aligned}\Delta p_e &= -\left(2.4756\times10^{-4}V_a^2 + 4.31807\times10^{-3}V_a^{1.56073}\right)\\ &\approx -\left(4.132315\mathrm{E}\times10^{-4}V_a^2 + 5.629484\times10^{-2}V_a\right) \quad ,Pa\end{aligned} \tag{C.1}$$

The volume flow rate can be written in terms of the average velocity in the z-direction

$$V_a = |w|\left(L_x \times L_y\right) \tag{C.2}$$

so that equation C.1 written in terms of w, become

$$\begin{aligned}\Delta p_e &= -\left(4.132315\mathrm{E}\times10^{-4}V_a^2 + 5.629484\times10^{-2}V_a\right)\\ &= 4.132315\times10^{-4}\left(L_x\times L_y\right)^2|w|w + 5.629484\times10^{-2}\left(L_x\times L_y\right)w\\ &= 6.4163|w|w + 7.1048w \quad ,Pa\end{aligned} \tag{C.3}$$

The body forces acting in the z-direction in each cell of the numerical heat exchanger model, shown in figure C.1, is given by

$$F_z = \frac{\Delta p_e}{L_z} = 32.082|w|w + 35.074w \quad , N/m^3 \tag{C.4}$$

Due to the fact that flow is restricted in the x and y-directions, |**v**|≈|w|, so that the body force in the z-direction given in table 3.4 becomes

$$F_z = \left(C_z \frac{1}{2} \rho |w| w + \frac{\mu}{\alpha_z} w \right) \tag{C.5}$$

By comparing equations C.4 and equation C.5, the viscous and inertial loss coefficients, $1/\alpha_z$ and C_z, can now be calculated

$$C_z \frac{1}{2} \rho = 32.082$$
$$C_z = 59.1364$$

and

$$\frac{\mu}{\alpha_z} = 35.074$$
$$\frac{1}{\alpha_z} = 1.897 \times 10^6$$

C.2. Heat source terms

An UDF (refer so section 3.2) was written to model heat transfer to the air. In the UDF the mass flow rate, m_a, and the average inlet temperature, T_{ai1}, are read from the solver. These values are then used in order to calculate the heat source terms in the heat exchanger model at each iteration. The calculation procedure and equations used in this code are given below.

The characteristic flow parameter given by equation A.5, for the first tube row, is adapted so as to account for the reduction in effective frontal area due to a fewer number of tubes

$$Ry_1 = \frac{m_a}{\mu n_b A_{fr} \frac{n_{tb1}}{n_{tb2}}} \tag{C.6}$$

The effective air-side heat transfer coefficient is calculated according to equation A.4

$$hA_1 = k_a \Pr^{0.333} n_b A_{fr} Ny_1 \frac{n_{bt1}}{n_{bt2}} \tag{C.7}$$

where Ny_1 is the characteristic heat transfer parameter given by equation A.1. The heat transfer rate for the first tube row, is calculated according to equation 2.7

$$Q_1 = m_a c_{pa}\left(T_{ao1} - T_{ai1}\right) = e_1 m_a c_{pa}\left(T_s - T_{ai1}\right) \tag{C.8}$$

By rearranging equation C.8, a relation for the air outlet temperature is obtained

$$T_{ao1} = e_1 T_s + \left(1 - e_1\right) T_{ai1} \tag{C.9}$$

where e_1 is the effectiveness of the first tube row calculated according to equation 2.8.

$$e_1 = 1 - \exp\left(\frac{-UA_1}{m_a c_{pa}}\right) \tag{C.10}$$

In the above equation the thermal resistance of the condensate film, typically in the order of 2% of the total thermal resistance, is neglected, so that the UA_1=hA_1. With the outlet temperature of the first tube row, T_{ao1}, equal to the inlet temperature of the second tube row, T_{ai2}, the heat transfer rate from the second tube row, Q_2, can be calculated using a similar procedure described above. The outlet temperature of the second row is thus given by

$$T_{ao2} = e_2 T_s + \left(1 - e_2\right) T_{ai2} = e_2 T_s + \left(1 - e_2\right)\left[e_1 T_s + \left(1 - e_1\right) T_{ai1}\right] \tag{C.11}$$

The total heat transfer rate per fan unit is then

$$Q_{tot} = Q_1 + Q_2 = m_a c_{pa}\left(T_{ao2} - T_{ai1}\right) \tag{C.12}$$

Numerically the heat transfer to the air is modelled by adding heat source terms the relevant energy equations. The heat source terms, F_E, are calculated such that it would result in a uniform outlet temperature distribution.

$$F_E = \frac{\delta Q}{\delta V} = \frac{\delta m_a c_{pa}}{\delta V}\left(T_{ao2} - T_{ai1}\right) = \frac{\rho |w| c_{pa}}{L_z}\left(T_{ao2} - T_{ai1}\right) \quad ,W/m^3 \tag{C.13}$$

where δm_a and δV are the mass flow rate through a cell and the volume of a cell, respectively.

Appendix D. Fan Blade Profile Lift and Drag Characteristics

The actuator disc model discussed in section 3.2.2, requires isolated blade profile lift and drag coefficients, as a function of angle of attack (α).

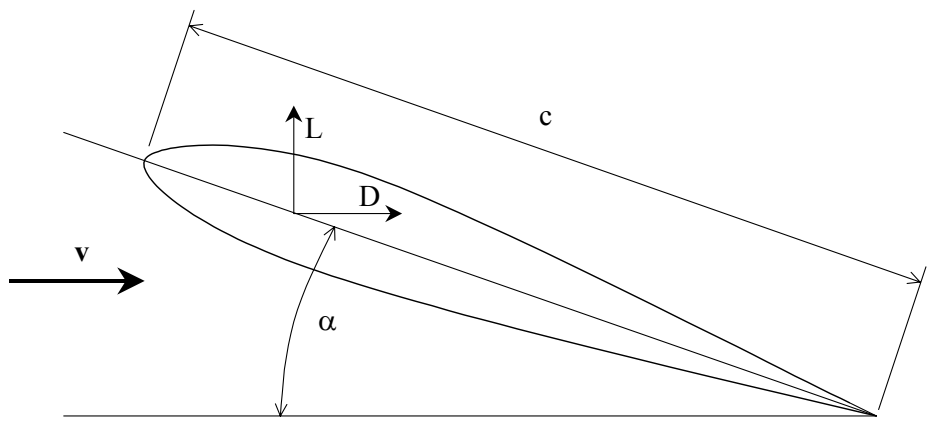

Figure D.1: Lift and drag forces on an isolated blade profile

The lift coefficient and drag coefficient per unit length of span are defined by equation D.1 and equation D.2, respectively.

$$C_L = \frac{L}{\frac{1}{2}\rho|\mathbf{v}|^2 c} \tag{D.1}$$

and

$$C_D = \frac{D}{\frac{1}{2}\rho|\mathbf{v}|^2 c} \tag{D.2}$$

where L, D and **v** is the lift force, drag force and free stream velocity magnitude, respectively, as shown in figure D.1. Distorted flow patterns near the fan inlet, and back flow near the hub, may result in a wide range of angles of attack (α). Depending on the severity of these factors, angles of attack, ranging between $-90° < \alpha < 90°$ can be expected.
The lift and drag characteristics of a blade profile (or airfoil) are a function of geometry, Reynolds number, and angle of attack, and can be determined by one of the following methods:

(a) **Analytically.** By applying classical potential flow and boundary layer theory, (Schlichting 1960; Houghton and Carpenter 1982; White 1991), the pressure and skin friction distribution along the airfoil can be determined for a specified flow condition. By integrating these parameters along the surface (perimeter) of the airfoil, the

aerodynamic forces can be calculated. This method can only be applied for a limited range (below stall) of angle of attack.

(b) **Empirically**. Hoerner (1965) and Hoerner and Borst (1975) provide empirical correlations for the lift and drag coefficients of airfoils, that are functions of camber ratio, thickness ratio, Reynolds number, and angle of attack. These correlations are also limited to angles of attack below stall. Thiart and von Backström (1993), discuss the implementation of these correlations in an actuator disc model, and recommend the use of flat plate data beyond stall.

(c) **Numerically**. CFD-based methods (Van Dam 1999) can be used to analyse the flow field around an airfoil using a two-dimensional or three-dimensional computational grid. It is found that the lift force, which is mainly dependent on pressure force, can be predicted with fair accuracy for attached flow conditions. The prediction of drag coefficient at low angles of attack however, is often less accurate. This is due to inaccuracies in predicting the viscous wall shear stresses. Insufficient grid resolution and the fact that transition in the boundary layer is neglected (the flow is assumed to be either fully laminar or turbulent), are some of the factors that might cause these inaccuracies. Despite these facts, RANS (Reynolds Averaged Navier Stokes) methods can effectively be used to predict the aerodynamic characteristics of airfoils for a wide range of flow conditions.

(d) **Experimentally**. The use of experimentally determined wind tunnel data is ideal. Experimental data is however not always available, as in the case of the A-fan blade profile. Furthermore, readily available experimental data is usually limited to the attached flow conditions, and do not include data beyond stall.

In this study, numerically determined data was used if experimental data was unavailable. The purpose of this appendix is to discuss and validate this numerical procedure. Furthermore, the lift and drag coefficients for the A-fan and B-fan blade profiles are given.

D.1. Numerically Determined Lift and Drag Coefficients

By modelling the flow field around a particular fan blade profile (or airfoil), at a prescribed angle of attack and Reynolds number, the resulting pressure and viscous forces acting on its surface, can be calculated. In this section, such a method is evaluated by comparing numerically predicted lift and drag coefficients to experimental data, for the NASA GA(W)-2 airfoil tested by McGhee et al. (1977).

D.1.1. Computational aspects

A two-dimensional computational grid was used to resolve the flow field around the fan blade profile. The circular flow domain has a radius of thirty chord lengths and consists of 28,800 rectangular elements, as shown in figure D.2.

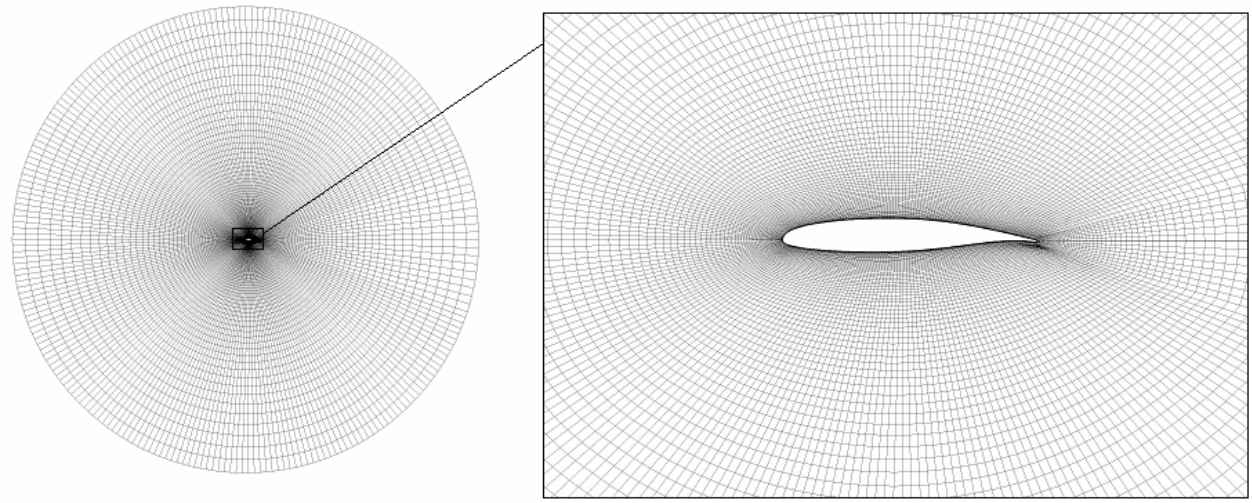

Figure D.2: Computational grid for the NASA GA(W)-2 airfoil

Details of the mesh near the surface are shown in figure D.3. The height of the wall-adjacent cells corresponds to $y^+ \approx 30$. This condition ensures the effective implementation of the log-law wall function, discussed in section 2.1.

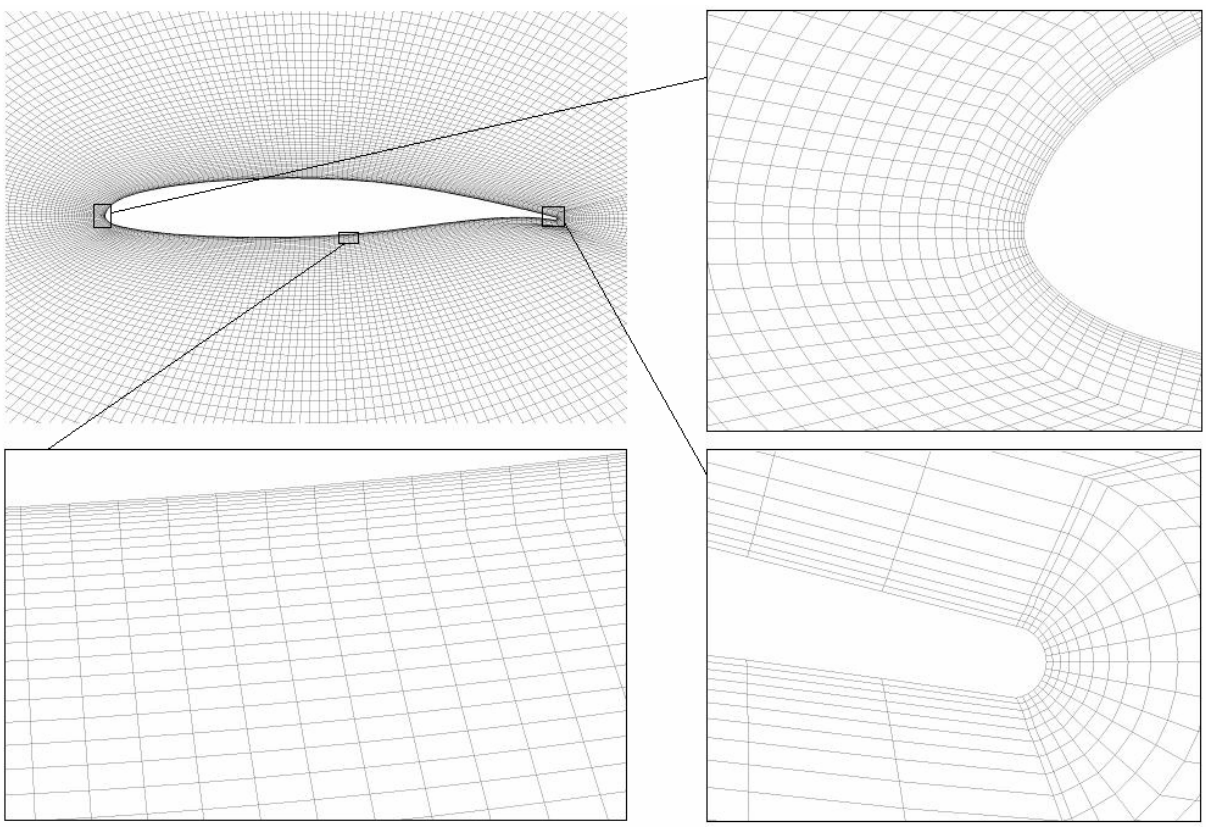

Figure D.3: Computational grid near the surface of the NASA GA(W)-2 airfoil

The flow was assumed to be incompressible and time independent (steady state).

Two turbulence models, namely the k-ε model of Launder and Spalding (1974), and the k-ω shear stress transport (SST) model of Menter (1994), were compared.

A velocity inlet boundary condition was specified at the periphery of the domain. The angle of attack was thus determined by prescribing the appropriate velocity vector at this boundary. The surface of the airfoil was modelled as a zero-slip wall.

For angles of attack below stall, the second order upwind discritization scheme was employed for the convective terms in the momentum equations. Beyond stall the flow was found to be highly unstable (or transient), characterised by periodic vortex shedding. Under such conditions first order upwind discritization was used in order to ensure better convergence.

D.1.2. Results and discussion

The numerically determined lift and drag coefficients, using both the k-ε turbulence and the k-ω SST turbulence model, are compared to experimental data in figure D.4 and figure D.5, respectively.

The average percentage error between the numerically predicted lift coefficient and experimental data, using the k-ε turbulence model and the k-ω SST turbulence model, are 2.5% and 5.8%, respectively.

It can be seen in figure D.4 that the prediction of the drag coefficient is less accurate, particularly at low angles of attack where viscous forces are dominant. The best results are again obtained using the k-ε model, which predicts the drag coefficient within an average error of 25%, compared to 57% using the k-ω SST model.

It was found that the actuator disc model was more dependent on (or sensitive to) lift coefficient data, than on drag coefficient data, at low angles of attack. A possible reason for this is the relatively high lift-drag-ratio, $C_L/C_D \approx 100$, that occurs for $0° < \alpha < 4°$. For this particular application, the numerical prediction of the drag coefficient using the k-ε model was therefore sufficiently accurate, and produced acceptable results.

For angles of attack beyond stall separated flow conditions were observed as shown in figure D.6 for $\alpha = 24°$.

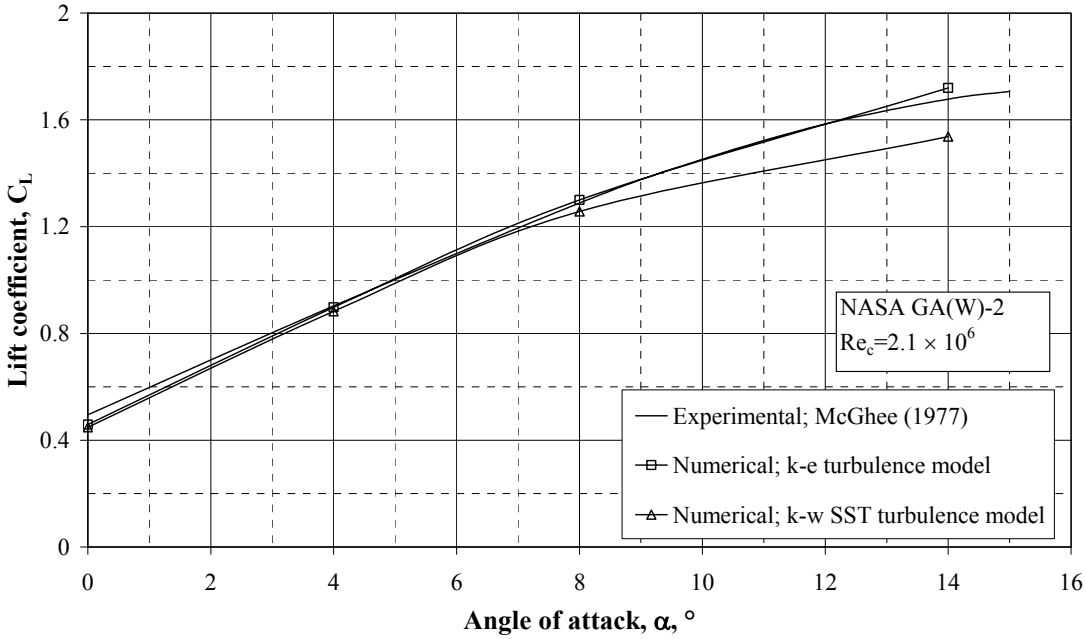

Figure D.4: Numerically determined lift coefficient of the NASA GA(W)-2 airfoil

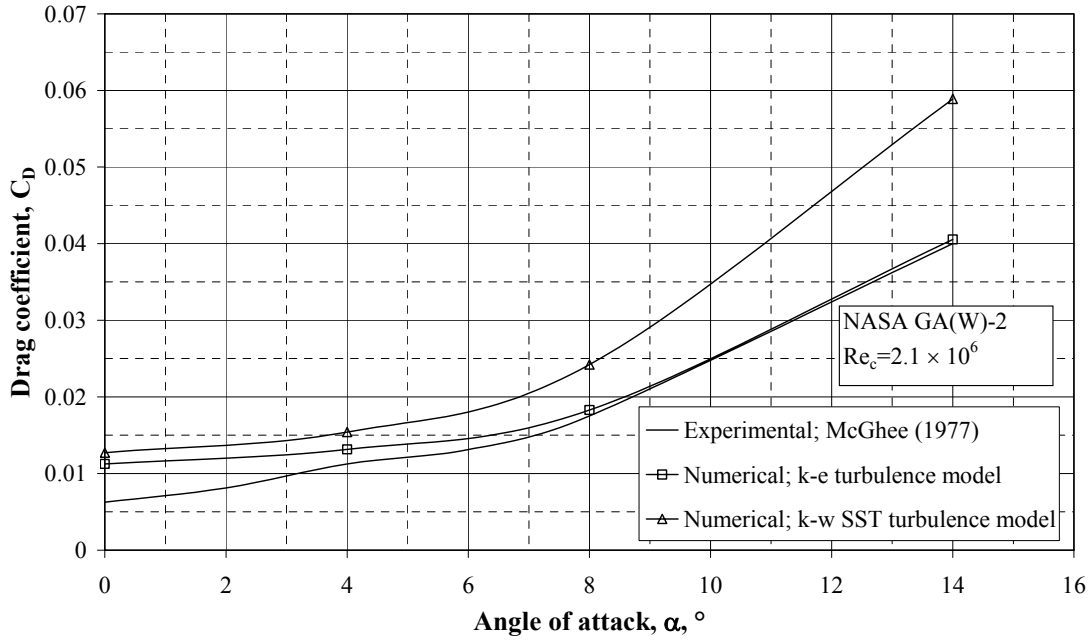

Figure D.5: Numerically determined drag coefficient of the NASA GA(W)-2 airfoil

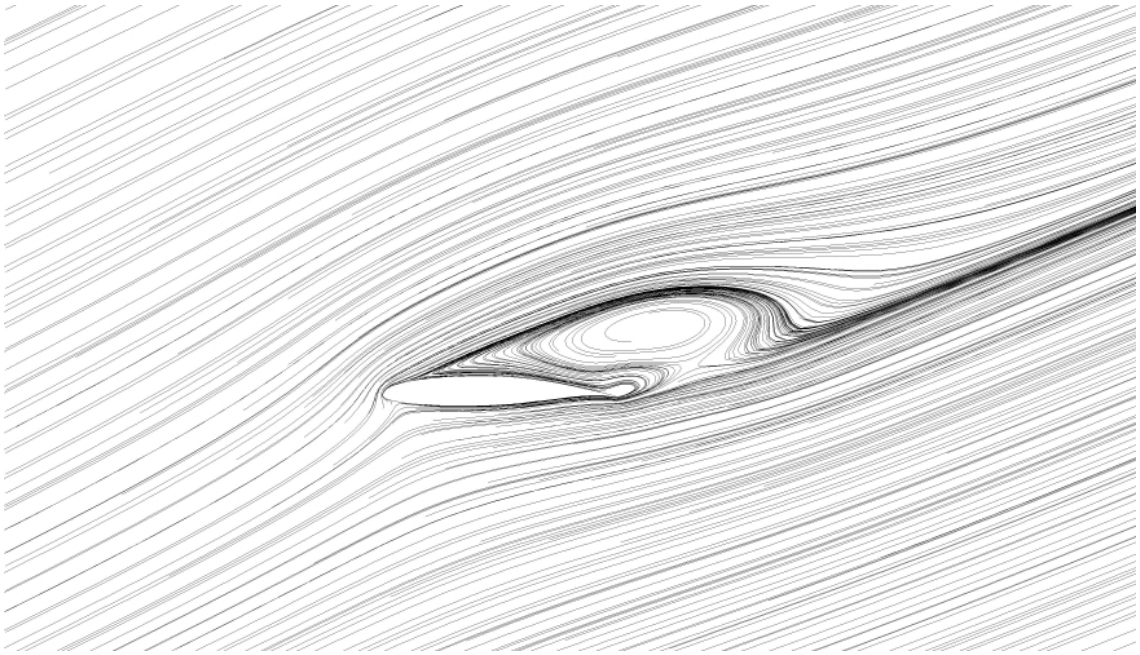

Figure D.6: Streamline plot for the NASA GA(W)-2 airfoil at α=24°

Due to the periodic nature of the flow, the lift and drag coefficients were averaged, as shown in figure D.7.

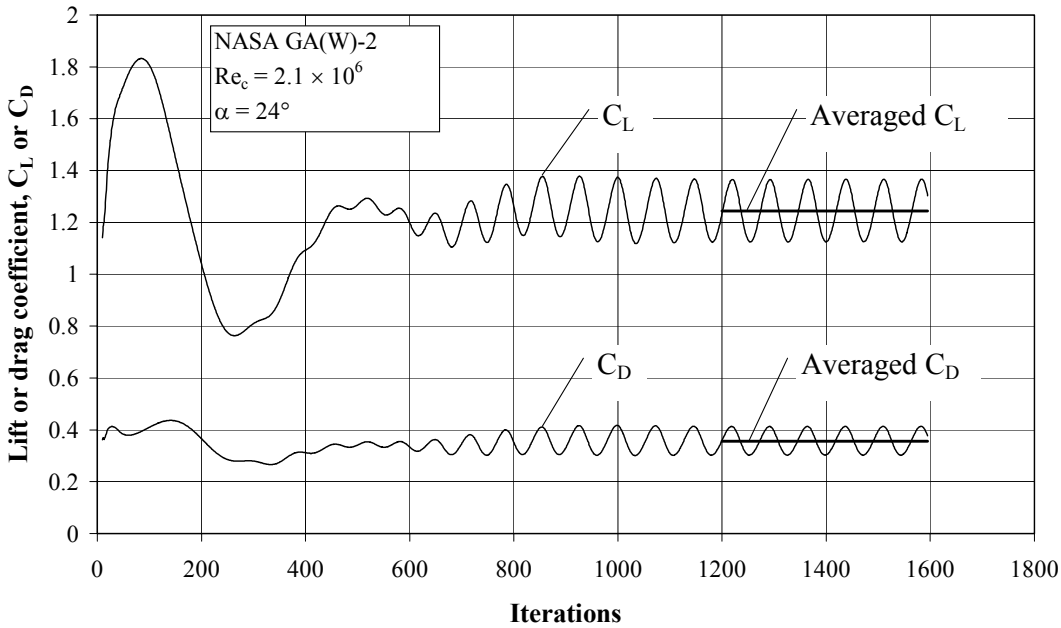

Figure D.7: Numerically determined lift and drag coefficients for the NASA GA(W)-2 airfoil at α=24°

The accuracy of the lift and drag coefficients beyond stall could not be determined. It should therefore be emphasised that the numerical procedure discussed above serves as a method to approximate the time averaged forces on a particular airfoil section under prescribed flow conditions.

D.2. A-fan blade profile lift and drag characteristics

Owing to the unavailability of experimental data, the lift and drag characteristics of the A-fan blade profile was determined numerically, using the same resolution grid as discussed in the previous section. For the A-fan with a diameter of d_F=9.145m operating under normal conditions, the Reynolds number based on the chord length of the fan blade, may range between $4 \times 10^5 < Re_c < 2.6 \times 10^6$. The variation of lift and drag coefficients within this range of Reynolds numbers were however found to be negligible. Numerical simulations were therefore conducted at an average Reynolds number of 1.5×10^6. The numerically predicted lift and drag coefficients for the A-fan blade profile are given in figure D.8. For use in the actuator disc model, the numerical data was represented by a series of polynomial curve fits.

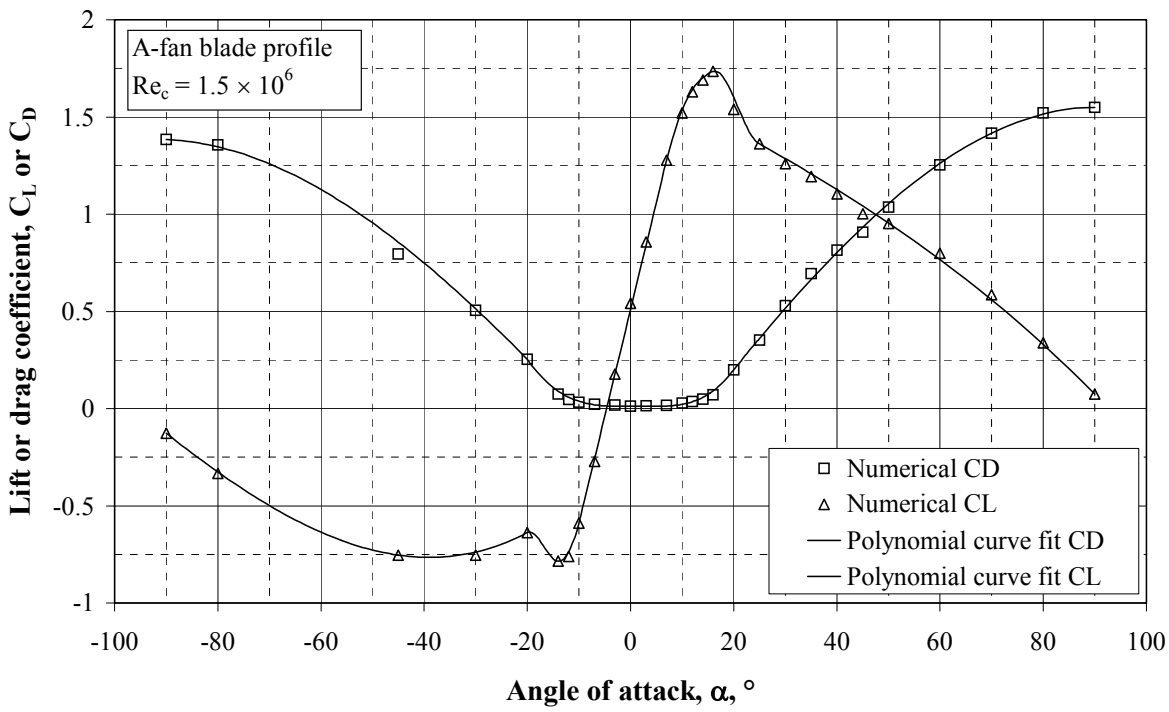

Figure D.8: Lift and drag coefficients of the A-fan blade profile for -90°<α<90°

D.3. B-fan blade profile lift and drag characteristics

Experimental lift and drag coefficient data of the NASA GA(W)-2 airfoil used in the design of the B-fan is given in Bruneau (1994) (it is assumed that the experimental data corresponds to Reynolds number of approximately 1.9×10^6). For angles of attack falling outside the range of experimental data, the coefficients were determined numerically at the same Reynolds number. The experimental and numerical data was again represented by a set of polynomial curve fits, as shown in figure D.9. As in the case of the A-fan, the Reynolds number effects are neglected.

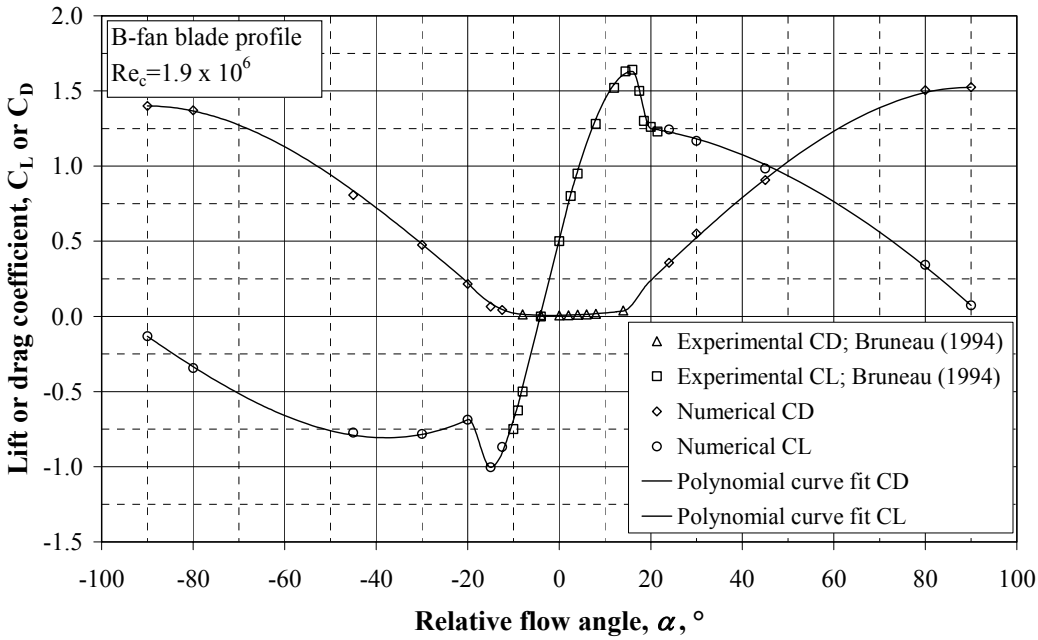

Figure D.9: Lift and drag coefficients of the B-fan blade profile for -90°<α<90°

Appendix E. Numerical Fan Performance Results for a Section of the ACSC under Windless Conditions

E.1. Fan performance results at a platform height of H_i=26 m

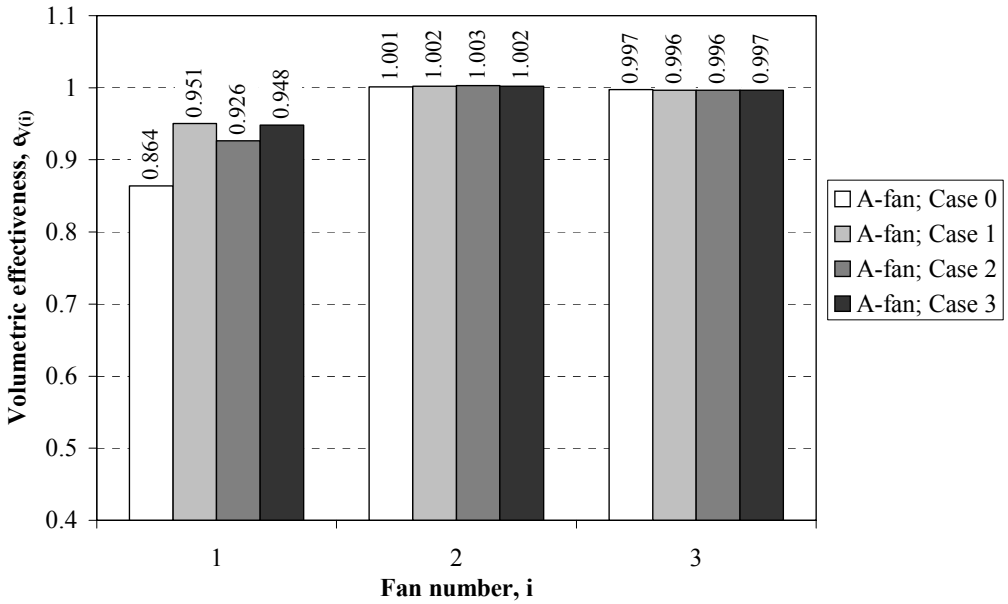

Figure E.1: Volumetric effectiveness for the A-fan (d_F=9.145 m, γ_{pt}=16°) at H_i=26 m

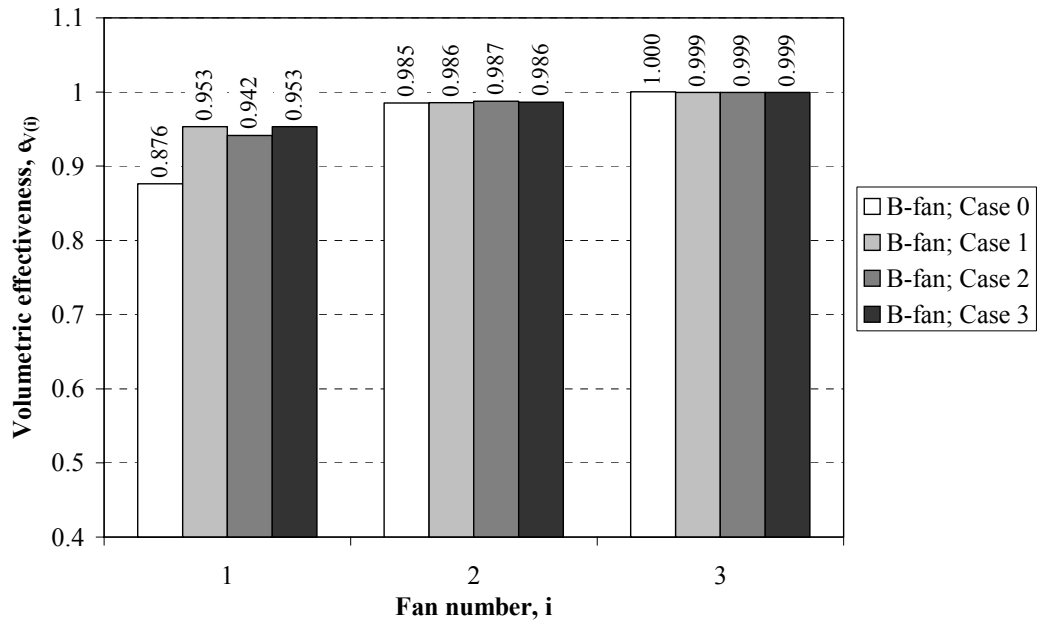

Figure E.2: Volumetric effectiveness for the B-fan (d_F=9.145 m, γ_{cr}=34.5°) at H_i=26 m

E.2. Fan performance results at a platform height of H_i=22 m

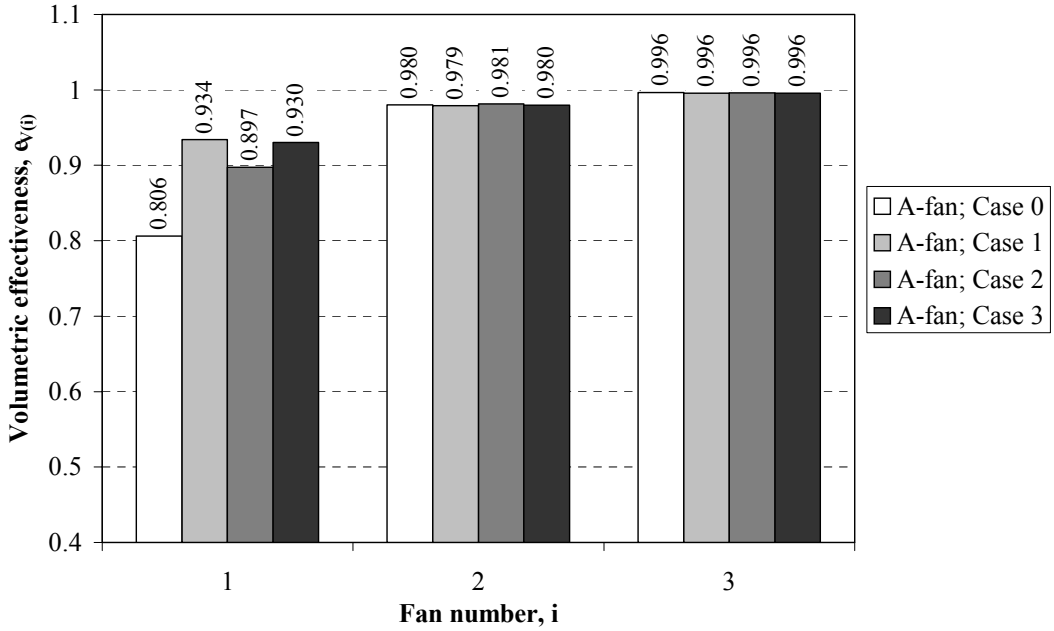

Figure E.3: Volumetric effectiveness for the A-fan (d_F=9.145 m, γ_{pt}=16°) at H_i=22 m

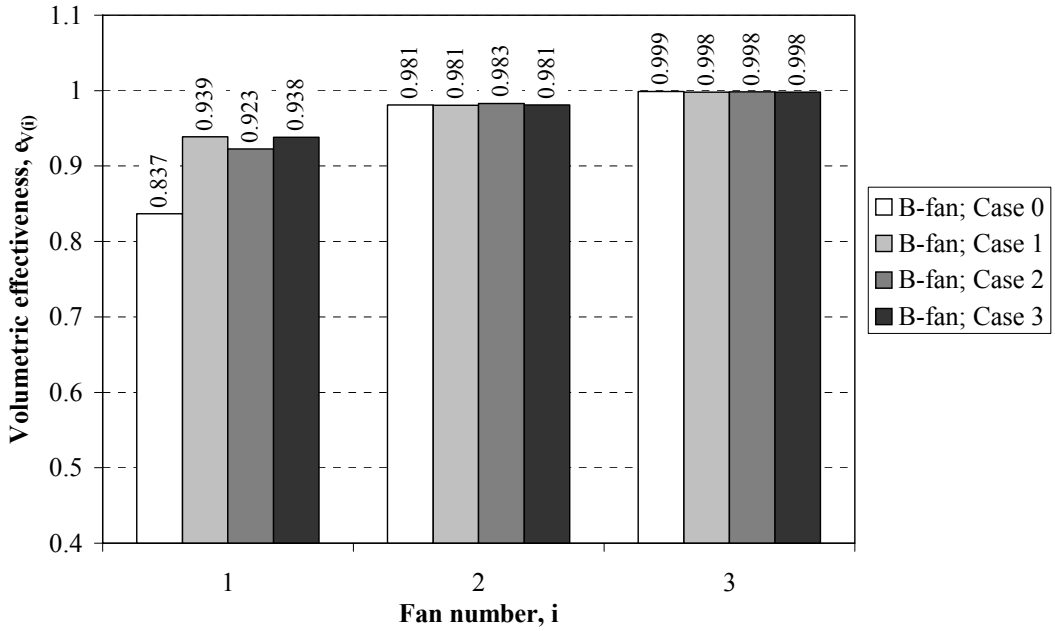

Figure E.4: Volumetric effectiveness for the B-fan (d_F=9.145 m, γ_{cr}=34.5°) at H_i=22 m

E.3. Fan performance results at a platform height of H_i=18 m

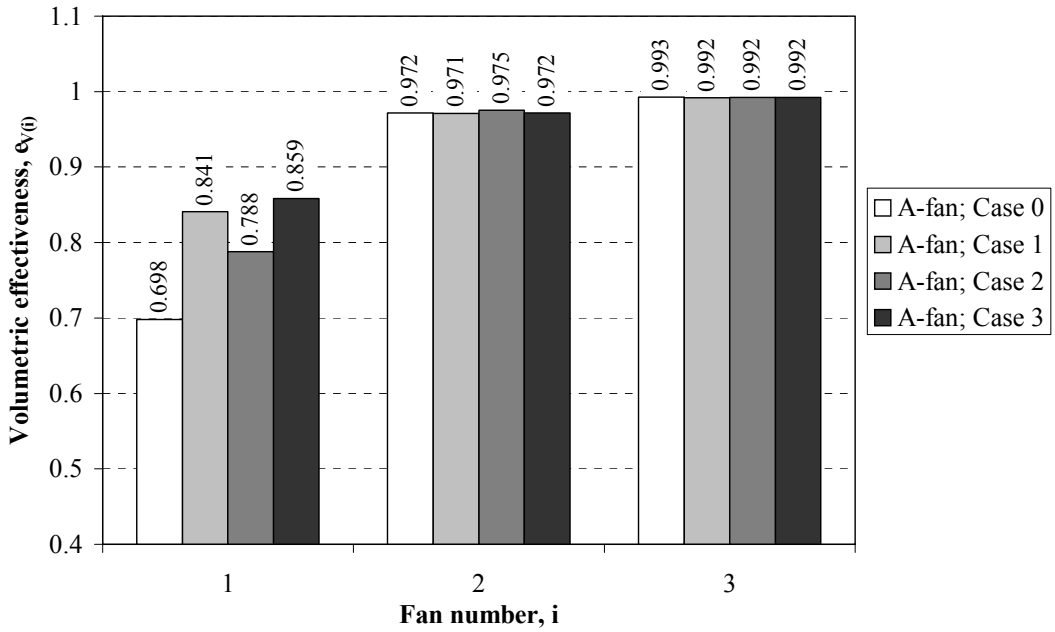

Figure E.5: Volumetric effectiveness for the A-fan (d_F=9.145 m, γ_{pt}=16°) at H_i=18 m

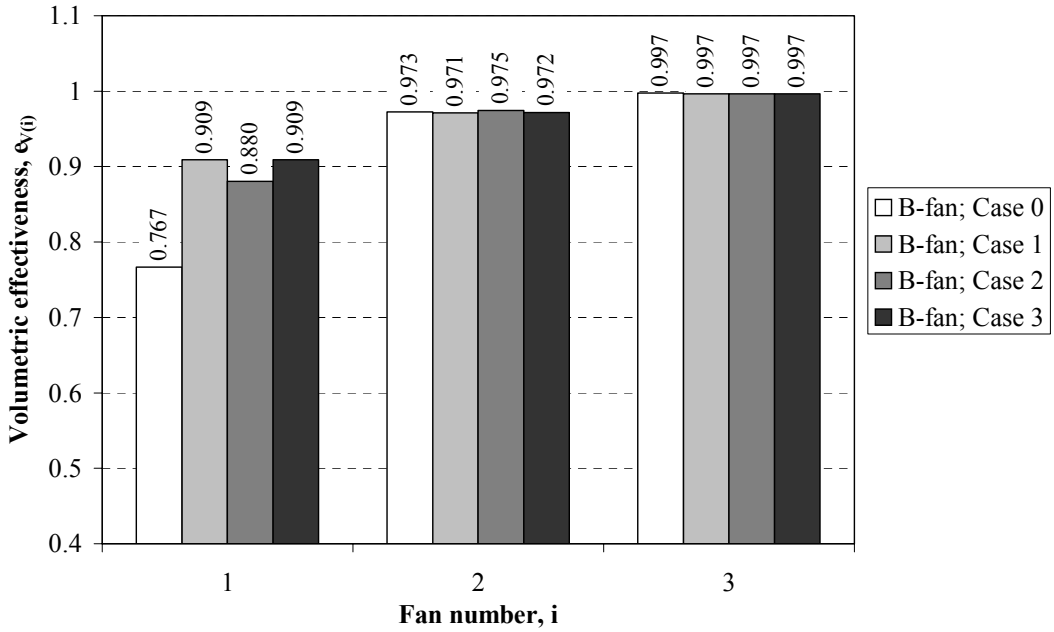

Figure E.6: Volumetric effectiveness for the B-fan (d_F=9.145 m, γ_{cr}=34.5°) at H_i=18 m

E.4. Fan performance results at a platform height of H_i=14 m

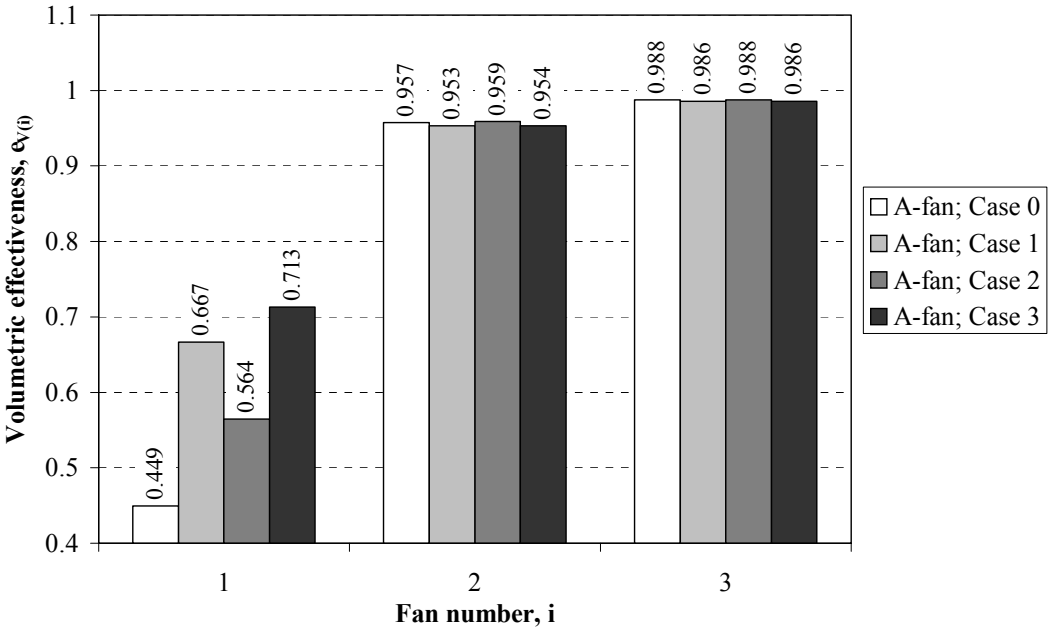

Figure E.7: Volumetric effectiveness for the A-fan (d_F=9.145 m, γ_{pt}=16°) at H_i=22 m

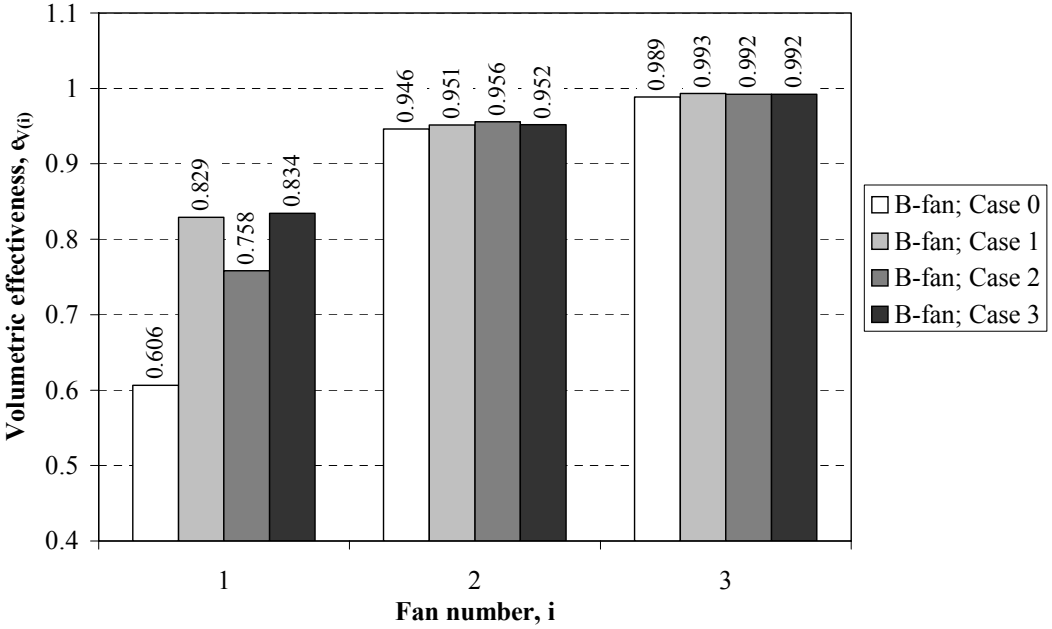

Figure E.8: Volumetric effectiveness for the B-fan (d_F=9.145 m, γ_{cr}=34.5°) at H_i=18 m